Summer 8-2019

Development of a Low Profile, Endoscopic Implant for Long Term Brain Imaging

Benjamin Scott Kemp
Louisiana Tech University

DEVELOPMENT OF A LOW PROFILE, ENDOSCOPIC IMPLANT FOR LONG TERM BRAIN IMAGING

by

Benjamin Scott Kemp, B.S.

A Dissertation Presented in Partial Fulfillment
of the Requirements of the Degree
Doctor of Philosophy

COLLEGE OF ENGINEERING AND SCIENCE
LOUISIANA TECH UNIVERSITY

August 2019

LOUISIANA TECH UNIVERSITY

THE GRADUATE SCHOOL

JUNE 12, 2019
Date

We hereby recommend that the dissertation prepared under our supervision by

Benjamin Scott Kemp, B.S.

entitled **DEVELOPMENT OF A LOW PROFILE, ENDOSCOPIC IMPLANT FOR LONG TERM BRAIN IMAGING**

be accepted in partial fulfillment of the requirements for the Degree of

Doctor of Philosophy in Biomedical Engineering

Supervisor of Dissertation Research

Head of Department
Biomedical Engineering
Department

Recommendation concurred in:

Advisory Committee

Approved:

Director of Graduate Studies

Dean of the College

Approved:

Dean of the Graduate School

GS Form 13
(8/10)

ABSTRACT

The increased public awareness of concussion and traumatic brain injury has motivated continued research into the brain, its functions, and especially its response to injury, with a focus on improving the brain's repair capabilities. However, due to the critical nature of the tissue, it is currently difficult for researchers to acquire high resolution images below the cortex without sacrificing a lab animal. Sacrificing an animal greatly reduces the amount of data that can be obtained from it, making longitudinal studies unappealing or unfeasible because a large number of animals is needed to obtain useful data over multiple time points. Additionally, inter-animal variance can further obfuscate results.

The gradient index (GRIN) lens is a form of micro-endoscope that can penetrate the cortex to obtain high resolution, *in vivo* images when used with a multiphoton microscope system. The lens is implanted through the skull and into the brain, providing a column of material that refracts and refocuses the laser beam, unlike the natural tissue, which scatters light.

This dissertation describes the development of a low profile GRIN lens implant system suitable for longitudinal imaging, as well as the co-development of a restraint system to accommodate the new implant on a microscope stage. The imaging protocol is detailed, and images acquired over three months are shown. The developed device drastically reduced the size of implant both above the skull and within the brain tissue

compared to previously reported GRIN lenses, while still obtaining the expected high resolution images. This research also found that labelled axons in transgenic mice appear in unique, recognizable patterns which remain consistent over months of imaging, meaning future studies may use the axons themselves as landmarks. An experimental design for analyzing traumatic brain injury is also developed, which could incorporate a future implant.

APPROVAL FOR SCHOLARLY DISSEMINATION

The author grants to the Prescott Memorial Library of Louisiana Tech University the right to reproduce, by appropriate methods, upon request, any or all portions of this Dissertation. It is understood that "proper request" consists of the agreement, on the part of the requesting party, that said reproduction is for his personal use and that subsequent reproduction will not occur without written approval of the author of this Dissertation. Further, any portions of the Dissertation used in books, papers, and other works must be appropriately referenced to this Dissertation.

Finally, the author of this Dissertation reserves the right to publish freely, in the literature, at any time, any or all portions of this Dissertation.

Author _____

Date _____

DEDICATION

This dissertation is dedicated to my family. Without their constant support and motivation, it would not exist.

TABLE OF CONTENTS

LIST OF FIGURES

LIST OF TABLES

ACKNOWLEDGEMENTS

First and foremost, I would like to thank my committee: Dr. Teresa Murray, Dr. Steven Jones, Dr. Mark DeCoster, Dr. Jamie Newman, and Dr. Bryant Hollins. Each of my committee members has supported my education in both the classroom and the lab, providing me with the tools necessary to analyze the literature and conduct my own research. They have always provided an open and welcoming atmosphere, freely giving their time and encouragement during one on one conversations. I am especially grateful for their considerable patience during the writing of this dissertation.

I would also like to thank Dr. James Spaulding and Emily Born for their diligent care of the animals used in this research. Without their expertise, this work would not have been possible. I would also like to thank them, as well as Debbie Wood and Davis Bailey, for their attentive care of the facilities.

I would like once again thank Dr. Spaulding, as well as Dr. Brandon Moore and the Lifshitz lab in Phoenix, AZ for their mentorship in animal handling, histology, and experimental procedures. Many of the skills I have developed during the course of this research would be considerably underdeveloped without their guidance.

Finally, I would like to thank my fellow lab members, especially Peace Ibole, Dr. Chelsea Pernici, Dr. Kevin Holly, Vlad Voziyanov, and Kayla Ponder. Thanks for covering when I couldn't come in, providing your own skills in areas I didn't have them, commiserating through frustration and exhaustion, and putting up with all the music.

CHAPTER 1

INTRODUCTION

1.1 Introduction to Light Microscopy

The invention of simple light microscopes allowed researchers to analyze objects too small to be resolved with the human eye. Despite the invention of more powerful microscopes in the following centuries, light microscopy is still often used in biological studies because it is highly compatible with living tissue. The continued prevalence of light microscopy in science necessitates the continued enhancements of the technique.

As the name implies, light microscopy relies on the illumination of a sample with electromagnetic radiation. Although the reflections and distortions of a wide range of wavelengths can be used to analyze a sample, the most commonly used techniques in biology rely on wavelengths between the ultraviolet and infrared range. These wavelengths include 380 to 780 nm, the range of light visible to the human eye[1], as well as wavelengths that can be used to excite the emission of visible light from fluorescent particles. In addition to generating data that can be interpreted without additional instrumentation, brief exposure to wavelengths between the ultraviolet and infrared range are less likely to damage the sample than wavelengths of higher frequency.

The reliance on light in the visible and near-visible range comes with a trade-off. Light microscopes are diffraction limited, meaning they are unable to resolve objects that are smaller than the wavelength of the light used to observe them. In biology, this limit

prevents light microscopes from clearly imaging most subcellular features, such as receptors on the surface of cells and organelles contained within the cell. Biological samples are also composed of particles that cause extensive scattering of light in the visible spectrum. When electromagnetic radiation interacts with sufficiently sized particles, it causes oscillations in the electrical charges of the matter, eventually resulting in a loss of energy[1]. The loss of energy affects how deeply light can penetrate into a tissue sample, creating constraints for the size of samples researchers can effectively analyze. Light scattering also creates secondary waves in all directions around the particle, which further interfere with the light reflected back to the researcher.

The light microscope uses lenses to change the angles of rays of light reflected off an object of interest. The simplest magnifiers, single lenses, simply allow the user to physically move an object closer to their eye, projecting a magnified image through the lens onto the user's retina[2]. This process can be repeated with multiple lenses to increase the amount of magnification. However, the resulting magnification depends on the focal lengths of the lenses used, which can be defined as the distance from the lens at which parallel light rays entering the lens converge through refraction[3]. In a two lens system, the equation for calculating magnification is shown in **Eq. 1-1**

$$M = 25\frac{L}{f_e f_o} \qquad \textbf{Eq. 1-1}$$

where f_e is the focal length of the lens in the eyepiece, f_o is the focal length of the objective lens, and L is the physical distance between those two points in the microscope. Most modern systems can also alternately project the final image to the focal point of a digital camera, which allows the resulting image to be recorded.

1.1.1 Histological Staining

Although, at the macroscopic level, most biological samples will reflect light, a single layer of cells is mostly transparent. This presents a problem, because, as previously mentioned, light will only penetrate samples to a certain depth. To provide the greatest amount of illumination, and thereby collect the most data through microscopic analysis, samples must be cut into sections one to two cell layers thick[4]. Once the samples are reduced to the appropriate size, they can be stained with specific dyes. Histological staining allows researchers to take advantage of the natural transparency of the cell. The affinity of a dye to a specific cellular region creates a visible signal in only that region, reducing the amount of extraneous information that would have to be filtered out if the cell were not transparent

Before a sample can be sectioned, it must be properly prepared. The process begins as soon as the sample can no longer support its own vital functions. As nutrients are depleted, chemical cascades begin within the cells that eventually destroy the tissue. Since the goal is to obtain a sample that is as relevant to the natural state as possible, it is best if these cascades can be avoided entirely. To that end, past researchers have developed multiple chemical fixatives that arrest the chemical functions in a tissue sample by cross-linking protein groups within the cells[4]. One of the most popular chemical fixatives is formalin, a diluted solution of formaldehyde. The solution is typically buffered with salts to reach an ion balance near that of the tissue, minimizing changes in cell size due to osmosis. In experiments on tissue samples collected directly from an animal, the animal is typically perfused with formalin before sample collection,

allowing the fixative to spread from both the sample surface and the underlying vasculature.

Though the fixed sample is no longer in danger of deteriorating, it is still not ready to be sectioned. The natural tissue is often irregularly shaped, making regular sections difficult to obtain, and may not have a consistency that lends itself to cutting. Soft tissues such as the brain, for example, will often first compress against a blade before beginning to cut. That compression will cause the section to vary in thickness and structures that should appear in the same plane will instead be separated. To prevent these problems, past researchers have developed embedding methods to provide regularly shaped samples that can be sectioned precisely. Paraffin wax is a common embedding material because it has a convenient melting point. The proteins in biological samples will not denature at the wax's melting point, and the wax will harden at room temperature. However, paraffin wax is not water soluble. Since the samples are infused with formalin, an aqueous solution, they must be further processed. Ethanol, being miscible with water, is used to dehydrate the sample. The dehydration is done in graded steps (70% ethanol, 80%, 95%, 100%) to prevent the cells from shrinking drastically. Ethanol is also miscible with organic solvents, such as the commercially available HistoClear. The organic solvent is miscible with the paraffin wax, allowing the sample to be infused with wax and reach a consistency appropriate for sectioning.

The dehydration and infusion process will destroy certain portions of the sample. Lipids are typically the most vulnerable to the organic solvent, thus most of the lipids present in the sample will be lost using the described process. Some alternative fixation processes better preserve lipids, but it is unnecessary to describe them here. Paraffin

embedding will generally preserve only the protein network present in the sample, but that is often enough to elucidate a wide variety of data.

After the sample has been embedded, it can be mounted in a microtome and sectioned to the desired thickness. Optimal thickness is determined by the orientation of the sample to the cutting edge and the size of the structure to be stained. For example, myelinated axons can be stained with Luxol Fast Blue dye, but the axons themselves are very thin. Researchers are advised to obtain 10-15 μm thick sections in order to capture enough axons to interact with a visible amount of dye. Alternatively, hematoxylin is a common nuclear stain. It is better to keep sections thin, in the 7-10 μm range, to ensure only a single cell layer is captured and prevent nuclei from overlapping in the section. Once cut, wax sections are mounted onto glass slides until ready to be stained.

A large variety of staining methods can be used once a sample is prepared. In the early and mid-twentieth century, popular methods included metal impregnation and a variety of dyes. However, metal impregnation was notoriously unreliable and difficult to replicate[3]. Dyes were a better option, but, even if the chemical structure of the dye was known, the reason it bound to certain parts of a sample and not others was not always clear. Use of dyes with known mechanisms is a simple process which has retained its popularity. A classical example is hematoxylin and eosin staining, which provides a darkly stained cell nucleus with a pink background for contrast. The dye molecules bind ionically, with hematoxylin attracted to the negatively charged nucleus, and eosin attracted to the positively charged proteins in the cytoplasm[4]. For this method, one must rehydrate the slides by reversing the steps from the dehydration process and then expose the slides to an aqueous solution of hematoxylin. The slides are then dehydrated

to a specific point, and exposed to an ethanol based solution of eosin dye. After staining, the tissue on the slides is covered with an optically clear resin which binds a separate piece of cover glass, protecting the sample. An example staining protocol is provided in the appendix, including exposure times.

New staining methods were developed in the late twentieth century. These were based around fluorescently labelled binding agents, most notably specific antibodies. Antibodies gained popularity in histological staining (referred to as immunohistochemical staining when antibodies are used) because of their specificity. Naturally, antibodies serve as labels for the immune system, their light chains binding to exposed proteins in viruses, bacteria, and parasites, labelling them for destruction. The natural labelling capabilities were used to the advantage of histologists. Past researchers exposed specific proteins to the immune systems of animals of a different species than the proteins' origin. In the new species, the proteins acted as antigens, inciting the host to create antibodies against them. The newly created antibodies could be labelled with a dye molecule or metal particle, and then used to label specific portions of a biological sample. Though applying an antibody stain to a sample has a steep learning curve, once mastered the technique brings a previously unprecedented accuracy to histological staining.

1.2 Fluorescence Microscopy

The introduction of fluorescent dyes into histological staining provided an additional level of specificity, as well as an increased signal to noise ratio. Unlike the previously described dyes, which absorb most wavelengths of light and reflect a smaller band[1], resulting in their unique colors, fluorescent dyes will only respond to a very

narrow range of wavelengths. This range is referred to as the excitation wavelength for the fluorescent molecules. Instead of absorbing a portion of the light spectrum and reflecting back the remainder, fluorescent particles emit light in a separate narrow band referred to as the emission wavelength. The emission wavelengths are always of lower frequency than the excitation wavelengths[3]. The narrow bands for emission and excitation allow researchers to use bandpass filters to reduce the amount of background noise during data acquisition. Because the emission and excitation wavelengths always differ, superfluous light from the source used to illuminate the sample can also be filtered, further reducing noise.

As well as reducing noise, the narrow emission bands of fluorescent dyes can allow for specific image captures in multiple colors. Excitation lamps that illuminate fluorescently stained samples can provide a wide range of wavelengths, guaranteeing that the excitation bands for multiple dyes are covered. The light path used for data acquisition is filtered to allow light in only the emission wavelengths of the dyes to pass to the eyepieces or camera. An example of this scenario is an antibody labeled with green fluorescent dye and a sample exposed to the fluorescent stain DAPI. DAPI is a blue dye that can permeate the cell membrane and has a strong affinity for the nucleus. The antibody will only attach to a specific antigen presented in parts of the cell, such as a portion of the NMDA receptor. All of the nuclei in the sample would be revealed through the DAPI stain, while the NMDA receptors would be shown with the green emitting antibodies. Using this technique would allow researchers to count all cells in the sample, and then determine which cells appeared to display the NMDA receptor, and how that receptor was localized.

Fluorescent stains lend themselves to other interesting techniques, such as Förster resonance energy transfer (FRET). FRET relies on careful selection of two separate fluorescent particles, such that each has a different excitation wavelength, but the emission wavelength of one overlaps the excitation wavelength of the other[3]. The technique requires that the particles are close together in order for the energy from the first set of particles to be captured by the second. In this way, researchers can use only the excitation wavelength of the first set of fluorescent particles to determine their location relative to the second. FRET has been used to identify conformations in cell receptors by fluorescently labelling the proteins that comprise the receptor subunits[5].

Fluorescent dyes and proteins have some disadvantages over traditional histological stains. Because light is emitted in all directions simultaneously, fluorescent stains will reduce the maximum resolution of an image, obliterating finer details such as the shape of dendrites. Fluorescent particles are also subject to photobleaching, or the loss of the particle's ability to continue emitting photons. Photobleaching occurs after prolonged exposure to an excitation wavelength and is usually temporary.

1.2.1 Confocal and Multiphoton Microscopy

Although traditional light microscopes can be equipped with the proper lamp to excite fluorescent dyes, developments in the field have allowed researchers to build on the increased signal to noise ratio gained from using fluorescent dyes. The confocal and multiphoton microscopes use lasers to illuminate samples at a precise wavelength, while their design allows for increased resolution. Lasers, which emit light in a much narrower band of wavelengths than traditional lamps, allow the researcher to select an excitation region optimized for absorption by fluorescent particles in the sample, resulting in higher

sensitivity, and they allow researchers to avoid wavelengths that may generate interference from other substances in the sample, resulting in higher selectivity[1].

The major difference between a confocal microscope and a traditional light microscope is the small pinhole incorporated into the confocal design. This pinhole allows only light that is in focus to return to the objective. This modification presents a clearer image to the researcher in which small details are more easily discernible, as out of focus light reduces the contrast and resolution of the image[3]. Because of the improved image quality, the confocal microscope has improved penetration into a sample, allowing samples to range in thickness from the 10-15 µm paraffin embedded sections described previously to about 100 µm. A camera records the image obtained from each plane of focus, and the resulting planes can be organized into a three dimensional stack of the sample.

Even though the confocal microscope gains better penetration into a sample than a traditional light microscope, it does so using high energy wavelengths of light. Some of the energy used to illuminate the sample will be dispersed as heat, damaging the sample over a prolonged exposure duration. Multiphoton microscopes overcome this limitation by using a pulsed laser. The laser fires two low energy pulses in quick succession, with the goal of multiple low energy photons hitting the fluorescent molecule nearly simultaneously. The cumulative energy of the photons excites the dye as if it was hit by a single, high energy photon within its excitation range. The lower energy pulses impart less heat into the sample, and their longer wavelengths allow further penetration into tissue. The requirement that two photons strike the same area nearly simultaneously to provide enough energy to excite a fluorescent molecule also prevents the generation of

out of focus fluorescence, obviating the need for a pinhole[6]. Multiphoton microscopes can successfully image over 300 μm beneath a sample's surface.

1.2.2 Transgenic Animals

Many studies attempt to take advantage of fluorescent dyes, however it is not always feasible to inject a dye into the region of interest immediately prior to imaging. In these cases, transgenic animals are used to provide tissue samples. The DNA of these animals is modified to incorporate fluorescent proteins. The proteins' codons are positioned so the cells will transcribe them when prompted to transcribe a native protein that researchers wish to study. In some instances, the fluorescent protein will remain in the cytoplasm of the cell, and cells that produce more of the protein of interest will exhibit an increased fluorescent signal. In other cases, the fluorescent protein can be localized to the same area as the native protein, giving researchers an idea of where the native protein exists in the cell. These methods are useful for studying a very specific cell type in a large amount of tissue, especially when the tissue contains similar cells.

1.3 The Brain

The brain serves as the information processing center of the body, receiving inputs from the nervous system and outputting reactions. The brain also controls involuntary nervous signals such as breathing and heart rate. The systemic consequences damage to the brain can cause make it difficult to study in a living specimen.

In the brains of rodents and primates, the entirety of the cerebrum is covered in a thin layer of cells known as the cerebral cortex. The cerebral cortex varies in depth by species, reaching about 1 mm thick in mice and extending to a thickness of up to 5 mm in humans. The cerebral cortex contains three major groups of neurons: granular, fusiform,

and pyramidal[7]. The types exhibit different morphologies. Granular neurons typically have shorter axons that connect to nearby neurons. The granular neurons act as interneurons, releasing GABA to modulate the excitatory signals of neighboring neurons. Both pyramidal and fusiform neurons output long fibers, but pyramidal neurons tend to be larger and create most of the subcortical fiber bundles.

Even though the cerebral cortex is a relatively thin area, it can be divided into distinct layers. The layers are distinguished by the types of neuronal cells present. Granular neurons tend to populate layers II and IV, while layer III and the deeper layers tend to be composed of pyramidal neurons. Fusiform neurons are located in the deepest layer, VI. The processes extending from the neurons can travel both horizontally through a single layer and vertically across multiple layers. It is most common to see vertical extensions from pyramidal cells, while layers II and IV feature heavy horizontal extensions[7].

The cerebral cortex performs multiple functions. Primary areas of the cortex contain direct connections to peripheral neurons. Secondary areas interpret the incoming and outgoing signals relayed through the primary areas. Association areas perform a mix of primary and secondary functions simultaneously. The Wernicke's area, for example, represents a confluence of somatic, visual, and auditory association areas[7]. When stimulated, Wernicke's area can elicit the formation of complex thoughts. When damaged, recognition of meaning from visual and auditory stimuli can be completely lost.

The prefrontal cortex is another vital association area. Although its previous importance in regards to intellect was likely overestimated, damage to the prefrontal

cortex can cause drastic changes. Patients who have received a prefrontal lobotomy, for example, often exhibit inappropriate social responses, rapid mood changes, and an inability to perform complex tasks and puzzles[7].

While many important functions rely on the cortex, it is literally just the surface of the brain. Many vital functions depend on structures deeper in the brain, such as the thalamus which has a multitude of two-way connections with all areas of the cortex[7]. If a connection between the thalamus and an area of the cortex is broken, the brain loses the ability to perform any function associated with that area of the cortex.

Other vital deep brain structures include the corpus callosum, the hypothalamus, and the hippocampus. The corpus callosum is a large fiber tract consisting of many bundles of myelinated axons. The fiber tract bridges the divide between the left and right hemispheres of the brain. If damaged, information received in only one hemisphere will be unavailable to the other. In extreme cases of damage, an individual may lose voluntary motor control of one side of their body[7].

The hypothalamus is a small area below the thalamus that nevertheless functions as a key component of the limbic system. It is responsible for the vegetative functions of the brain, those dealing with actions such as regulating body temperature and the drives to eat and drink. Damage to the hypothalamus can have severe behavioral effects, either depressing or exciting the patient's appetite and thirst as well as leading to extreme aggression or passivity depending on the location of the damage[7].

The hippocampus is another deep brain structure of great importance. It receives incoming sensory signals and elicits behavioral patterns such as pleasure, rage, passivity, or sex drive. It can become hypersensitive, leading to seizures with auditory and visual

hallucinations. The hippocampus also plays a major role in learning, which has been shown in cases where the hippocampus was partly destroyed, resulting in the patient becoming unable to generate new memories[7]. It is theorized that the excitability of the hippocampus allows it to reinforce memories by repeatedly activating neuronal circuits, stimulating them until the proper chemical and structural changes have occurred to convert short term memories into long term memories.

Through careful case studies, experiments, and histology, the functions of many parts of the brain have been determined. Atlases have also been created that illustrate the shape and placement of major structures in the brain[8]. However, even in mice with their relatively thin cerebral cortex, the deeper structures of the brain remain out of reach for *in vivo* imaging studies. This becomes a problem when the researched events happen in a limited time frame and are best observed in real time.

1.3.1 Traumatic Brain Injury

Traumatic brain injury (TBI) is a serious medical issue dealing with neurological impairments brought on by external forces acting on the body, brain, or spinal cord. It is estimated that 1.7 million civilians in the United States suffer a brain injury each year. This results in approximately 50,000 deaths and 200,000 moderate to severe injuries which require hospitalization. Additionally, $9-10 billion is spent on TBI each year in order to cover injury management, urgent treatment, and disabilities that affect 50% of the survivors of moderate brain injury[9]. The brain consists of many different cell types, all of which communicate with one another. Important examples are neurons, astrocytes, microglia, oligodendrocytes, and endothelial cells. When TBI occurs, losses occur across all cell groups.

The initial mechanical insult generated by TBI will disrupt the plasma membrane of the cells that undergo mechanical stress. These cells are no longer capable of maintaining homeostasis, and neurons in the injured population, unable to keep their ions balanced, will depolarize. This leads to a calcium cascade, exacerbated by the depolarization of nearby axons and oligodendrocytes. The now free-floating calcium ions will be taken up by previously undamaged cells, compromising the function of the mitochondria within and initiating apoptosis. Axons that were disrupted in the initial insult are likely to fragment completely, preventing the restoration of disrupted neural networks. The end result is a primary injury caused by a mechanical insult, followed by a much larger secondary injury caused by the uncontrolled release of neuronal signaling factors[10].

The effects of different levels of TBI are often studied through behavioral tests. Any underlying physical condition can only be determined through histology days to weeks after the initial insult, making it impossible to study the healing process, or lack thereof, as it happens. However, increased awareness of TBI incidence has led to an urgent need to better understand the condition and develop treatment options[11]. The research presented in this dissertation will provide a means for longitudinal imaging of the deeper structures of the brain *in vivo* using a gradient index (GRIN) lens. This imaging system will allow for an improved quantification of damage over time and provide a means for determining the effects of pre-clinical trials in real time.

CHAPTER 2

LITERATURE REVIEW

2.1 Introduction

The basic methods described in Chapter 1 have been refined and applied to further the understanding of both the brain's architecture and its dynamic functions. These applications are spurred by the need to better understand the critical organ's disease states and the events that occur during and in the aftermath of trauma, in the hopes that a better understanding will provide better avenues of treatment. Some of the techniques are also applied to study the impacts of experimental treatments in pre-clinical trials and determine their potential efficacy. Despite incredible advancements in imaging techniques, it can still be incredibly difficult to study dynamic events with the resolution required to observe changes at the cellular level. This chapter will review techniques that have been used to observe such phenomena, and discuss their limitations. This chapter will focus on experiments involving mice and rats because these models are widely used in brain studies for basic science and pre-clinical trials.

2.2 *Ex Vivo* Imaging Techniques

Imaging that occurs *ex vivo* is still widely used in scientific research. Historically, these techniques have used a microtome to section the brain, followed by mounting the tissue on a slide and staining. However, *ex vivo* imaging has expanded as imaging

technology evolved, including the ability to cut and analyze thicker slices of brain, tissue clearing techniques, and whole mount imaging.

The basic methods of histological and immunohistochemical staining were described in Chapter 1. This chapter will be more concerned with the application of these techniques. Brain atlases, some of the most important resources in neuroscientific research, were created using such techniques. For example, when creating their Mouse Brain Atlas, Paxinos and Franklin used both colorimetric and immunohistochemical stains to aid delineation of structures in the brain, including cresyl violet stain, a reaction to reveal acetylcholinesterase, as well as immunohistochemistry to reveal parvalbumin amongst others[12]. The advantage of using traditional histology is the long shelf life of fixed tissue samples. Such samples can be viable for weeks to years after collection, depending upon the storage conditions and the staining method. However, the sheer number of samples generated can be daunting. Sections must be incredibly thin to allow a suitable amount of light to pass, typically around 10-15 μm in thickness, and, in some cases, as little as 50 nm thick[13]. The adult mouse brain measures roughly 8 mm across and 15 mm along the rostral-caudal axis[12], meaning a single brain could contain 800-1500 sections depending on the direction of sectioning. Additionally, because the sections are fixed, it is impossible to capture rapidly occurring dynamic events. Those events that can be captured require many animals to be sacrificed because one animal is required for each time point and because variances between animals must be ruled out.

One strategy researchers use to keep larger regions of the brain intact is to optically clear the tissue. Tissue extraction and preparation is similar to the method used for traditional histological staining, however it is unnecessary to infuse or embed the

specimen in paraffin. Instead, the tissue is immersed in chemicals such as tetrahydrofuran (THF), dibenzyl ether (DBE), or BABB (a 1:2 solution of benzyl alcohol and benzyl benzoate) which remove lipids from the cells and match the cells' refractive index[14]. Detailed descriptions of clearing protocols such as CUBIC[15], CLARITY[16], and iDISCO[17] can be found in the literature. The clearing protocols allow light to penetrate much further into the tissue (up to 2 mm in some cases[14, 18]). When used in conjunction with fluorescent labelling techniques, such as dye tracing, transgenic animals, antibody labelling, or viral transfection[14], optical clearing allows researchers to observe specific parts of the brain without damaging or deforming the surrounding architecture. The structural continuity also provides the opportunity to capture elongated structures, such as axons, that may travel in and/or out of a thinly sectioned plane.

A consequence of working with fixed tissue is that sample is taken from a deceased subject. The loss of nutrients and buildup of cellular waste following death can affect the condition of the tissue, by either inducing stress reactions in the cells or apoptosis. These reactions can create a radically different environment than the normal *in vivo* conditions if allowed to persist. Perfusion with a chemical fixative is used to halt such processes, however complete perfusion of the tissue can take hours. Cells distant from the blood vessels used to circulate fixative during perfusion or distant from the edges of the tissue during immersion will be the last to come into contact with the fixative, and consequently the most affected by damaging cascades. To work around this problem, researchers may attempt to extract tissue before the systems that maintain it cease to function. With such methods, the tissue can be kept viable through the use of

commercially available or custom built circulation devices, which perfuse a small bath of artificial cerebrospinal fluid with the appropriate amount of gaseous oxygen (95%) and carbon dioxide (5%).

The first of these methods is somewhat similar to traditional histology, in that researchers cut the brain into slices to be analyzed. However, these slices are still composed of living tissue, and a vibratome is used in place of a microtome. Slices cut in this manner are much thicker than those used in traditional histology, ranging from 0.4 to 40 mm. Using this method, a closer approximation of the *in vivo* environment can be studied, as well as dynamic events such as cell motility. For example, Rachel James et al. have used this method to study the migration of fluorescently labelled neuronal stem cells along the rostral migratory stream (RMS) in the mouse brain[19]. By slicing the brain to expose the RMS, James et al. were able to use two-photon microscopy to record the movement of labelled neuronal precursors in a tissue sample taken from a transgenic mouse. In doing so, they were able to observe the morphology and motility of the cells, as well as the areas in which migration occurred. The events took place over the hours spent imaging, indicating that it would be nearly impossible to observe similar outcomes using fixed tissue.

Whole mount imaging is another popular method of tissue preparation, especially regarding structures with complex or extensive shapes. Whole mounts attempt to preserve the architecture of a region by removing only as much tissue as is necessary to expose it. One of the method's most common applications is in the study of the subventricular zone (SVZ) and the associated migration of neuronal precursors from the region. In rodents, the SVZ is a germinal region along the walls of the lateral ventricle.

Chain migration from this region allows neuroblasts to reach the olfactory bulbs, where they mature into neuronal cells[19]. By immunostaining fixed whole mounts for the proteins PSA-NCAM and TuJ1, Doetsch and Alvarez-Buylla were able to show the extent of these chains in a murine model[20]. Doetsch et al. would also later show that the SVZ was composed of three primary cell types[21], however this research was done using ultra-thin sections, obscuring the true morphology of the cells. By immunostaining fixed whole mounts of the mouse lateral ventricle for beta-catenin, gamma-tubulin, and glial fibrillary acidic protein (GFAP), Mirzadeh et al. were able to both generate a better understanding of the organization of cells previously described by Doetsch et al., and reveal extended processes connecting the cells to nearby blood vessels[22].

The whole mount method is not limited to fixed tissue. Using fluorescent microbeads, Mirzadeh et al. were able to demonstrate the ependymal flow influenced by ciliated ependymal cells around the ventricles[23]. Similarly, living whole mounts have been extracted after experimental stroke to study the changes in ependymal flow after restructuring of the area[24].

Unfortunately, both brain slicing and whole mount imaging suffer from some of the same deficits that affect traditional fixed histology. While the architecture is largely preserved, especially in whole mount preparations, and the study of dynamic events is possible, both methods are limited to the amount of time researchers can keep the tissue alive after extraction. This time limitation forces researchers to incorporate additional mice for longitudinal experiments, and introduces the possibility of variation between animals. Additionally, perfusion of the tissue is extremely inhibited by the lack of a functioning circulatory system. Cells near the surface may continue to be perfused by lab

equipment, but many cells in the interior of the tissue will slowly die. This introduces a number of additional variables that would not be encountered *in vivo*.

2.3 *In Vivo* Imaging Techniques

The most straightforward way to view events occurring in the brain without the drawbacks of excising tissue is to simply image the tissue in a living subject. Attempting to image such a critical and protected structure *in vivo* carries with it many difficulties, most importantly the prevention of compromising tissue function in order to observe the region of interest. A variety of imaging techniques have been developed for this purpose, ranging from minimally invasive magnetic resonance imaging procedures (MRI) to more invasive surgical procedures that expose a portion of the brain through a craniectomy.

MRI is a non-invasive imaging technique that relies on the response of hydrogen atoms to powerful magnetic and radio frequencies to create an image of the exposed area. The wavelengths can penetrate biological tissues, removing any need to surgically expose organs. However, MRI alone is incapable of detecting a single cell. In order to visualize single cells, researchers applied *in situ* injections of superparamagnetic iron oxide (SPIO) particles as contrast agents. Shapiro et al. demonstrated that cells incorporating these particles could be detected with MRI by injecting the particles into primary mouse hepatocyte cells and transplanting the labelled cells into host spleens[25]. By also labelling the cells with fluorescent agents, Shapiro et al. were able to histologically confirm that the cells detected by the MRI were the transplanted hepatocytes.

Similar techniques have been used to track neuronal precursor cells (NPCs) in rodent models. Shapiro et al. injected the SPIO particles into the lateral ventricle, allowing the contrast agent to be taken up by cells in the SVZ[26]. As the cells migrated

along the RMS, the contrast agent was visible as a large dark shape filling the injected ventricle, with a smaller black line emanating from the structure and following the RMS into the olfactory bulb. This technique has continued to be refined in the literature, with subsequent authors modifying the injection site and the size of the particles used. A review by Mallett et al. includes a table containing information such as the animals used in replications of the technique, injection volume, and injection location[27].

The largest advantage MRI has over previously described techniques is its non-invasive nature. The reduced surgery and lack of permanent implant removes most of the threat of infection. As with the other *in vivo* techniques that will be discussed, the nature of the experiment allows data to be collected at multiple time points from a single animal, and the speed of capture allows researchers to observe dynamic events, such as cell migration. However, MRI has drawbacks. The artifact created by the SPIO particles is typically much larger than the particle itself[27]. While this is important for the device's ability to detect labelled cells, it significantly limits the available image resolution. As valuable as it is for detecting the location of labelled cells in living tissue, MRI is still incapable of revealing the morphology of cells.

A second and equally important issue is the specificity of cell labelling. The SPIO uptake depends on simple phagocytosis of the particles by nearby cells. Studies have shown that astrocytes will always consume an initial percentage of the particles, and that an increase in time post injection or an increase in distance from the injection site directly relates to the amount of non-neuronal cells containing SPIOs[28, 29]. These additional cells are often microglia, which either directly consume free floating SPIOs or ingest the particles through pruning of migrating NPCs. The lack of specificity

introduces uncertainty into the experiment, forcing researchers to either include a second label that is later analyzed through traditional histology or to interpret their results based on the behavior of the cells containing the SPIO particles.

More invasive methods, such as thin skull windows and craniectomies, allow researchers to employ the advantages light microscopy has over MRI while still working in an *in vivo* model. Much like MRI, these techniques allow repeated imaging of a single animal. However, while MRI is largely dependent on the contrast created by SPIO particles, a much wider array of dyes and fluorescent molecules with greater specificity for certain cell types or free ions can be detected with light microscopy. Using light microscopy also overcomes the limited resolution of MRI, allowing researchers to visualize not only single cells, but also smaller structures such as axonal projections and even dendritic spines of neuronal cells.

The literature contains extensive protocols on both thin skull windows, and cranial windows that employ a complete craniectomy[30-34]. The procedures are similar, typically only differing in that a thin skull window, as the name implies, does not completely penetrate the skull, instead using a handheld drill to thin the bone until it is optically clear[32]. Cranial window procedures remove a portion of the skull entirely, also granting researchers the option of removing the dura covering the brain. When used with multiphoton microscopy, a thin skull window may allow up to 300-400 μm of light penetration below the cortical surface[31], and cortical depths greater than 600 μm have reportedly been reached using cranial windows[30]. A thin skull window carries with it a much smaller chance of immune response due to lesion, however it risks bone regrowth

or light scattering by irregularities in the thinned surface. These risks can be mitigated by attaching a cover glass over the thinned region[32].

Thin skull windows and cranial windows have been used to study a wide array of phenomena in the cortex. Yang et al. used Thy1-YFP positive transgenic mice to study changes in dendritic spines over time, as well as a CX3CR1-EGFP line to study the morphology of microglia[31]. Shih et al. were able to demonstrate the orientation of YFP-positive neurons in a transgenic mouse line and their relation to nearby vasculature by also including a tail vein injection of Texas red dextran[32]. By developing a removable cranial window, Goldey et al. were able to create a model for targeted injection of AAV-GCamp3, a viral transfection for a genetically encoded calcium indicator, to study calcium dynamics in cortical axons[33].

Both invasive and non-invasive *in vivo* methods offer distinct advantages over their *ex vivo* counterparts. *In vivo* methods can repeatedly image a single animal, allowing easier study of longitudinal changes. These methods also reduce the amount of damage to the organism, presenting a model much closer to the cell's *in vivo* environment. However, their disadvantages are apparent. While they have nearly unfettered access to any region of the brain, non-invasive methods like MRI cannot specifically label target cells or resolve smaller objects such as cell bodies or fine processes. Thin skull and cranial windows, on the other hand, have access to labels with great specificity and are capable of detecting objects less than five microns in size, but are limited to the penetration depth of light into the tissue. To better understand the dynamic relationship between architecture and function in deeper areas of the brain, such

as the SVZ, researchers were forced to continue developing advancements in imaging technology.

2.4 *In Vivo* Imaging with Gradient Index Lenses

Advances in endoscopy allowed the formerly low resolution technology to meet the high resolution needs of imaging research. Successful imaging through an optical fiber attached to a confocal microscope was first reported by Ghiggino et al. in 1992, with the intent of using the flexible fiber to reduce the number of optical components necessary for excitation source redirection[35]. Over the next decade researchers would improve on this design, seeing the potential not only in reducing bench space dedicated to confocal setups, but also in the impact on *in vivo* research[36-38]. Much like in its already extensive medical use, the extended conduit provided by the optical fiber would allow researchers to extend their field of view to areas previously only accessible through excision and extensive preparation of tissue.

Unfortunately, researchers encountered problems when they attempted to apply endoscopy to multiphoton imaging. The femtosecond pulses necessary to excite fluorescence in multiphoton imaging would degrade over the length of the optical fiber, increasing from 100 fs to anywhere from 0.2-1 ps after 1 cm of travel[39]. This problem was not overcome until 2003, when Jung and Schnitzer published a microendoscopic system based on gradient index (GRIN) lenses[39]. GRIN lenses are glass cylinders doped with radially incremented metal ions, allowing the devices to bend collimated light as it passes axially, focusing it a working distance from the opposite face. Jung and Schnitzer developed multiple compound, triplet GRIN lenses totaling 0.9-2.6 cm in length and 350-1000 μm in diameter, and demonstrated their effectiveness by imaging a

neuron and its dendrites in prepared slices from a zebra finch[39]. The next year, Levene et al. published the first *in vivo* demonstration of the triplet GRIN lens; they fabricated a 16 mm compound lens and partially implanted the device through a craniotomy to image YFP-containing cell bodies up to 1.5 mm below the surface of the cortex of an anesthetized mouse[40].

While such advances were impressive, the lenses themselves were much too large and fragile to chronically implant in most research animals. Additionally, the metal sheath Levene et al. used to protect the lens from mechanical damage increased the diameter of the implant, requiring aspiration of the tissue to facilitate implantation. The lenses also suffered from severe distortion in the axial direction, up to 12-15 μm in length[40]. These problems were mitigated through the introduction of the singlet lens. In the system described by Murray and Levene in 2012, the singlet lens used was less than 2 mm in length and only 500 μm in diameter[41]. The researchers further developed the implant by including a cover glass, introducing negative spherical aberrations to counter the positive spherical aberrations created by the GRIN lens, with the intent of reducing the axial distortion. Murray and Levene showed a reduction in axial distortion of their implants compared to a singlet lens alone without introducing additional lateral distortion. The researchers were also able to perform *in vivo* imaging with their lens, capturing high resolution images of Thy1-YFP expressing neurons, including fine processes less than 1 μm in size[41].

2.5 Conclusion

Although advancements in imaging technology have created a number of tools researchers can use to investigate brain structure and function, dynamic events are still

difficult to study, especially those that occur in multiple phases over an extended period of time. Research into disease states such as stroke, which involves mass infiltration of microglia and associated morphology changes, and events such as traumatic brain injury, which can cause multiple stages of tissue loss, greatly benefit from longitudinal studies. However, such studies are currently inhibited by the number of animals required to adequately study events that have both immediate and lingering effects, especially when testing a possible treatment.

The development of the GRIN lens presents an opportunity to create a low profile, chronic implant for longitudinal studies of such events. Such an implant would drastically reduce the number of animals used in these studies, as data could be obtained *in vivo* without requiring the sacrifice of subjects at multiple time points. The GRIN lens can also capture high resolution images of subcortical regions of the brain, greatly expanding the regions that can be accessed by *in vivo* light microscopy.

The research presented in this dissertation created this low profile, chronic implant and used it to repeatedly acquire images over an extended period of time without degradation in quality. The developed device drastically reduced the size of implant both above the skull and within the brain tissue compared to previously reported GRIN lenses, while still obtaining the expected high resolution images. This research also found that labelled axons in transgenic mice appear in unique, recognizable patterns which remain consistent over months of imaging, meaning future studies may use the axons themselves as landmarks. Using the axons as landmarks obviates the need for vascular dye injection.

CHAPTER 3

DEVICE DEVELOPMENT

3.1 Initial Implant Design

Three aims were set for the design of the GRIN lens implant. The first was that the implant must be low profile and low weight. A low profile and low weight device was less likely to catch on the cage elements, or to accidentally be removed through grooming behaviors. Lower weight would also decrease the stress on the mouse, and minimizing the size of the implant would allow more room to remain for additional implants to be incorporated.

The second aim was to prevent a negative response from the tissue due to contact with the implant. Stainless steel and glass were the only materials used in the implant, as both are known to be largely inert when in contact with tissue. Finally, the third aim was that the implant had to be placed stereotaxically. The stereotax is a surgical frame with an attachment that can be moved in precise increments. The implant would have to be compatible with this attachment, so it could be reliably placed in the same region.

The initial implant was designed to mimic the headplates found in the literature[42-44], which were used to secure mice in place during imaging of cortical regions through cranial windows. It consisted of a nearly flat metal rectangle 20 mm in length, 7.20 mm in width, and 0.60 mm in height. A powered hand tool (Dremel) was used to further machine the headplate to include a cutout that allowed light to pass

through to an attached GRIN lens in the medial/caudal area of the implant. The rostral edge of the implant was ground down to create a small shelf, creating increased surface area for the polymer adhesive that would bind the headplate to the skull. A three dimensional model of the headplate design with an attached GRIN lens is shown in **Figure 3-1**.

The initial implant design was difficult from the beginning, as the only multiphoton microscope available at the time was an inverted Leica microscope better suited for imaging plated cells. The need to securely hold the animal's head against the force of gravity greatly affected the implant design, and the exact method for holding the animal in place was still in the planning process when the lab secured funding for an upright microscope system which would be dedicated to the multiphoton laser. This greatly eased the process, as it meant only the head needed to be rotated to align the lens while the animal's body rested on the stage. An initial prototype accomplished this by attaching a bulldog clamp to a pitch and yaw platform (Thorlabs) installed on a post screwed into the stage.

Unfortunately, even with the switch to an upright microscope the initial design proved unsatisfactory. The implant was nearly impossible to place stereotaxically with the equipment available at the time, which prevented reliable placement of the lens in a desired brain region and meant the design failed the third specific aim. Additionally, the headplate acted as a lever arm that greatly reduced the amount of force it took to separate the implant from the skull, often so much so that the force required to separate the implant was lower than the amount required to adjust the mouse's head under the objective. This situation was untenable, as it meant the implanted lens could not be

aligned with the laser beam, drastically reducing imaging quality when not eliminating the capability completely. Based on these difficulties, it was decided that the implant had not satisfactorily met the first aim, and that more focus would be applied to lowering the implant's profile.

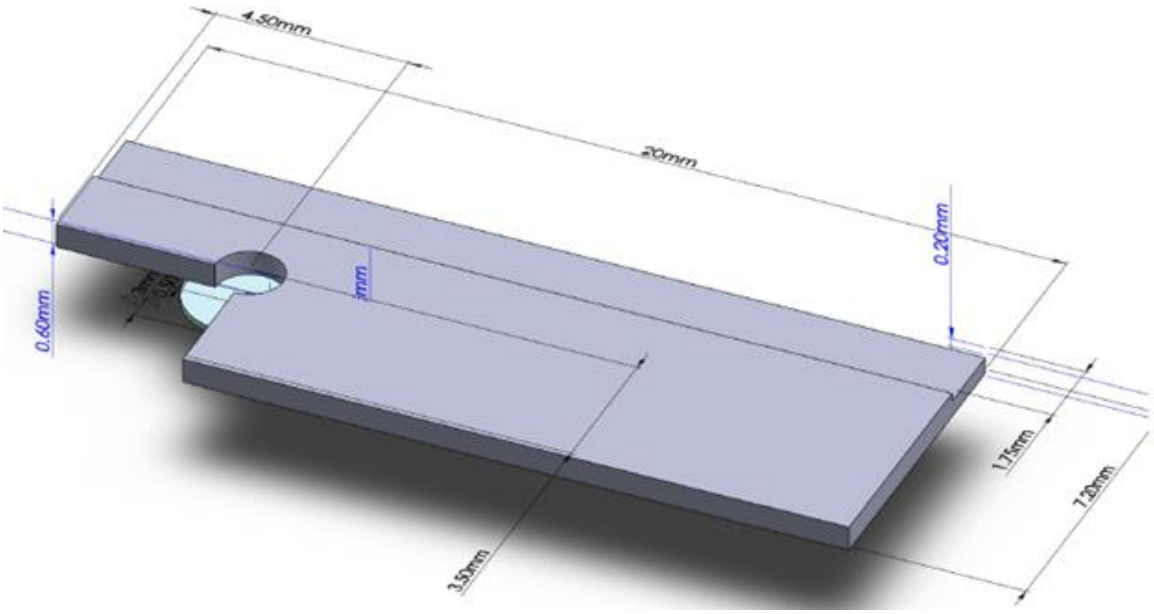

Figure 3-1: Three dimensional model of the initial implant design. The GRIN lens is attached to the cover glass beneath the metal bar so that it may be inserted through a craniectomy.

3.2 Revised Implant

The next iteration was drastically different. It was designed with the knowledge that it could be incorporated into an upright microscope, which expanded the pool of functional designs. Instead of a headplate that extended beyond the skull, the implant was a simple ring, which was less likely to be detached due to its lower profile and easier to reliably replicate on a benchtop lathe (Grizzly). The implant no longer needed to be secured with a clamp or a screw, but instead could be held magnetically in a similar fashion to a previously reported GRIN lens implant[41]. With that in mind, the implant

made from 400 series stainless steel round stock (McMaster-Carr), which is innately ferritic. The revised implant design with measurements is shown in **Figure 3-2**.

Stereotaxic implantation was possible with the new design using a cannula holder attachment. The implanted lens itself was also slightly redesigned to be more modular. A glass window, used both to increase the depth the lens reached and to provide negative spherical aberration, was added between the lens and the cover glass.

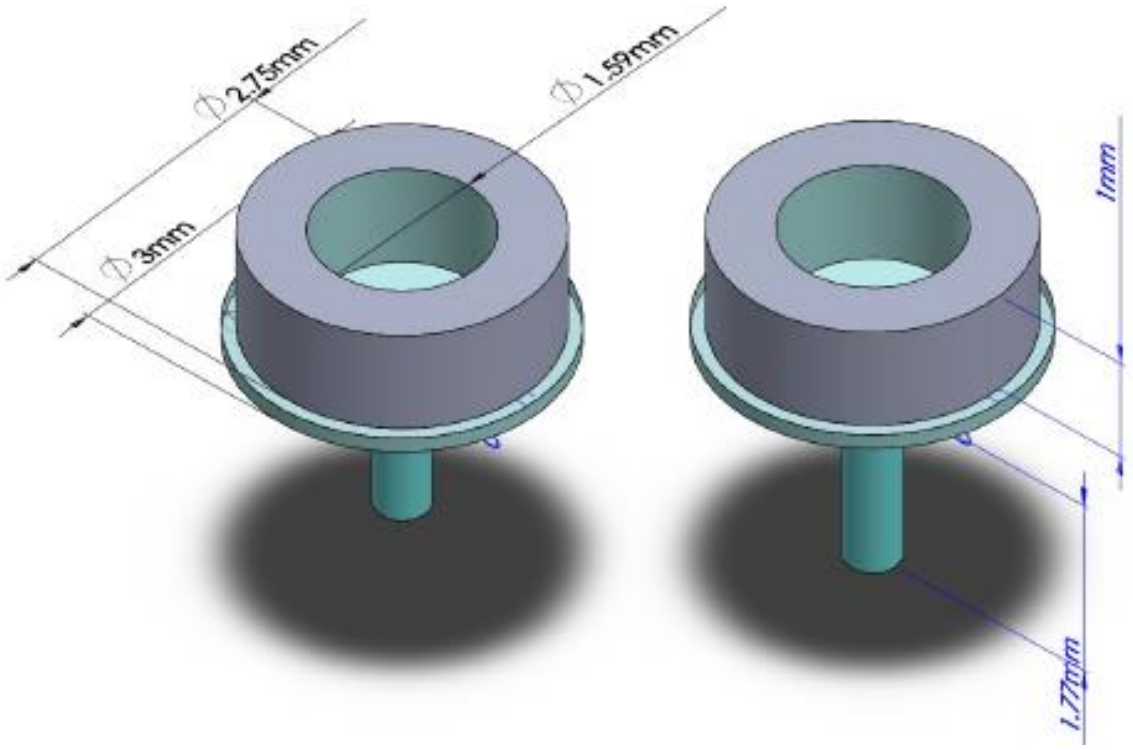

Figure 3-2: Revised implant design with measurements. The model also depicts the implant with and without the glass window.

3.3 Histological Analysis

To verify that the lens had achieved the desired penetration into the brain, mice were sacrificed post-op and prepared for histological sectioning. Mice were anesthetized and perfused using phosphate buffered saline followed by formalin fixative. The sample

was removed and allowed to sit in formalin overnight before being prepared for paraffin embedding. Once embedded, tissue samples were sectioned on the microtome in the core histology facilities and mounted on glass slides.

Hematoxylin and eosin (H&E) staining, luxol fast blue and cresyl violet staining, and Gomori trichrome staining were used to examine sectioned tissue. H&E staining did not distinguish the region of interest, while luxol fast blue and Gomori trichrome did. However, Gomori trichrome is the less specific of the two stains.

Gomori trichrome distinguishes different structures as a result of the large difference in size of its component dye molecules. The three components of this particular Gomori trichrome stain are Fast Green FCF, Chromotrope 2R, and hematoxylin. The Fast Green FCF (MW 808.85 g/mol, Sigma-Aldrich) dye molecule is roughly twice the molecular weight of the Chromotrope 2R (MW 468.37 g/mol, Sigma-Aldrich) molecule. The larger dye molecules will displace their smaller counterparts in areas of the tissue where the remaining protein network is less dense. Areas of higher protein density will prevent the larger molecules from penetrating, allowing the Chromotrope 2R dye to remain in place. Fortunately for this research, this resulted in Chromotrope 2R staining only the myelinated areas of the tissue samples, such as the corpus callosum and external capsule. The staining of these tissues provided a clear image of the depth of the implanted lens in relation to the structures of interest, which is shown in **Figure 3-3**.

The luxol fast blue with cresyl violet counterstaining protocol was used to label structures with greater specificity. Luxol fast blue is used to highlight myelinated regions. Cresyl violet stains the Nissl material found in neurons, granular bodies that are

comprised of rough endoplasmic reticulum. This staining method was used to clearly identify the axons in the corpus callosum and external capsule. The cresyl violet counterstain allowed visualization of neuronal bodies in addition to providing background staining to contrast the luxol fast blue. An example of luxol fast blue and cresyl violet staining is shown in **Figure 3-4**.

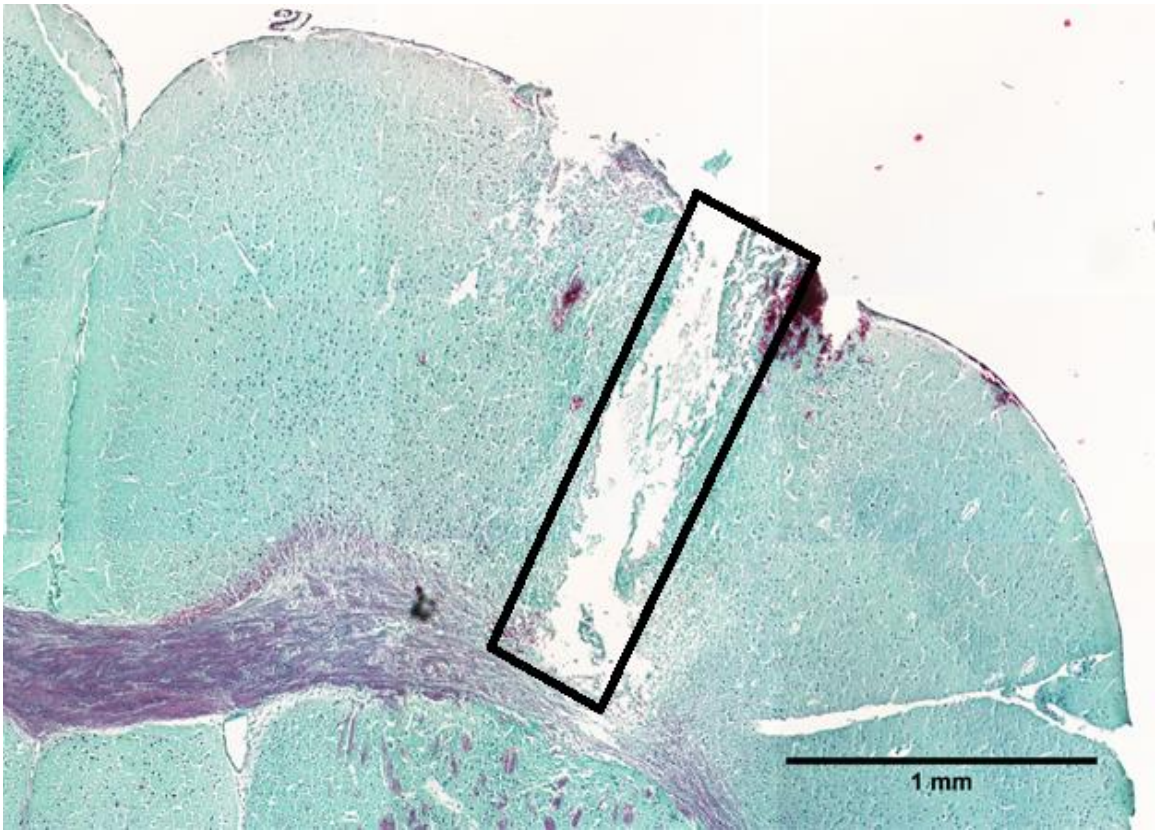

Figure 3-3: Coronal section of an implanted brain stained with Gomori trichrome. The smaller dye molecule results in a light purple stain in myelinated regions, such as the corpus callosum and external capsule. Regions with less dense protein networks, like the cortex, are stained green by the larger dye molecule. Hematoxylin staining shows nuclei. The rectangular void (boxed) indicates the depth the implanted lens reached before removal.

Hematoxylin and eosin stains are also highly specific, but they do not easily distinguish the regions of interest. Hematoxylin is a cationic dye molecule that binds to negatively charged DNA in the cell nucleus. Eosin is an anionic molecule that binds to

proteins in the cell cytoplasm. The result is a sample with darkly stained nuclei and a lightly stained background. The H&E protocol is one of the most commonly used staining methods in biological research for good reason, however, unlike Gomori trichrome and Luxol fast blue with cresyl violet, it created a homogeneous image. Though the dyes bind to specific components in the cell, those components are present in cells throughout the brain. The alternative staining methods provided images that could be rapidly analyzed.

Figure 3-4: A coronal section of mouse brain stained with luxol fast blue and a cresyl violet counterstain. The luxol fast blue stain labelled myelinated areas of the section, while the cresyl violet stain associated with Nissl material. This allowed the corpus callosum and external capsule to be easily distinguished from the surrounding tissue with greater specificity than Gomori trichrome could provide.

3.4 Implant Microscope Interface

Successfully implanting the lens into the brain over the target region was only the first step in acquiring images. The implant had to be developed simultaneously with an interface that would allow the lens to be aligned with the microscope objective. However, the interface carried its own set of specific aims. The first was that the interface would need to align the lens beneath the microscope objective. The GRIN lens has a low tolerance for misalignment, with consequences including a diminished field of view, objects in the field of view perceived with stretched dimensions, or total internal reflection. In order to keep the lens aligned, the interface would also have to be somewhat adjustable, to account for the slight differences that might occur in animal size.

The second aim was that the interface needed to restrain the mouse during imaging. Although the mouse is sedated, the act of breathing still creates small amounts of motion. While the head may seem largely motionless to the naked eye, under the microscope even the slightest displacement can result in drastically decreased image quality. It was imperative that the interface restrain the mouse in a way that prevented head motion artifacts without restricting the animal's breathing.

The third aim was targeted at supporting the animal during imaging. Anesthesia and heat delivery were a major concern during design. The interface would have to allow for monitoring of the subject's level of anesthesia, and updates, should they be necessary. Gas anesthesia delivery would have been optimal, however, due to equipment limitations, the interface was designed for delivery by an intraperitoneal injection of a ketamine xylazine cocktail. The interface also needed to incorporate a heating element to prevent the animal from becoming hypothermic while sedated.

The final, and most straightforward aim was that the interface must fit within the limited space provided by the microscope stage. No matter how well it met the other aims, if the interface couldn't fit on the stage or prevented the microscope objective from moving within its focal length, it would be a failure. **Figure 3-5** depicts the microscope stage and the working distance of the objective used.

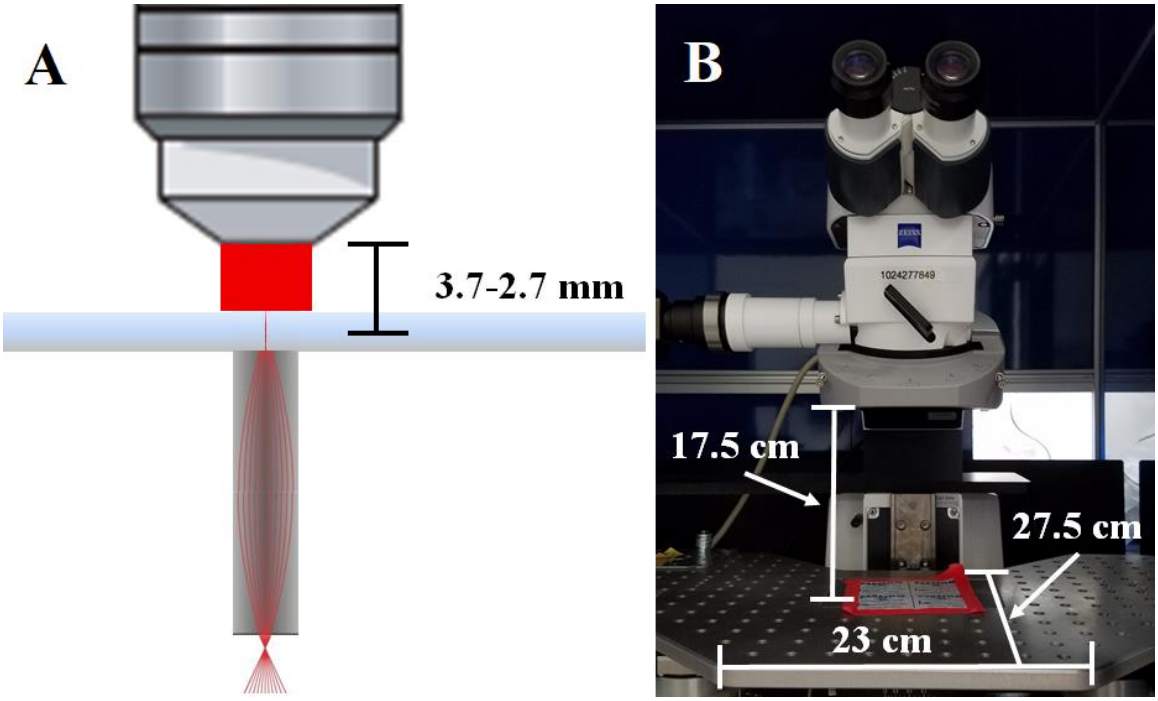

Figure 3-5: A depiction of the working distance of the 40x objective and the dimensions of the microscope stage. The objective used had an extremely long working distance, but still required close proximity to the GRIN lens. The maximum height between the microscope and the stage is shown, but was reduced considerably by the safety shutter and objective lens (not shown). These components needed an additional 8 cm of space.

The interface design is shown in **Figure 3-6**. Two long bars and a short cross piece were modeled in SolidWorks. The designs were then given to Dr. Louis Reis, who converted the .stl files into g-code which could be interpreted by the Tormach CNC machine. The converted files were used to cut the design out of an aluminum block.

The interface is designed to be as open as possible in order to prevent contact with the animal's body. The two long bars were raised from the microscope stage on stacks of metal washers and held in place with metal screws, which matched the ¼"-20 holes in the microscope stage. While inelegant, this design allowed the total height of the interface to be adjusted incrementally as needed. Each long bar contained a cut out section to accommodate a shorter cross piece. The animal's head would be placed under this cross piece, propped up using a small piece of packing foam.

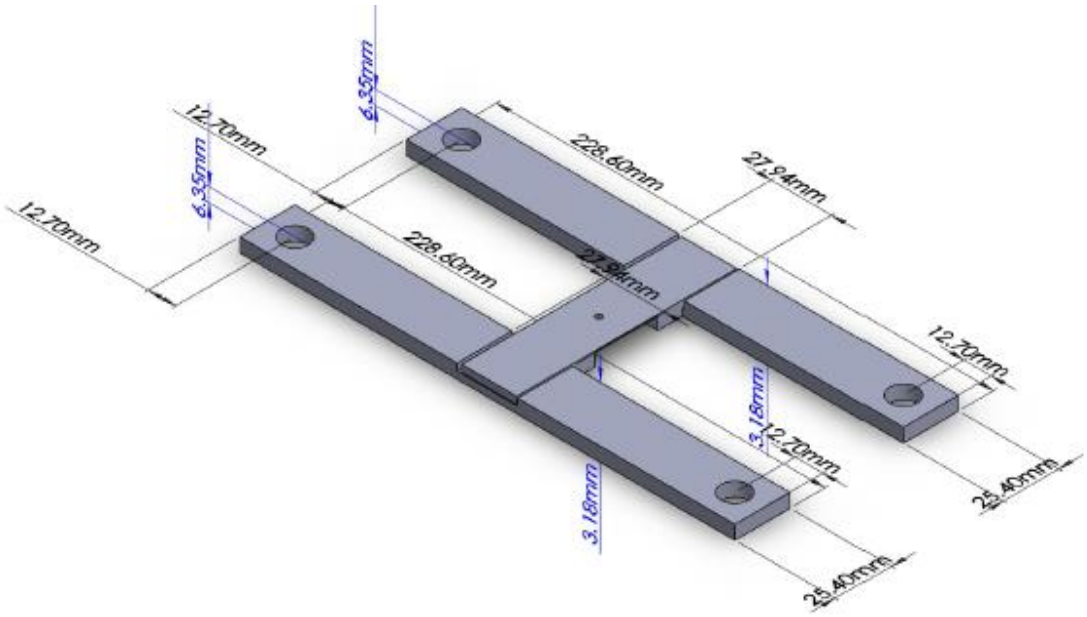

Figure 3-6: A three dimensional model of the microscope stage interface used to position the lens implanted in an anesthetized animal with the laser beam. Screws passed through the four corner holes to hold the interface in place on the microscope stage.

A hole was cut through the crosspiece at its center. This hole allowed light to pass through to the GRIN lens, then back to the imaging system. A small socket on the underside of the crosspiece prevented the lens from sliding out of the light path. The crosspiece was held firmly in place against the two long bars using tape. Because the

interface was level on the microscope stage, as long as the implant was firmly held against the crosspiece, the lens was aligned with the beam path.

3.5 TRIO System Incorporation

Although it functioned as desired for image collection, the initial interface had drawbacks. The interface contained no heating element for anesthetized animals, and instead relied on a borrowed electric heater. The design also made it difficult to incorporate gas anesthesia, which equipment upgrades in the lab eventually made possible to use during imaging as well as surgery.

Developed by Vlad Voziyanov for his own research, the TRIO system (**Figure 3-7**) solved many of these problems with only minor modification to accommodate the previously designed implants. The TRIO system incorporated a restraint system that also aided lens alignment, a water based heating system, and a nose cone for the delivery of gas anesthesia. It was 3D printed rather than machined.

The main consideration in switching to the TRIO system was reformatting the system to incorporate the previously shown GRIN lens implant as opposed to the intended head plate. Vladislav's experiments attached a full head plate to the skull, however this proved less reliable than the low profile implant. The head plates, much like the first iteration of implant shown previously, provided a large lever arm that led to many of them being removed prematurely. The lack of curvature also made it difficult to successfully implant lenses in lateral regions of the brain.

The solution was to create a new crosspiece that could fit into the arms meant to secure the head plate, but would also provide a socket to catch the low profile implant and hold it in place. This crosspiece design is shown in **Figure 3-8**. The new crosspiece

design also incorporated a thin, ring-shaped neodymium magnet. The force from the magnet, though not enough to hold the animal's head in place, provided slight assistance to the researcher. As with the previous interface, a small cushion was also placed beneath the subject's head to hold it against the crosspiece.

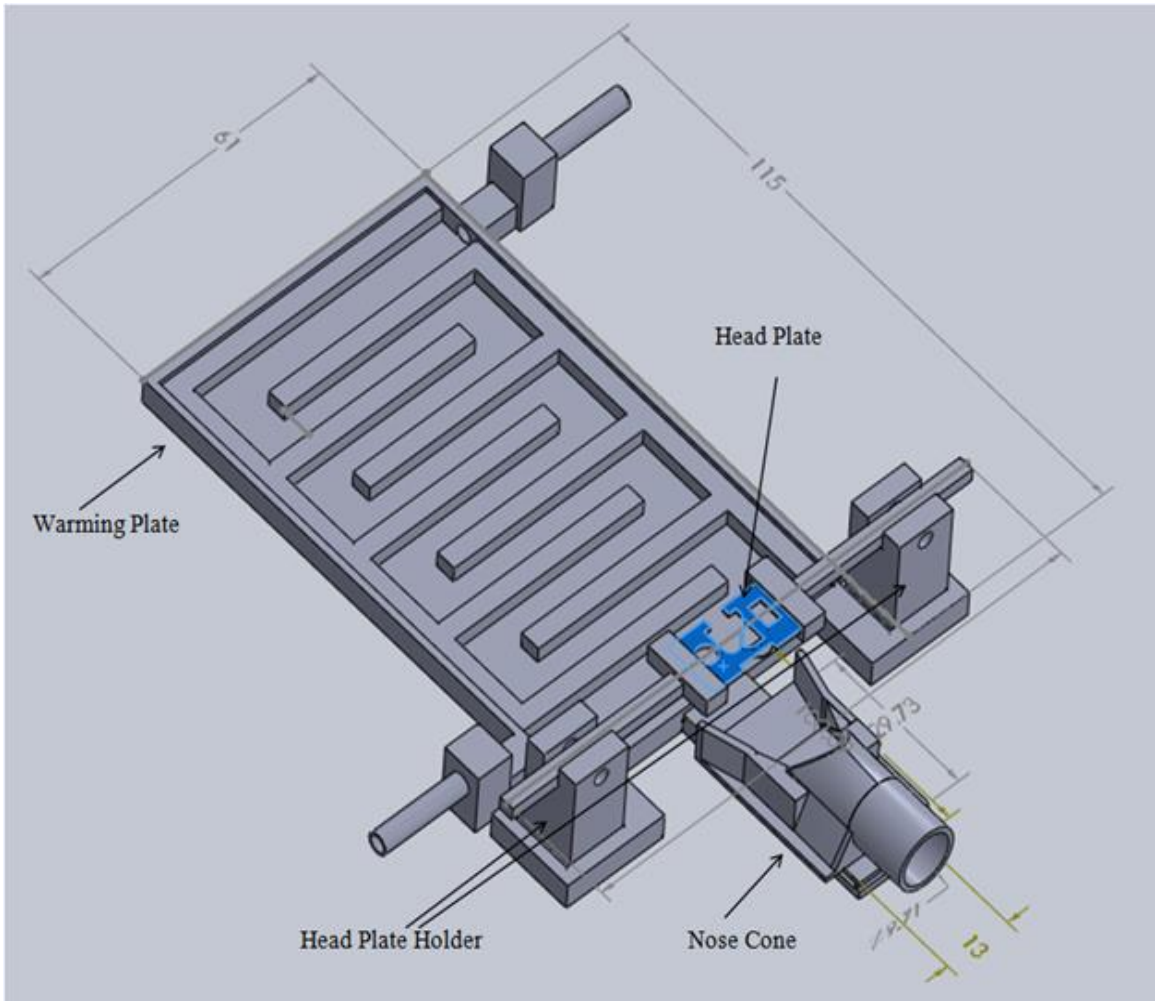

Figure 3-7: A three dimensional model of the TRIO system designed by Vlad Voziyanov[45]. The system contains an interface to hold the animal's head in place, a delivery port for gaseous anesthetic, and a channel where heated water can flow beneath the animal.

The crosspiece was machined rather than 3D printed to aid in positioning the objective over the lens. It was common for researchers to use a fluorescent lamp attached to the microscope to find and focus on the lens. The fluorescent light provided a visible

point that could be positioned over the hole in the crosspiece using the naked eye. The top of the lens would also reflect back some light, appearing green through a GFP filter while the surrounding area was dark. This method of finding and focusing on the lens proved both reliable and useful, however the plastic used in 3D printing produced a similar effect when exposed to fluorescent light. Instead of seeing a clear depiction of the lens, researchers would see only a field of green light. When a metal crosspiece was used, the field of green light disappeared, making it the slightly more challenging process of machining a metal crosspiece the superior option.

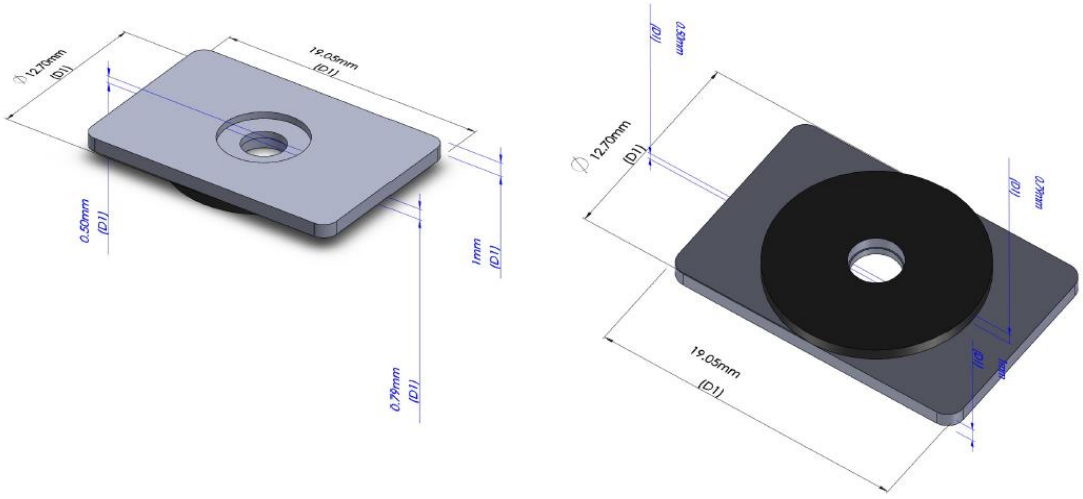

Figure 3-8: A three dimensional model of the metal crosspiece used to integrate the low profile implants with the TRIO system, with top and bottom views. The bottom of the crosspiece (left) included a small indentation that helped keep the implant from slipping along the surface. The top (right) included a small magnet, represented by the dark disc, to attract the implant.

3.6 TRIO System Heated Plate Test

During development of the TRIO system, the heated system was tested to ensure the appropriate amount of heat was delivered to the sedated mouse. A total of three tests were performed by Ben Kemp with the assistance of Kayla Ponder. The complete test results are available in the appendix, but a description of the tests is presented here.

The base of the TRIO system is a sealed chamber which allows heated water to run through multiple lanes beneath the animal. The direction of flow was dependent on the manner in which the pump was attached to the base, and this experiment was set up not only to determine if the correct amount of heat was reaching the animal, but if a change in the direction of flow affected the temperature in each lane.

To determine if the base was reaching the correct temperature, temperature readings were taken at the top of the base from five equally spaced positions located in the center of their respective lanes. These positions were assigned numbers, beginning at the location nearest the nose cone, which remained constant throughout the trials. A Fluke 62 Mini infrared thermometer (Fluke, Inc.) was used to measure the temperature at each position. The three tests were performed over two days, with the first test performed on Day 1 and the latter tests both performed on Day 2.

Each test began by heating the water bath to 40ºC before connecting it to the heated plate. The temperature of the water bath was measured using an immersible glass laboratory thermometer. The IR thermometer would then be calibrated by measuring the water bath and confirming the reading against the glass thermometer. The water bath would then be connected to the TRIO system using a total of 8 m of 4 mm ID silicone tubing. Once it was confirmed that the water was flowing properly and the inlets were sealed, the initial measurements would be recorded for each position. Measurements were taken at 5 minute intervals until 30 minutes had passed, at which point the interval was increased to 10 minutes. Measurements stopped at 60 minutes, for a total of ten measurements per position.

After the measurements had been completed, the pump was stopped and the base disconnected from the water bath. The water bath remained at 40ºC, but the base was allowed to return to room temperature (about 20ºC, as determined by the IR thermometer). The inlet and outlet were reversed by switching the tube placement, and the experiment restarted. This created two data sets of the water flowing from position 1 to position 5, and one data set of the water flowing in the reverse direction. After running the test three times, it became obvious that the readings were consistent independent of flow direction. The average of the three tests was calculated for each time point at each position, followed by the mean temperature over time and the associated square error of the mean (SEM). The mean temperatures at each position and the associated SEM are shown in **Table 3-1**. The temperature in the base took some time to stabilize, so only the measurements from 20 minutes onward are used to determine the mean in each position.

The measurements showed that the portion of the plate near the nose cone remained consistent at 35ºC once the base had reached a stable temperature. However, the temperature began to drop in Position 4, and drastically decreased in Position 5. The individual tests provided in the appendix show that this temperature drop consistently occurs only in Positions 4 and 5 regardless of flow direction, so it is unlikely due to heat loss as the water flows through the device. Instead, the cause was determined to be the silicone coating used to seal the base. The coating had been applied unevenly and was noticeably thicker at the rear of the base. The silicone likely acted as an insulator, preventing the water from warming the surface. Fortunately, the mouse's body (exclusive of the tail) only covered Positions 1-3, where the temperature was near normal body temperature. As such, the device was determined to meet the heating demands of

imaging sessions.

Table 3-1: Mean Temperature of Recorded Water Channels

Position	Mean Temp over 40 minutes (Celsius)	Mean SEM over 40 minutes
1	35.11	0.55
2	35.17	0.59
3	35.22	0.60
4	32.56	0.78
5	24.11	0.22

3.7 Conclusion

In summary, this project not only required the development of a GRIN lens implant, but also an interface that allowed the implanted subject to be properly aligned with the microscope system. The interface design also had to accommodate life support and anesthesia for the subject. Additionally, histological skills and protocols had to be learned in order to verify that implants were reaching the region of interest. These goals were all met, either through novel design or adaptation of similar systems.

CHAPTER 4

SURGERY METHODS

4.1 Animal Description and Care

The developed implants were tested on multiple strains of transgenic lab mice. Initial designs were developed in white lab mice transgenic for enhanced green fluorescent protein (eGFP) associated with double cortin (dcx). Double cortin is a marker for partially differentiated neural precursors. If placed correctly, the lens would capture the fluorescently labelled cells as they travelled along the rostral migratory stream from the subventricular zone to the olfactory bulb. The dcx-GFP mice were bred in house, and the original breeding pair was supplied by the Mutant Mouse Regional Resource Center (Columbia, MO).

The ability to image astrocytes was tested in white mice expressing eGFP under the promoter for glial fibrillary acidic protein (GFAP), a marker for astrocytes in the brain. Experiments targeting white matter tracts were performed on black mice that express yellow fluorescent protein in a subset of pyramidal neurons under the Thy1 promoter. Thy1 is an immunoglobulin superfamily member that can be modified to be expressed solely in projection neurons, making it an appropriate marker to study axons. Both strains were also bred in house, and the original breeding pairs were provided by Jackson Labs (Bar Harbor, ME).

All mice were housed in the animal housing facilities of the Biomedical Engineering Center, room 137. Male and female breeding pairs were kept in separate cages until a new litter was needed, at which point they were caged together until pregnancy was apparent, as judged by the researchers in conjunction with the animal facilities staff. Offspring litter mates were separated by sex and kept at a maximum of four to a cage. Litters remained with the mother for three weeks, after which the pups were weaned. At four weeks the sex of each pup was double-checked, and then a tissue sample was removed from the ear in one of four patterns. The resulting notch pattern was used to distinguish animals, as follows: animal one would receive a single notch in the right ear, animal two a single notch in the left ear, animal three a notch in both ears, and animal four two notches in the right ear. The samples were stored and shipped to a third party for genetic testing. The genotyping was performed by Real Time Labs (Carrollton, TX), indicating if the mouse was positive or negative for the desired transgene. Multiple tool sets were used to avoid mixing genetic material, as well as thorough washing and sterilization of tool sets when necessary. Mice were cared for by the animal facility staff. Unexpected problems, such as infections, congenital malformations, or behavioral changes, were brought to the attention of the facility director, who determined the appropriate course of action.

4.2 Surgical Procedure for GRIN Lens Implant

All surgical procedures used in this research were developed based on instruction from Dr. Teresa Murray, the Lifshitz lab (Barrow Neurological Institute, Phoenix, AZ) (with special thanks to Dan Griffith, Megan Evilsizor, and Katharine Eakin), and procedures taken from the literature[30, 46]. These surgical procedures were

incorporated into a protocol that was approved by the Louisiana Tech University Institutional Care and Use Committee.

Animals used in surgery were anesthetized with either an intraperitoneal injection of ketamine/xylazine cocktail, or through intranasal administration of vaporized isoflurane (SomnoSuite, Kent Scientific). During surgery, the subject's vitals (most notably heart rate and body temperature, but also SpO2 when a consistent measurement was obtained) were monitored and body temperature was maintained using an integrated, commercially available system (PhysioSuite, Kent Scientific). A pulse oximeter sized for mice was placed over one rear paw, while a temperature sensor was placed between the subject's body and the heating pad. The other rear paw was left bare, allowing the surgeon to ensure a proper plane of anesthesia was maintained with routine noxious stimuli in the form of a toe pinch. Noxious stimuli were applied every fifteen minutes during surgery with a pair of forceps, followed by proper resterilization of the surgeon's gloves with 95% isopropyl alcohol before resuming surgery. Opthalmic gel was applied to the subject's eyes just after anesthesia was induced to prevent drying. All tools used during surgery were stored in sealed packs and sterilized with an autoclave prior to the procedure.

Prior to any incision, the subject's scalp was cleared of fur and sterilized with alternating treatments of povidone-iodine (Equate) and 95% isopropyl alcohol (Equate). Scissors were used to clear the fur rather than an electric razor to prevent incidentally inciting a larger injury response than necessary. After the fur was removed, the animal was placed in a Benchmark stereotaxic frame (Leica Biosystems) with a mouse and neonatal rat adaptor (Stoelting). Once the scalp was sterilized, a scalpel was used to

make a rostral-caudal incision through the skin. In very early surgeries, the procedure would proceed without further damage to the scalp. However, it was found that the skin would grow back and interfere with the implant, possibly completely covering lower profile procedures such as cranial windows. To prevent such interference, surgeries were quickly modified to remove all skin in the immediate area around the incision with scissors.

Once the skin was removed, the scalpel blade was used to scrape the periosteum from the skull. This removal helped to reveal landmarks and created a dry surface, which could be more easily marked, was easier to drill through, and adhered better to the the glue. The landmarks used for these surgeries were bregma and lambda, two distinctive intersections of sutures on the top of the skull. With the aid of a mouse brain atlas[12], the eventual position of the GRIN lens was mapped out in relation to bregma prior to surgery. Once revealed and cleared, bregma was marked with a black, fine tip marker. This central mark provided an unambiguous center, preventing slight variations in later measurements which would have had major ramifications.

After bregma was located and marked, a sterilized plastic ruler was used to locate the craniectomy location. The GRIN lens was implanted through a 2 mm diameter craniectomy that was drilled through the skull with a foot operated drill. The exact location depended on the target cell type, but the most common surgery performed in this research targeted Thy1-yfp tagged cells in the Corpus Callosum. To image these cells, the craniectomy was located 1 mm rostral and 2.5 mm lateral to bregma, and inserted at a 15º medial-lateral angle. The targeted region is shown in **Figure 4-1**.

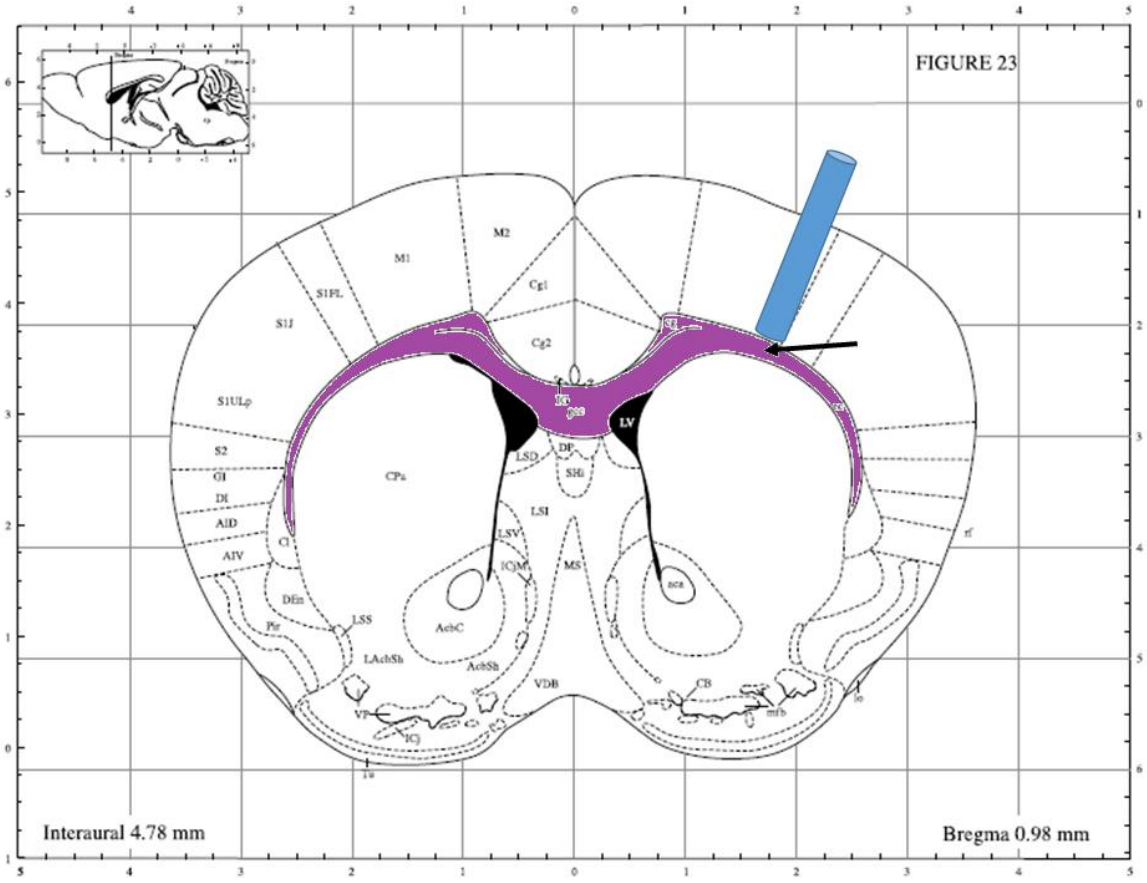

Figure 4-1: A representation of the target region for GRIN lens surgeries in Thy1-YFP labelled mice. The blue cylinder represents the GRIN lens. The portion outside of the brain would extend through the skull and connect to the cover glass of the implant. The callout indicates the approximate focal point of the lens, 125 µm below the distal end. The purple region shows the corpus callosum and external capsule, a region of highly myelinated axons labelled by the Thy1-YFP protein. Major demarcations are in millimeters. Adapted from Paxinos and Franklin's Mouse Brain Atlas[12].

For larger craniectomies, the drill bit was typically guided around the outer edges of the desired area to be removed. This allows the surgeon to maintain a raised area in the center that could gripped with forceps and removed. Removing the bone in this manner limits damage to the underlying dura, and typically prevents broken fragments from plunging into the brain. Unfortunately, the small size of the craniectomy used in this research made it difficult to keep the drill bit out of the center. Instead, a careful touch was used, and the consistency of the bone was regularly probed using a

hypodermic needle. The hypodermic needle allowed the surgeon to gauge the thickness of the remaining bone without the consequence of accidentally drilling into the brain. This method would be problematic in experiments that required preservation of the dura, as the needle could easily penetrate the soft membrane, but was possible here because the dura was removed to allow the lens to be implanted unobstructed.

Eventually, the bone would be thinned enough that the hypodermic needle would begin to pierce it. At this point, drilling ceased and the remaining bone was separated with the needle, then removed with forceps. A cruciate cut was made in the dura, allowing the surgeon to move it aside so it would not be forced into the brain by the implant. Surgical sponges were placed over the area to reduce bleeding while the implant was loaded into the cannula holder.

Implants were sterilized with UV radiation prior to surgery, then stored in a sealed container. An implant was removed from the container and loaded into the cannula holder immediately before surgery to ensure any damage incurred by the process was addressed before putting an animal through undue stress. Once loaded, the cannula holder was set aside while surgery proceeded. After the craniectomy was completed, the cannula holder and lens were again sterilized with 95% isopropyl alcohol and replaced on the stereotaxic frame. The lens was positioned over the center of the previously left mark, then moved stereotaxically to the implant site. Once the surgeon was certain that there would be no obstructions to lens insertion, the lens was lowered into place at a rate of roughly 250 μm per minute until the glass cover slip contacted the skull. If the implant was not flush against the skull due to the surface's curvature, surgical sponges were used to fill any gaps. A small amount of cyanoacrylate gel was applied at the edges

of the implant to prevent displacement and seal any openings. Pressure was applied evenly across the top of the implant with the scalpel blade to prevent movement while the cyanoacrylate dried.

The skin around the surgical site was sealed to the skull with cyanoacrylate. This created a barrier, during the remainder of surgery and the healing process, with the goal to prevent extracellular fluid from disrupting the glue around the implant as it set. Dental cement was then mixed and placed over the exposed skull. The dental cement was durable polymer comprised of a powder and liquid activator (Aplicap™, 3M). Once mixed, the polymer would form a viscous liquid that could be applied to the surface of the skull as needed. The polymer was applied over the entirety of the exposed skull to prevent exposure to infectious or otherwise harmful agents. The dental cement was carefully guided with a hypodermic needle, ensuring that it remained on the outside of the metal washer encircling the imaging window. The polymer around the implant was allowed to rise no more than half way up the wall of the implant, leaving space for interaction with the imaging interface.

After the dental cement was applied to the surgeon's satisfaction, the subject remained undisturbed for twenty minutes to allow the polymer to partially set. During this time, anesthesia and heat remained active, but the ear bars used to brace the mouse's head in the stereotaxic frame were released to prevent unnecessary pressure on the vagus nerve and relieve the subject's breathing. A microwavable heating pad was warmed up and placed under a clean cage in preparation for the subject's eventual relocation. Animals were caged individually after surgery to limit implant loss. The cage bedding was shifted to one side, exposing the bare cage floor. When the animal was completely

released from the stereotaxic frame and caged, it was placed in the cleared portion of the cage. The bare surface prevented the bedding from interfering with the subject's breathing or becoming stuck in the dental cement.

The surgeon remained with the subject until it regained consciousness. At this point, the surgeon placed a food pellet on the cage floor, in easy reach of the recovering animal, and replace the cage top. A dose of analgesic (Children's Advil, Pfizer), calculated by weight, was mixed with the animal's water supply. When it was clear the animal was capable of moving about the cage voluntarily, the cage was returned to an open spot on the appropriate rack in animal housing.

4.3 Alternative Procedure for Traumatic Brain Injury Hub

For studies involving TBI, a diffuse brain injury was created using a fluid percussion device (Custom Design and Fabrication, Virginia Commonwealth University). This device required a surgically implanted hub that connected to a Luer lock on the end of a small, flexible tube. This tube was attached to the fluid chamber of the fluid percussion device. When the opposite side was struck with a weight on the end of a pendulum, a pressure wave propagated through the fluid, eventually inflicting a diffuse brain injury on the subject.

Preparing a mouse for TBI required a slightly different surgical procedure and preparation previously described in the literature. The injury hub was created by cutting off the needle from a 20 gauge hypodermic needle with a razor blade, then beveling the edge with a hand operated crayon sharpener. Creating injury hubs was a time consuming process, so most of the hubs required for upcoming surgeries were made in a single

sitting, then stored in a sealed container until needed. During surgical preparation, hubs were sterilized in a bath of 95% isopropyl alcohol.

In addition to the hubs, a small guide was required to aid removing the skull during the craniectomy. This guide was made by cutting a roughly 1 mm thick piece of 1 mm diameter plastic line trimmer filament, normally used in lawn care equipment. The guide was secured to the skull using cyanoacrylate during surgery, and used to remove the freed section of bone.

Once preparations were completed, surgery proceeded as described above up to the clearing of the periosteum. Instead of proceeding to use a foot operated drill to create a 1 mm craniectomy, a hand turned trephine was used to drill a 3 mm craniectomy on the medial suture at the midpoint between bregma and lambda. The center was measured and marked, then the guide was attached. The small plastic guide was substituted for the pin normally used to guide a trephine to alleviate weight on the skull. The extra weight of the pin could cause the skull to give way without warning, resulting in massive destruction of the brain, and requiring the animal to be euthanized.

The goal of the surgery was to complete the craniectomy without disrupting the dura. Any disruption of the dura could result in herniation of the brain through the craniectomy after TBI was induced. When the surgeon judged that the skull had been thinned enough by the trephine, the tool was put aside and a pair of forceps was used to grip the plastic guide. By applying light lateral stress, never rotational, the surgeon could free the bone from the surrounding skull without disrupting the dura.

Once the craniectomy was successfully completed, the surgeon would inspect the dura to ensure it had not been damaged. After the assessment, a small bead of sterile

saline solution was placed over the opening in the skull to prevent the brain from drying and the injury hub was prepared. The hub was carefully placed over the craniectomy and secured with a small amount of cyanoacrylate. Additional sterile saline was injected into the injury hub once the glue had dried to determine if it was leaking. If the injury hub was properly sealed, the top was covered with a piece of tape and the skull covered in dental cement, as previously described.

Mice fitted with injury hubs were placed in special cages without low hanging bars to prevent premature detachment. Recovery was monitored as previously described. The method of TBI induction will be described further in Chapter 6.

4.4 Replication of Surgical Techniques

A pressing issue across biological sciences is the ability to replicate novel results. Although miniature endoscopic lenses such as the GRIN lens have gained widespread popularity over the past decade, the techniques used in this research, although based on articles available in the literature and training provided by more experienced researchers, were developed independently. In the interest of aiding similar research projects and of good scientific practice, the manufacturing, surgical, and imaging techniques discussed here were taught to both dedicated lab members and visiting personnel. Specifically, Dr. Chelsea Pernici, Dr. Charla Poole, Vlad Voziyanov, and Tim Doughty were all trained to use the developed system and implant techniques. All of them have successfully implanted the lenses into animals, and have obtained images of specific cell types in the brain. Examples of these images will be shown in Chapter 5. In some cases, those instructed in these procedures further developed the implant to suit their own research.

While those developments have been left to the other researchers to describe, it is still satisfying to watch the system's rapid evolution and continued effectiveness.

CHAPTER 5

MULTIPHOTON IMAGING THROUGH THE IMPLANTED LENS

5.1 Imaging Setup

Imaging experiments were conducted in the Biomedical Engineering Center, Room 132, using equipment acquired for this purpose. A Zeiss microscope was outfitted by 3i (Intelligent Imaging Innovations) to function with their proprietary Slidebook software and a Coherent Chameleon titanium sapphire, multiphoton laser (80 MHz, Coherent). The microscope was enclosed in a large shield to prevent incidental light from disrupting the sensitive photo multiplier tubes (PMTs). Prior to imaging, samples could be brought into focus through the eyepieces, with the aid of either brightfield or fluorescent lights. Unfortunately, no camera was attached to obtain brightfield or fluorescent photos. The stage controls were located outside of the shield, and accessible to the researcher during imaging. The microscope, shield, and laser were installed on an air table and optical breadboard with ¼”-20 threaded holes. Other functions were controlled using the Slidebook software, a proprietary program for the Vivo™ 2-Photon Microscopy Workstation (3i, Inc.).

The functions controlled by the Slidebook program included, but were not limited to, the wavelength of the laser, the attenuation of laser power through the Pockels cell (Conoptics, Danbury, CT, USA), the sensitivity of the PMTs, the position of the filter cube, the digital zoom of the image, the resolution of the image, the number of planes in

three dimensional images, the number of times each plane was captured and averaged, and the number of time points in an imaging session. Most images taken in this research were single time point images including multiple planes in the z dimension. The x and y dimensions were typically left at their max value. Laser wavelength and power as well as PMT sensitivity depended on the sample imaged. Images were taken at 1024x1024 pixel resolution. Although the filter cube contained filters for a wide array of wavelengths, the filter relevant to this research was a fluorescent bandpass filter set for red (612/69 nm) and green (525/40 nm) emission (Semrock, Inc.), as it allowed the passage of light emitted by enhanced green fluorescent protein (eGFP), yellow fluorescent protein (yfp), and Texas red dextran (TRD).

The laser emitter was secured to the table beside the microscope enclosure. The beam path ran through a shielded tube before entering the back of the enclosure, immediately encountering the Pockels cell. The beam was redirected into an *m*BEAM™ (3i, Inc.) software controlled beam expander. After passing through the beam expander, the laser entered the back aperture of the microscope objective. A plastic shield prevented direct exposure to the researcher as the beam passed through the back of the enclosure.

The microscope stage was trapezoidal and large enough to easily accommodate an anesthetized mouse. The stage was also evenly spaced with ¼”-20 threaded holes, allowing for simple integration of the H-shaped interface described in Chapter 3. The stage could be moved in x and y during imaging, but adjustments in height were more involved and only undertaken under extreme circumstances. Instead, the nose piece of the microscope was moved to adjust the distance of the objective from the subject. No

turret or slide was attached to the microscope, forcing the researcher to remove the objective and replace it with another if desired.

When the H-shaped interface was used, the long bars would be propped up on 1 mm thick washers to a height that could accommodate the imaging subject. A screw was then passed through the bar and the stack of washer before entering the threaded hole in the stage. The screw was turned until hand tight, holding the bar firmly against the washer stack and preventing the washers from sliding out of position. This method allowed the height of the frame to be changed in regular increments as necessitated by the subject's size. The heated plate of a PhysioTemp heating unit was placed under the interface and used to maintain the subject's body temperature during imaging.

The TRIO system required more time to set up. The base was set on the stage, with the nose cone facing the rear of the enclosure. Paper towels were placed near the water inlets to limit the spread of any water released by a faulty connection. A circular opening in the side of the enclosure allowed power and communication cables to reach the various systems inside. The tubes allowing for delivery of anesthetic and warm water were also run through this opening, then connected to the appropriate ports on the TRIO system. The anesthesia tubes were connected to a Somnosuite identical to the one described in Chapter 4. The Somnosuite was located outside of the enclosure, which allowed the researcher to adjust the rate of delivery or refill the reservoir without opening the enclosure. In early iterations, a warm water bath was prepared using a lab hot plate and 1 L beaker filled to submerge a small aquarium pump. The inflow tube leading to the TRIO system was connected to the pump, while the outflow tube returned water to the bath. A glass thermometer was placed in the bath to monitor the water's temperature.

An integrated pump/heater was eventually purchased to connect directly to the TRIO system, simplifying setup by replacing the water bath and aquarium pump.

5.2 Animal Preparation

Animals were taken from housing and allowed to acclimate to the imaging room for at least thirty minutes while the imaging area was set up. The interfaces used in this research were designed to handle animals differently, so each will be described individually. However, for both pieces of equipment, imaging of an individual animal was limited to no more than two hours.

The H-shaped interface was designed for work with an animal anesthetized with the ketamine/xylazine cocktail described in Chapter 4. Once setup was complete, the animal was injected with 0.1 mL of sedative per 10 g body mass and remained caged until anesthetized. A toe pinch was used to decide if a proper level of anesthesia had been obtained. The animal was briefly placed under a stereomicroscope, and the implant was inspected for debris. A broken cotton swab handle was used to clear any debris from the imaging surface of the implant, under the assumption that the wood would be less likely to scratch the glass than a metal implement. The broken handle was dipped in isopropyl alcohol to aid in clearing the imaging area. Once judged clear, the mouse was brought to the main microscope stage and placed on the heated plate of the PhysioTemp. Opthalmic gel was applied to the subject's eyes to prevent drying. A small cushion cut from packaging foam was used to prop the subject's head up, helping to force the implant into the socket of the interface's crosspiece. The crosspiece was then placed into position over the implant, and taped down against the frame. The animal was observed for

distressed breathing, and repositioned if any difficulty was suspected. The objective was then screwed into the nose piece, and imaging began.

The TRIO system was designed to eliminate the need for the K/X cocktail, relying instead on gaseous delivery of isoflurane. To begin, the subject was removed from its cage and placed in an induction chamber, where it was anesthetized using 3% isoflurane at 500mL/minute delivery rate. The TRIO system base, disconnected from the water lines, was kept on hand with the stereoscope. The anesthetized subject was transferred to the TRIO system base along with the tubes running isoflurane. The percent isoflurane was lowered to 1.5%, and the implant was cleared of debris in the same manner as described with the alternative interface. The base was disconnected from the short gas lines used with the induction chamber and transferred to the microscope stage. The long hoses, already running into the enclosure, were connected to the Somnosuite and the TRIO base. The water hoses were also connected to the TRIO base, and the pump activated. The subject's anesthesia level was checked with a noxious stimulus and, if adequate, the researcher placed the subject in the head restraint. As before, a small cushion cut from packing foam was used to lift the subject's head. The cutout headplate described in Chapter 3 was placed over the implant, then fit into the slots of the arm bars. As with the previous setup, the subject's breathing was monitored and the animal repositioned if distress was noted. Once the researcher was satisfied with the subject's state, the objective was screwed into the nose piece and imaging would begin.

Figure 5-1 shows mice restrained in each system. Images A and B show a sedated mouse in the H-shaped restraint on the microscope stage. Image C shows an anesthetized mouse in the TRIO system.

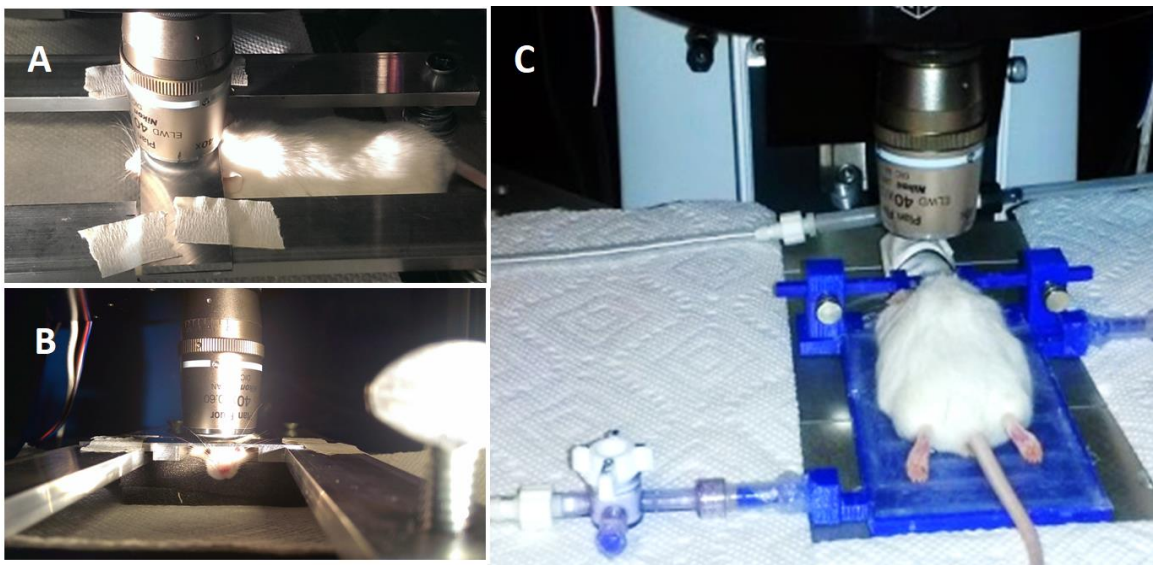

Figure 5-1: Anesthetized mice positioned under the microscope objective. Images A and B show the H-frame interface, which required the mouse to be anesthetized with a subcutaneous injection of K/X cocktail. Image C shows the mouse in the TRIO system, with attached tubes for heated water and vaporized anesthetic delivery.

The first step towards imaging through the GRIN lens was to center the lens under the objective. This was a difficult task to perform solely through the eyepieces due to the inability to easily and accurately switch from a low magnification lens to the 40x objective. This problem was resolved by using the fluorescent capabilities of the microscope. When the fluorescent lamp was enabled and the GFP filter was used, a visible beam of light shone through the microscope objective. The circle of light created by this beam was used to align the objective over the hole in the restraint system. Afterwards, the researcher could view the top of the cover glass through the eyepieces. The GRIN lens usually appeared as a green circle through the filter, while the cover glass remained dark. Whether this was an interaction of the lens with the fluorescent lamp or the optical adhesive used to secure the lens to the cover glass is unknown, but researchers were able to take advantage of this circumstance to locate the lens under the high power

objective with relative ease. By happenstance, it was discovered that this method was not feasible if the headplate was made of ABS plastic. Early iterations of the cutout headplate attempted to use a 3D printed model to reduce thickness, however it was discovered that the entire cover glass appeared green through the eyepieces when the plastic headplate was used, obscuring the location of the lens. This effect is likely caused by the high quantity of phenyl groups in plastic creating autofluorescence, which washed out anything below it. The autofluorescence was alleviated by switching to a metal cutout headplate.

When the lens was aligned with the fluorescent light, it was possible for the researcher to focus on deep brain structures through the lens. However, the labelled cells and processes were rarely visible using this method. Vasculature often was visible, though, appearing dark against a diffusely fluorescent background. When fortunate enough to have clearly visible vasculature, researchers could use these structures as landmarks during imaging and as an indicator that the objective was near the appropriate z position to focus through the lens. If no structures were visible, researchers centered the objective over the lens, and made the final preparations for using laser illumination.

As mentioned above, vasculature was a useful landmark for researchers using the GRIN lenses, especially for studies using GFAP or YFP labeled animals. In these cases, the labeled cells are expected to undergo conformational changes, making it difficult for the researcher to be certain the lens remained stable for the duration of a longitudinal study. In contrast, the vasculature was largely stable, providing the researcher a consistent reference point between imaging sessions. For these studies, an additional step was added to the animal preparation, before the animal was transferred into the

microscope enclosure. After the animal was anesthetized, it was injected with 0.1 mL of the fluorescent dye Texas Red Dextran (TRD) in a concentration of 10 mg/mL (70,000 Da, ThermoFisher). The animal was placed on its back after reaching an acceptable level of anesthesia, and the dye was slowly injected into the tail vein. The tail vein is one of the largest vessels in the animal that is also clearly visible and near the surface. Instructions in proper tail vein injection were given by Dr. Teresa Murray and Dr. Charla Poole. With the dye circulating, any vasculature in the region of interest would also be visible. The difference in dye color allowed the system to distinguish between the fluorescence given off by the TRD and the fluorescently labeled cells.

5.3 Imaging

The microscope housing was closed after the animal had been successfully positioned for imaging. The room lights were turned off to protect the PMTs, and the imaging was controlled from the computer console. In Slidebook, the researcher would set the laser to an appropriate wavelength, increase the sensitivity of the PMTs and the amount of laser power allowed through the Pockels cell, and change to the appropriate filter. The researcher could then open the laser shutter, allowing the beam to travel to the subject and excite the fluorophores in the labeled cells or dye. A live image of the illuminated region could be displayed on screen, and, by rapidly scanning at a lower resolution, the researcher could pinpoint a region of interest, record the relative location in x, y, and z, and proceed to capture the desired image at a higher resolution. The filter cube allowed researchers to acquire images in both the red and green channel simultaneously, reducing the risk of harming the subject or bleaching the fluorophores.

For experiments involving YFP and GFAP, the excitation wavelength was set to 890 nm. This wavelength not only excited the fluorescent proteins present in the animals, but also the TRD dye. The PMTs were initially set to 70% sensitivity and the amount of laser power allowed through the Pockels cell was initially increased to 35% of the 1 W total. For comparison, thin samples such as preserved tissue on slides required a laser power of 5-10%. Reasons for the necessary difference in applied laser power include, but are not limited to, interference from the doping ions in the GRIN lens that shape the light as it passes through, reflection, and light scattering as the laser passes through 150 μm of tissue between the end of the lens and the focal point.

The resolution of the image could be set, ranging from 128x128 to 1024x1024 pixels. The time it took the laser to scan and present an image was directly affected by the resolution of the image, so obtaining images at maximum resolution was usually reserved for the final capture, not intermittent scanning. When determining a new region of interest or locating a previously used landmark, a resolution of 512x512 pixels was typically used. When the system was set to a continuously scanning mode, this resolution provided images quickly enough that a researcher could steadily adjust the z position of the objective lens with enough detail to determine major features. Once the plane of the region of interest had been located in z, the researcher could begin capturing a stack of images around it.

One of the major advantages of this system is the ability to capture multiple planes in the z dimension through the GRIN lens. A series of x-y planes captured along a single z axis is referred to as an image stack. As described earlier, multiphoton microscopy only provides enough energy to excite fluorescent particles when the photons

strike almost simultaneously. This limits interference from fluorescent sources outside the plane of focus, and allows the researcher to capture details despite a close proximity in z. The microscope system allows the researcher to set a desired range of motion in z, the step size between planes, or the number of planes to be captured within the range. Once two have been set, the third is automatically calculated. The researcher can then choose to use the current z location as a starting point or a central point for the image stack and force the objective to return to the starting z position or remain at the end point after the stack has been captured.

Additionally, the researcher can use a digital zoom to select a specific region of interest to scan within the microscope's maximum field of view. This region can be selected freehand from a menu on the console, then refined to an exact area, providing the researcher and future analysts with a known pixel to micron (or preferred unit of distance) ratio. Selecting a smaller region of interest can aid later image analysis by providing increased image resolution, up to a theoretical limit. The theoretical limit of image resolution is determined by a ratio of the excitation wavelength (λ) used to the numerical aperture of the objective lens (NA), as shown in **Eq. 5-1**[3]. In the case of these experiments, with an excitation wavelength of 890 nm and numerical aperture of 0.6, the theoretical resolution limit was roughly 905 nm.

$$r_{xy=}\frac{0.61\lambda}{NA} \qquad \textbf{Eq. 5-1}$$

After the image stack parameters have been set, the process is mostly automated. The researcher selects the channels they wish to capture, and start the process of scanning the region of interest. The program provides a still of each plane as it is captured, allowing the researcher to detect saturation in the image, large motion artifacts, PMT

overload, or any other problems that would require restarting the process. Once an image stack is captured, the laser shutter is closed, the PMTs are deactivated, and the subject's vitals are checked as well as the pad temperature and anesthesia levels. At this point, the researcher may choose to end the imaging session or continue imaging at a new location. Most sessions performed using this system took multiple image stacks over the same region in z, but at different x-y locations. Multiple image stacks allowed the researcher to later create a mosaic of the GRIN lens's entire field of view, which exceeded the microscope system's maximum field of view.

After imaging was completed, the subject was removed from all restraints and replaced into their cage. The researcher would monitor the subject's breathing until the effects of anesthesia had worn off and the animal was moving freely. The amount of time needed to monitor the animal varied by anesthetic. Isoflurane is eliminated quickly, and its effects typically wear off in 3-5 minutes. The ketamine/xylazine cocktail had much longer lasting effects, and it could be 20-30 minutes before the mouse regained locomotive function. Once the subject was moving freely in its enclosure, the cage was returned to the appropriate room in animal housing.

5.4 Results

Images were saved as a proprietary file type in the Slidebook software, and could be viewed and manipulated in the program. While some of the manipulation tools available were useful, such as filter application and three dimensional projection, it was far easier to export the raw data and reconstruct it in the commonly used program, ImageJ[47]. Image files were exported as gray-scale, single channel images in the .tiff format. Each image file was accompanied by an OME file containing pertinent metadata,

such as the capture and export times, the file dimensions, the number of channels and their assigned PMT, as well as the microns per pixel.

Using ImageJ, raw data files or filtered data files were combined to create images demonstrating the anatomical structure beneath the GRIN lens. The channels were pseudocolored using a green or red look up table (LUT) as designated by the OME file. This was done using the "merge channels" function in ImageJ, which can be found under the Image->Color menu. This function allowed the user to assign an open image file to a specific color channel, creating a single image file with pseudocolored versions of the data found in the original files. The user could then adjust individual properties of each channel, such as brightness or contrast, while maintaining the integrity of the original image file. This was especially useful if, during imaging, one color fluoresced with much higher intensity than the other.

Once the user was satisfied with the appearance of the image stack, the file could be prepared for publication. While some online journals allow the entire stack to be downloaded as supplementary material, in general the file should be reduced to a single, more easily reproducible two dimensional image. A single image plane could be chosen to represent the stack, but the architecture of the brain rarely aligns with the imaging plane of the lens. Important features that are continuous in x and y may appear disrupted in a single plane because they twist and turn through the z dimension. Instead of using a single plane, multiple planes were typically combined into a z projection. This function found in ImageJ created a new image file using the average intensity value of each pixel from selected planes in the original stack. The two dimensional image created using this

method retained data from each plane, allowing the researcher to create a better representation of the architecture captured during imaging, as long as the z step was smaller than the observed feature.

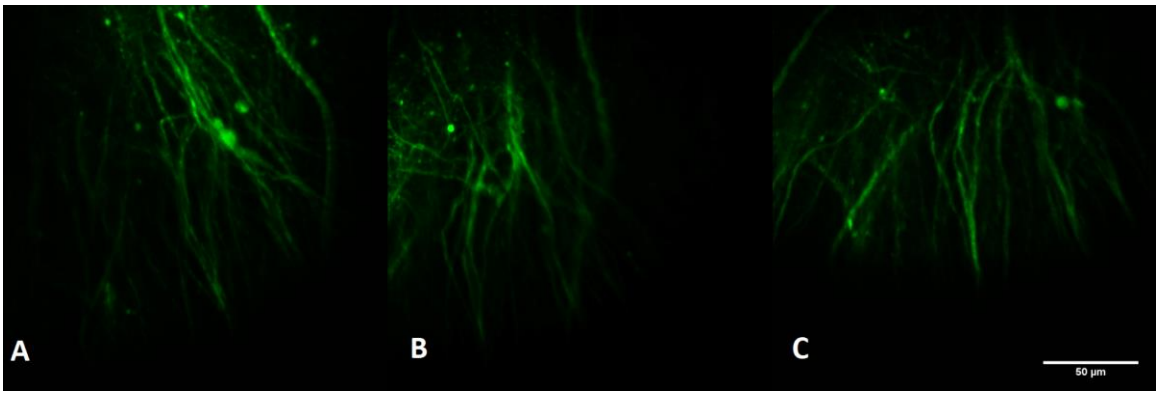

Figure 5-2: A series of z projections of images acquired through similar portions of the GRIN lens of YFP-expressing cells. A bifurcating bundle of axons appears as a regular feature. Image A was acquired January 29th, 2016 using the H-frame interface. Image B was acquired March 4th, 2016. Image C was acquired March 31st, 2016. Both images B and C were acquired using the TRIO system interface. 50 µm scale bar.

An example of a series of z projections can be found in **Figure 5-2**. The series of images is comprised of z projections taken from stacks captured over a period of 60 days from a single subject. Each image is the average of five planes covering approximately the same location, though the exact step size between planes (and thus, the total z dimension) varies between the first image and the following three. Five was chosen as the appropriate number of planes to avoid blurring the image. A drawback of using z projections is that significant changes can occur over the totality of the image stack, resulting in a loss of detail when planes encompassing too much of the stack are averaged. The image stacks captured in this study would extend 50-100 µm in the z dimension. Over such a large area, many features appear and disappear, making it impossible to create a z projection of the entire stack. With images taken at 1-2 µm steps,

the z dimension would only cover 5-10 μm, a limited enough region to capture some three dimensional aspects of the sample without reducing the image quality.

When it is necessary to display a larger region of the image stack, there are multiple options. The first option is to create a series of z projections descending through the image stack, then to display them sequentially. This option presents the entire stack in a publishable format, while providing some three dimensional detail to the reader. Alternatively, when a digital format is available, the stack can be presented as an animated gif, showing each plane sequentially.

As previously mentioned, a single image stack cannot always encompass the entirety of the GRIN lens' field of view. In this research, this problem was alleviated by capturing four slightly overlapping image stacks. Once processed in ImageJ, the resulting z projections could be digitally combined to create a larger mosaic. The ImageJ plugin, MosaicJ, was used to perform this function. It was created and distributed by Philippe Thévenaz, Biomedical Imaging Group, Swiss Federal Institute of Technology Lausanne[48]. Though it provides a grid to aid alignment, the mosaics created in the plugin are largely qualitative and dependent on the researcher's familiarity with the captured images. However, when aligned with care, the resulting mosaic can present a very detailed image.

Figure 5-3 shows a mosaic created from four z projections, each created using eleven planes of an image stack. The animal was prepared with an injection of TRD dye, making the vasculature in the region visible as well as the YFP labelled axons. At the time of capture, the implant had been in place for three months. Images obtained from this implant remained of similar quality for another month before deteriorating. The

mosaic image shows no obvious differences where the image stacks overlapped, making the plugin a powerful tool for reconstructing captured data.

As previously mentioned, multiple researchers were able to successfully replicate these techniques and use the developed GRIN lens implant to record images. **Figure 5-4** shows the results obtained by Dr. Chelsea Pernici and Dr. Charla Poole, who used the implants in different strains of mice. Dr. Pernici, a fellow lab member at the time, used the implant to image astrocytes expressing glial fibrillary acid protein (GFAP) and eGFP surrounding blood vessels carrying TRD. Dr. Poole, a visiting researcher with surgical expertise related to inducing stroke, was able to capture a time series of neuronal precursors expressing double cortin (dcx) and eGFP.

5.5 Discussion

This chapter demonstrates the methods used to prepare both the imaging area and the animal subject for capturing images through the GRIN lens. Additionally, it shows the results of the described imaging practices, from both the perspective of a single time point as well as longitudinally. The data acquired and presented in this chapter have been used as a proof of concept for longitudinal imaging using the GRIN lens implant described in this research.

This chapter describes the different setup requirements for the H-shaped interface and the TRIO system, because both were used to capture data presented in **Figure 5-2**. The first panel was taken with the H-shaped interface, and shows a noticeable difference in the level of detail. Finer processes are slightly more distinct in images taken with the earlier interface. The improved image quality may be due to an increased level of restraint restricting motion artifacts induced by the animal's breathing, or an improved

alignment of the lens with the microscope objective. However, the small payoffs came at a large cost, as the H-shaped frame had many disadvantages compared to the TRIO system. Not only did it require an unincorporated heating element that took up additional room in the microscope enclosure, but, more importantly, it could not incorporate a gaseous anesthetic such as isoflurane without significant modification. Based on empirical experience, isoflurane is a much simpler anesthetic to manage, resulting in a safer environment for the animal. With an injected anesthetic like the ketamine/xylazine cocktail, adjustments were limited after the injection. An animal that resisted the effects or came out earlier than expected could be updated with an additional injection of anesthetic, but this would risk upsetting the alignment of the lens in the interface. An animal that was more sensitive to the initial dose would often experience distressed breathing, creating extreme motion artifacts with no recompense for the researcher. When isoflurane was used, the concentration of anesthetic delivered to the mouse was easily adjusted with the turn of a dial. The gaseous anesthetic cleared more quickly than its injected counterpart, meaning adjustments to the delivered concentration had almost immediate effects. The slight reduction in image quality was deemed an acceptable loss when the ease of setup and diminishment of stress on the animal were taken into account.

Also of note was the successful replication of the described techniques by researchers uninvolved in their development. Although the images shown were taken over a much shorter period of time, they still indicate that the low profile system can be reliably implanted by experienced surgeons and aligned beneath a microscope objective using the provided interface. This bodes well for the expanded incorporation of such devices in future research.

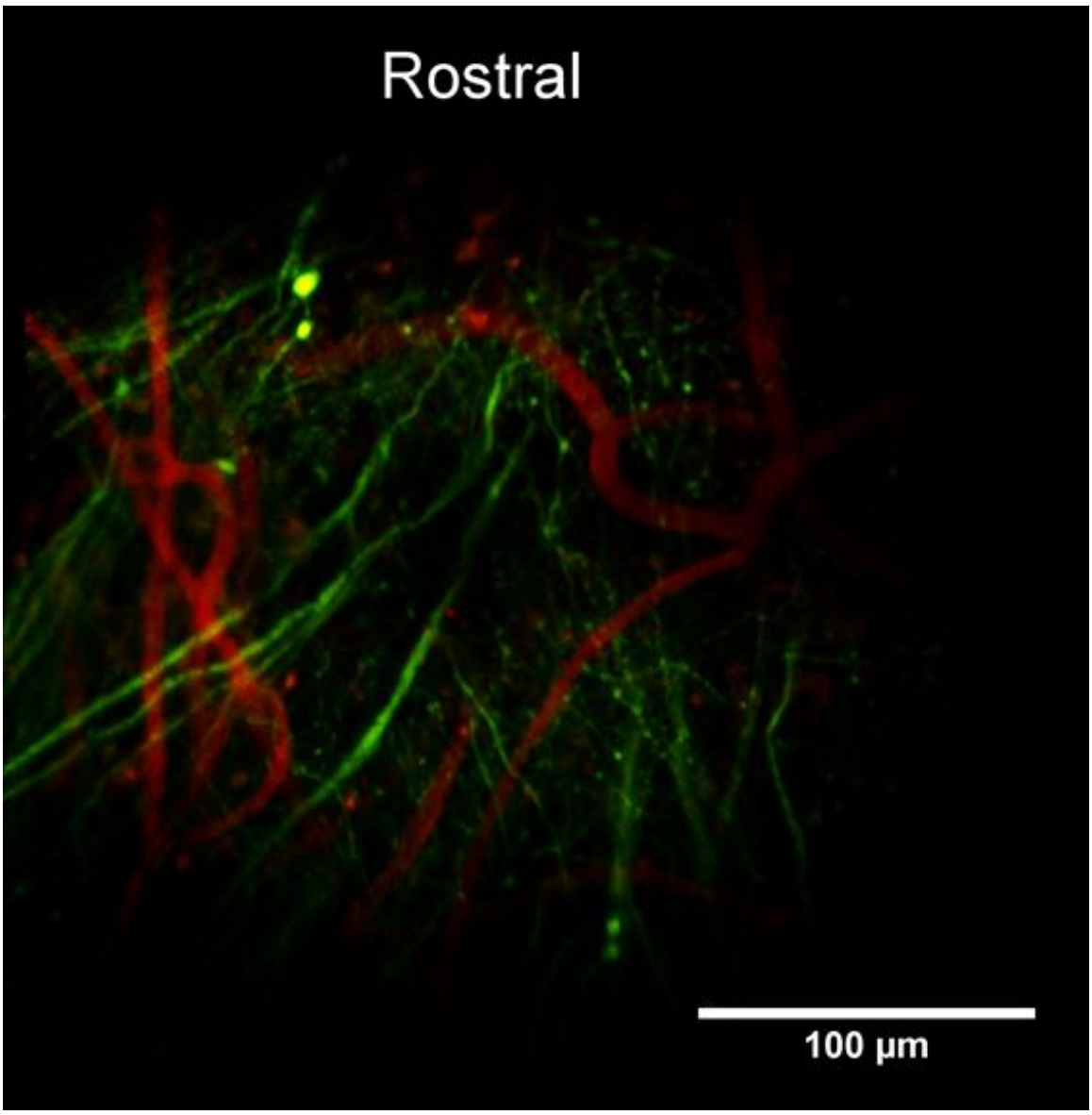

Figure 5-3: Mosaic prepared using images captured March 25, 2016. Four image stacks were acquired, with 200x200 µm dimensions in x and y, and a 2 µm step size in z. The image stacks were first reduced to z projections created using 11 planes. The individual z projections were aligned in ImageJ using the MosaicJ plugin, resulting in the final image. Texas Red Dextran (TRD) dye was injected into the tail vein and allowed to circulate to provide images of local vasculature through the red channel. The green channel acquired images of yellow fluorescent protein (YFP) expressing cells.

The low profile, longitudinal approach to GRIN lens imaging should open up new avenues of research. One of the most difficult parts in working with mice is the small size of the skull, which typically limits research to one type of observation. By

continuing to reduce the profile of the GRIN lens implant, more space is left open to incorporate other forms of signal collection. Alternative strategies could include implanted electrodes to record the electrical signals emitted in the region visible through the lens, or an injection port to inject dye into the lens's field of view, revealing fast dynamic events against traditionally labelled cells. It would also be possible to incorporate additional surgeries that induce an observable injury state over the life of the implant. This could allow study of the events such as the migration of microglia into the penumbra of a stroke or damage induced by traumatic brain injury in real time, as well as the possible effects of treatments for said injuries.

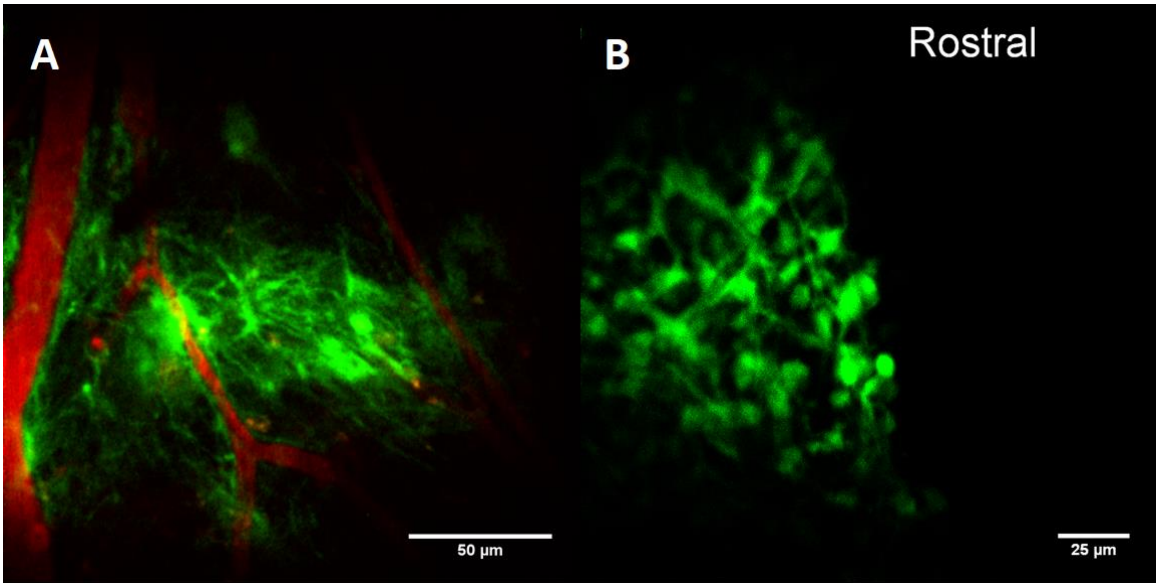

Figure 5-4: Images obtained by successful replication of the techniques described in this dissertation. Image A is a stack of five z planes containing astrocytes expressing eGFP-GFAP and blood vessels carrying TRD captured by Dr. Chelsea Pernici. Image B is a stack of seven z planes containing neuronal precursors near the wall of the lateral ventricle expressing eGFP-dcx captured by Dr. Charla Poole. Both researchers were instructed in the implantation and imaging procedures by Ben Kemp, but completed the surgery and imaging to capture these images independently.

CHAPTER 6

EFFECTS OF TRAUMATIC BRAIN INJURY INDUCED MEMORY DEFICITS ON BEHAVIORAL TESTING

6.1 Background

This study served as preliminary work for NIH Grant R21NS090131, which proposed to study the effects of minocycline treatment on traumatic brain injury (TBI). Anti-inflammatory treatments such as minocycline have been shown to attenuate cell death that can contribute to secondary injuries in TBI[49-51], but the effects had not been studied *in vivo*. During literature review in preparation for work on this grant, it was noted that previous experiments using minocycline reported an unexpected discrepancy in treated subjects of certain injury severity. While untreated mice showed less anxiety in tests such as the Elevated Plus Maze (EPM) and Open Field (OF) when compared to a sham group, treated subjects showed an equal or increased level of anxiety. Further reading revealed that severe levels of TBI could result in working memory deficits, impairing the ability to form spatial maps[52, 53]. It was hypothesized that similar memory deficits were inhibiting the affected animals' abilities to store information about their environment, resulting in mice that showed fewer traditional signs of anxiety. It was further hypothesized that the minocycline was protecting treated groups from similar memory deficits, which resulted in an increase in anxious behaviors after treatment when compared to untreated groups with similar injuries.

In order to examine this hypothesis, a study was planned to replicate the TBI conditions found in the literature and associated results from EPM and OF experiments. A third behavioral test, novel object recognition (NOR), was incorporated to determine if there was a relationship between memory deficits and anxious behavior. This study allowed the surgeons in the lab to begin training in surgical procedures that would be necessary to complete the goals of the NIH grant. The behavioral work also dove-tailed nicely with research performed by Dr. Kevin Holly, who had developed a program to measure stretch-attend-posture (SAP) as an additional measure in OF behavioral tests.

The behavioral tests used each have a widely accepted rationale provided in the literature. The EPM test allows researchers to study anxious behaviors based on the natural aversion mice display towards open spaces. The device created for the test consists of an elevated four armed apparatus, with open and closed arms intersecting in the middle. Increased avoidance of the open arms of the apparatus is directly related to an increased level of anxiety[54]. The apparatus design used in this study was previously described in the literature[55]. The OF test similarly measures anxiety based aversion to open spaces, but instead uses a completely open container. Using a grid painted on the container's base, the researcher can determine the amount of time a mouse spends in the open center versus against the walls, as well as trace the subject's path of travel over the duration of the experiment[56]. SAP is a specific behavior that occurs during the OF test, during which the animal performs risk assessment. The behavior is signified by the animal lowering its back, elongating its body, and reducing or completely stopping movement[57]. The specificity of the behavior allows SAP to be used as a more sensitive measurement in addition to previously mentioned outcomes of OF.

The NOR test measures the time an animal spends with a known object against the time spent with a newly introduced object. The subject is allowed to familiarize itself with a pair of identical objects, which are removed and replaced, one object identical to the original pair, the other novel. The percentage of time the subject spends with the novel object is compared between groups, with a lower percentage typically indicative of memory deficits[58]. By combining the NOR test with traditional anxiety related tests, associations between memory loss and anxiety could be detected.

6.2 Experimental Design

To test the effects of TBI induced memory deficits on anxious behavior, mice were divided into control, sham, and injured groups. These groups underwent behavioral tests including OF, EPM, and Novel Object Recognition (NOR) before and after injury. Based on previous findings in the literature, injured animals were expected to have more trouble distinguishing a novel object from a known object, implying short term memory deficits. The injured mice were also expected to show less anxiety in the OF and EPM tests, correlating the memory deficits with the lower anxiety scores previously demonstrated in the literature.

Forty male, wild type C57BL-6 lab mice aged 9 weeks old were acquired for the study (Envigo) and quarantined for 1 week after arrival. The mice were housed in a 12 hour day/night cycle where food was administered ad libitum. Mice were housed individually after quarantine to prevent discrepancies between controls and those undergoing surgery, which would require individual housing to prevent aggravation of the surgical site. Separating the mice also prevented discrepancies in anxiety levels observed during behavioral tests[54]. Three groups of ten mice were the end goal, with

an additional ten in reserve should an animal need to be eliminated. To alleviate the testing and surgical schedules, the forty mice were divided into six sets of six mice each, and one set of four.

Behavioral tests were performed in the first, third, fourth, and fifth week of the experimental period, beginning when the mice reached 10 weeks of age. The sets of mice were staggered according to the Gantt chart shown in the appendix so that each set of mice received 10 days of recovery time between injury and the resumption of behavioral tests. This recovery time was important, due to possible locomotive impairment that can occur shortly after TBI. Each mouse received a minimum of 24 hours between the OF and EPM behavioral tests to prevent the outcomes from one test measuring anxiety from affecting the other. As the most experienced lab member in the subject, Dr. Kevin Holly oversaw and analyzed the results of each test. However, it has been published that mice behave differently in the presence of a male handler. To prevent this, Dr. Holly instructed five female undergraduate assistants in the correct method of handling mice for the tests, and they conducted the experiments. The undergraduate assistants were not informed of the injury status of each mouse, blinding them to all but the control mice, which they could easily identify as uninjured.

Mice were recorded in both the OF and EPM to measure anxiety based on spatiotemporal location. SAP frequency was measured during these experiments. The NOR test was also given in order to detect and compare any cognitive decline that occurred over the course of the study.

Surgery and injury were performed by Ben Kemp and Dr. Chelsea Pernici. In the weeks leading to the experimental period, Mr. Kemp taught Dr. Pernici the surgical and

injury protocols he had learned from the members of the Lifshitz lab and described in Chapter 4. The surgical load was divided evenly between the surgeons, with Dr. Pernici implanting three hubs in the morning, and Mr. Kemp implanting three in the afternoon. Mice in the injured group received an injury on the same day that the injury hub was implanted, after surgeries had been completed. The severity of injury was quantified using the righting time of animal after impact, as has been described previously in the literature. Sham mice received an injury hub implant and were briefly attached to the fluid percussion device, but the impact was not carried out.

At the conclusion of the experimental period, each mouse underwent a set of baseline measurements for each behavioral test and three additional sets of measurements were acquired after TBI was induced in the injured group. The post-TBI data were normalized against the baselines to minimize differences attributed to the individual natures of each animal. Animals could then be compared over the course of the study to detect any significant difference between groups and to determine whether the three weeks post-TBI allowed for any recovery.

6.3 Surgical Procedure and Injury

A detailed description of the surgical procedures used in this research is provided in Chapter 4. The pertinent aspects are recounted here.

One week after initial training, mice were fitted with an injury hub in a procedure adapted from the literature[46]. Mice were given an intraperitoneal injection of ketamine/xylazine cocktail (10mg/mL ketamine, 0.1mL/10g xylazine) and the surgical site was cleared of fur with scissors. Once clear, mice were positioned in a Cunningham Mouse Adapter (Stoelting) with a nose cone attachment on a stereotaxic frame.

Anesthesia for the duration of the surgery was induced using 1.0% isoflurane gas, delivered with a Kent SomnoSuite (Kent Scientific). A 3 mm outer diameter trephine was used to drill a craniectomy. A previously cut 20 gauge hypodermic needle female end Luer-lock, sterilized in 91% isopropyl alcohol, was used as an injury hub. The hub was placed over the craniectomy with forceps and attached with a thin layer of cyanoacrylate (Loctite Ultra-gel) followed by a layer of dental cement (Relyx Aplicap, 3M). Mice were kept on 1.0% isoflurane for an additional twenty minutes to allow the cement to dry, then placed in an empty cage on a microwaveable heating pad (Braintree Scientific). Once awake, mice were returned to housing with food and water to await injury.

Mice were injured the same day surgery was performed, in the order the injury hubs were installed. TBI was induced using a fluid percussion device (Custom Design & Fabrication). Mice were allowed to acclimate to the room, then anesthetized in an induction chamber under 4.5% isoflurane. Level of anesthesia was determined by the lack of a righting response when the induction chamber was rotated and the depth of respiration. During this time, the fluid percussion device was primed to ensure a regular and consistent pressure wave was created in the fluid chamber, and the output from the pressure transducer in the device was recorded.

Once anesthetized, the injury hub was filled with sterile saline and the mouse hooked up to the male end Luer-lock of the fluid percussion device. The mouse was then laid on its side, and the pendulum dropped when breathing returned to normal, delivering an impact of 2.18 atm. Severity of injury was determined by righting time. Mice were deemed to have undergone a moderate concussion when righting time ranged between

360 and 600 seconds. After righting, mice were anesthetized at 4.5% isoflurane and the injury hub removed. After removal, isoflurane was reduced to 2.0%. The craniectomy was inspected and mice in which the brain had herniated through the opening were immediately euthanized. The removed injury hub was also inspected for occlusions that may have affected the pressure wave before it struck the dura. If the craniectomy was clear, the skull was sealed by first applying a thin layer of low melt agarose gel to protect the brain, followed by a 3 or 5 mm cover glass, depending on the gap in the remaining dental cement, and finally a layer of cyanoacrylate (Loctite). This sealing procedure prevented infection and allowed the skull to be sealed without closing the scalp. Sham mice followed the same procedure, but no impact was delivered. Once recovered, mice were returned to their home cage.

6.4 Surgical and Injury Results

A total of 30 mice underwent surgery for the initial trial period. The outcomes of these surgeries are provided in **Table 6-1**, and a breakdown of these outcomes by surgeon is provided in **Table 6-2**. For outcomes with injury, the severity of injury was determined by the time it took for the mouse to exhibit a righting response, which is the reflex a mouse exhibits when laid on its back. Because a mouse will typically immediately attempt to right itself, the righting response is often used to gauge when a subject has regained consciousness after a TBI. The righting times associated with level of severity are given as[46] 120 s < mild < 240 s, 360 s < moderate < 600 s, severe > 600 s.

Certain cases prohibited animals from continuing in the study. If the dura was torn during surgery or by the impact during TBI, the brain would herniate through the

craniotomy. This complication required the animal to be immediately euthanized. Additionally, the injury hub could become occluded by either the glue meant to seal it to the skull or by clotted blood. The occlusion disrupted the pressure wave from the fluid percussion device, also requiring the animal to be euthanized. Euthanasia was performed in compliance with the university's Institutional Animal Care and Use Committee (IACUC) guidelines. In cases of herniation or occlusion, the subject was immediately re-anesthetized, then euthanized by cervical dislocation.

Though the pressure wave was measured using a pressure transducer connected to an oscilloscope to ensure a consistent and appropriate waveform, as described in the literature[46], the resulting injuries were unexpectedly diverse. Instead of being consistently moderate as desired, injuries ranged from mild to severe. Six additional mice of the same strain were acquired (Envigo) and used to expand the groups to a statistically relevant population. The six additional mice were numbered M41-46, and their outcomes are also shown in **Table 6-1**. Six separate groups were obtained instead of the expected three, however the resources were not available to rectify the situation. Behavioral tests continued in the hopes that significant results could be obtained despite the small population sizes.

Table 6-1: Surgical Outcomes

Mouse ID	Surgery Date	Outcome	Injury Date	Outcome
M1	4/4/2016	Survival	4/4/2016	Euthanized
M2	4/4/2016	Death	-------	------
M3	4/4/2016	Death	-------	-------
M4	4/4/2016	Survival	4/4/2016	Severe
M5	4/4/2016	Survival	4/4/2016	Euthanized
M6	4/4/2016	Death	------	------
M7	4/5/2016	Survival	4/5/2016	Sham
M8	4/5/2016	Survival	4/5/2016	Mild
M9	4/5/2016	Survival	4/5/2016	Euthanized
M10	4/5/2016	Survival	4/5/2016	Moderate
M11	4/5/2016	Death	------	------
M12	4/5/2016	Survival	4/5/2016	Sham
M13	4/6/2016	Survival	4/6/2016	Moderate
M14	4/6/2016	Survival	4/6/2016	Sham
M15	4/6/2016	Survival	4/6/2016	Severe
M16	4/6/2016	Survival	4/6/2016	Sham
M17	4/6/2016	Death	------	------
M18	4/6/2016	Death	------	------
M19	4/7/2016	Death	------	------
M20	4/7/2016	Survival	4/7/2016	Sham
M21	4/7/2016	Survival	4/7/2016	Mild/Mod
M22	4/7/2016	Survival	4/7/2016	Moderate
M23	4/7/2016	Survival	4/7/2016	Euthanized
M24	4/7/2016	Survival	4/7/2016	Sham*
M25	4/8/2016	Survival	4/8/2015	Mild
M26	4/8/2016	Survival	4/8/2016	Mild/Mod
M27	4/8/2016	Survival	4/8/2016	Euthanized
M28	4/8/2016	Survival	4/8/2016	Moderate
M29	4/8/2016	Survival	4/8/2016	Moderate
M30	4/8/2016	Death	------	------
M41	5/8/2016	Survival	5/8/2016	No Injury
M42	5/8/2016	Death	------	------
M43	5/8/2016	Survival	5/8/2016	Euthanized
M44	5/8/2016	Survival	5/8/2016	Euthanized
M45	5/8/2016	Survival	5/8/2016	Mild/Mod
M46	5/8/2016	Survival	5/8/2016	Severe

Totals
Mild
Mild/Mod
Moderate
Severe
Sham
Euthanized
Deaths
Excluded
Total

Table 6-2: Outcomes by Surgeon

Surgeon Breakdown						
Surgeon	**Mild**	**Moderate**	**Severe**	**DOT**	**Herniation**	**Sham**
Ben	0	4	1	5	1	3
Chelsea	4	1	1	3	3	3

Herniation Breakdown			
	Mild	Moderate	Severe
Ben	0	1	0
Chelsea	1*	1	1

6.5 Behavioral Testing Schedule

Mice were divided into groups of six with tests staggered between groups to ensure that surgery occurred exactly one week after the behavioral baselines were acquired for each mouse. On day one, mice were placed in the EPM for 10 minutes. On day two, mice were placed in the OF for 5 minutes, immediately followed by the NOR test in the same apparatus. This step allowed the OF test to also function as an acclimation period for the NOR test, which reduced the possibility of anxiety causing negative effects on the results of the cognitive test. During the NOR test, two novel objects were presented for 5 minutes, after which a new object replaced one of the originals. The position of the new object was alternated between mice to prevent bias. Each test was repeated once a week for three weeks following the post-op recovery period. Retrograde memory loss was also tested during the NOR experiment by pairing the non-novel object from Week 1 of the behavioral tests with a completely novel object during post-TBI NOR tests.

6.6 Behavioral Testing Results

The behavioral testing results were organized by Dr. Kevin Holly and delivered to Ben Kemp in a consolidated spreadsheet. Then the animals were grouped according to injury status, and the parameters measured during the tests were analyzed.

The results of the EPM were analyzed first. The test was broken down into multiple parameters meant to characterize the subject's behavior, including the total distance the animal traveled, the amount of time spent in each arm or the center of the maze, and the total number of entries into either open or closed arms. The measurements were also converted to percentages when appropriate (for example, the percentage of time spent in an open arm of the maze over the duration of a day's experiment). The total time for each test was also recorded to ensure analysis was accurate in the case an experiment was ended prematurely.

Mouse handling created some difficulties in analysis of the EPM data. In some cases, it was reported that a mouse fell and recording could not be completed. This created holes in the data sets of individual mice, and, in one case, prevented normalization of results for a subject because the fall occurred in week one of the study. Complete representations of the collected data can be found in the appendix of this dissertation, but a representative selection is included in **Table 6-3**.

The representative selection in **Table 6-3** compares the percent open arm stay time for each group. When anxious, mice typically attempt to hide themselves in enclosed areas. Therefore, the amount of time spent in the open arms of the EPM is theoretically indirectly related to the anxiety level of the mouse. The mice in **Table 6-3** have been divided into groups based on their injury level: control (n=10), sham (n=4),

moderate (n=8), and severe (n=3). Columns with fewer mice than these group totals are the result of a fall from the EPM disrupting recording. Single factor ANOVA analysis was used to determine if a significant difference existed between the four groups. Unfortunately, the analysis showed no significant difference between groups in any measured parameter of the EPM.

Table 6-3: Representative Selection of Percent Open Arm Stay Time in EPM

Week 1 (%)			
Control	Sham	Moderate	Severe
0.80	3.83	7.62	3.83
9.88	0.37	16.12	0.28
6.58	16.64	2.73	14.32
2.17		24.69	
2.18		18.95	
23.64		11.27	
7.23		7.75	
19.00		7.55	
1.28			

Week 3 (%)			
Control	Sham	Moderate	Severe
0.08	5.73	0.18	2.58
15.12	3.00	2.58	0.00
0.00	0.60	1.80	0.70
1.62	6.60	0.32	
2.50		6.52	
0.70		5.42	
14.77			
0.63			
0.00			
1.53			

The parameters measured during the OF test were analyzed following review of the EPM metrics. The OF test was divided into the total distance traveled (cm), the average speed of the mouse in the enclosure (cm/sec), the number of movements the mouse made, and the total time spent in the center (sec). As with the EPM tests, the total duration of each OF test was also recorded. Unlike the EPM tests, the OF tests suffered considerably fewer handling errors. The improved handling practices allowed data to be normalized by subject.

Representative selections in **Table 6-4** compare the total center time (TCT) for each group. Similar to the open arms of the EPM, the center of the enclosure provides

less cover for the subjects. In theory, an animal suffering increased anxiety will prefer to remain near the walls of the enclosure and spend less time exploring the center of the open field. The mice included in **Table 6-4** are divided into the same groups used to examine the data obtained from the EPM. Again, columns with fewer entries are the result of handling errors that made data unusable. Single factor ANOVA analysis was used to determine if a significant difference existed between groups in each week. Although ANOVA analysis of the raw data showed a significant difference between the four groups ($p=0.026$) in week four, the difference was no longer significant once the data was normalized to the pre-injury recordings ($p=0.340$). This increased p-value in the normalized data indicated that the differences were due to the inherent nature of the individual animals, and not related to the experiment.

Table 6-4: Representative Selection of Total Center Time in Open Field

Week 1 (s)					Week 4 (s)			
Control	Sham	Moderate	Severe		Control	Sham	Moderate	Severe
2.2	41.2	35.5	43.8		0.6	20.7	6.3	18.5
6.1	32.1	10.2	4.4		2.6	9.1	5.2	13.2
11.4	7.6	2.7	12.5		1.4	3.9	1.2	0.7
8.9	6	22.5			1.3	8.4	1.2	
6.3		8.3			8.2		2	
8.3		6.5			4		11.5	
15.2		4.4			8.9		3.8	
5.7		36.5			0.5		2.2	
2.1					0			
1.2					0.6			

Interestingly, the total distance traveled in the OF as well as the average speed of the subject both returned significant differences in the ANOVA analysis each week post-injury. The total distance traveled was further analyzed in data obtained from Week 2,

which contained the greatest likelihood of significant difference from the three post-injury weeks ($p=0.003$). The normalized groups from Week 2 were further compared using the student's t-test. An F-test was applied to pairs used in the t-test to determine equal or unequal variance before applying the t-test. The t-test was first applied to the sham and control groups to determine if the significant difference was caused by the surgery alone. A one-tailed t-test between the sham and control groups showed no significant difference ($p>0.05$). After it was determined that the surgery was not the source of any behavioral changes, a one-tailed t-test was performed between the moderately injured group and the control group, a second one-tailed t-test was performed between the severely injured group and the control group, and a third one-tailed t-test was performed between the moderately injured and the severely injured groups. A one-tailed t-test was chosen because it was expected that injured groups would have a greater mean travel distance. In the second OF trial, both injured groups showed a significant difference in total distance traveled when compared to the control group, but there was no significant difference between the moderately injured and severely injured subjects. Full results of Week 2 are shown in the appendix.

Many factors beyond anxiety can affect the locomotive behavior of animals post-TBI. TBI itself is known to cause short term locomotive deficits, as well as increased locomotion in cases of severe injury[52, 59]. While the significant differences in locomotive behavior shown in this study are interesting, none of the metrics gauging anxiety supported a change in anxious behavior between the groups. With no change in anxious behavior, and lacking resources to expand the experiment with additional surgeries and behavioral tests, it was decided that analysis of the NOR data could not

support or refute the original hypothesis. The behavioral portion of the experiment was deemed inconclusive.

6.7 Histology

A histological analysis followed the inconclusive behavioral tests. For this analysis, it was hypothesized that the structures directly beneath the craniectomy would be damaged by the trauma. Animals that received more severe injuries were expected to have received axonal damage, which would be detected as a thinning of the corpus callosum or the external capsule, and memory deficits, which would exhibit as a loss of neuronal cells in the hippocampus. The null hypothesis was represented by no change in either region between groups. This analysis was overseen by Ben Kemp with the assistance of Kayla Ponder. The analysis was limited to resources already available, so it was decided the analysis would proceed using a Luxol Fast Blue stain with a Cresyl Violet counterstain. The Luxol Fast Blue stain highlights the myelinated axons that create white matter tracts in the brain, and creates a more easily discerned image of the corpus callosum and external capsule than traditional H&E staining. The Cresyl Violet stain is incorporated into Nissl bodies in the neurons of the brain, allowing for specific identification of neuronal cell bodies at the exclusion of surrounding glial cells. This specificity allowed researchers to measure the density of neuronal cells near the CA1 region of the hippocampus.

Tissue was collected from the mice after the initial analysis of the behavioral results proved inconclusive. Mice were deeply anesthetized with the previously described ketamine/xylazine cocktail, then underwent cardiovascular perfusion. During this procedure, the animal's thoracic cavity was opened surgically to expose the heart. A

hypodermic needle connected to a peristaltic pump was inserted into the left ventricle, and the right atrium was lacerated to drain blood from the animal. A phosphate buffered saline (PBS) solution was first pumped through the animal's circulatory system to clear the blood, which can react negatively with various stains and fixatives. When the fluid draining from the right atrium appeared clear, the PBS was switched to a formalin solution, lightly fixing the tissue. After 20 mL of formalin had run through the system, the animal's head was removed along with any extraneous tissue. The brain was left encased in the skull and submerged in a sufficient volume of formalin, then refrigerated overnight. In previous preparations, it was noted that attempting to remove the brain immediately after perfusion often resulted in a portion adhering to the skull, damaging the tissue. This event occurred less often if removal was delayed until after the overnight fixation.

The following day, the brain was removed from the remaining skull and subjected to a dehydration and infusion series, eventually being embedded in paraffin wax. This method was modified from tissue preparation protocols developed and taught to the researchers by Drs. James Spaulding and Brandon Moore. Dehydration was accomplished by submerging the tissue in alcohol solutions at increments of 70% (2 hours), 85% (1 hour), 95% (2 hours), and two separate solutions of 100% ethanol (2 hours each). The alcohol was then replaced with a miscible organic solvent (Histoclear, Amresco), once again in two separate steps of 2 hours each. The sample was then placed into heated containers of solvent/paraffin solutions in two steps. The first step was a 1:3 ratio of paraffin to solvent, and by necessity lasted overnight. The second step was a 3:1 ratio of paraffin to solvent, for 2 hours. The final step moved the sample to a pure

paraffin solution contained in a vacuum oven for 24 hours. The sample could then be stored until researchers were ready to section the tissue, or it could be immediately embedded in a paraffin block for sectioning.

Coronal sections were obtained using a microtome (Olympus Cut 4060) located in the core histology facility (BME 134). The majority of samples were sectioned at 10 µm thickness, though three of the first samples sectioned experienced some variance as the optimal sectioning thickness was determined. A table containing the thickness of sections taken from each brain, as well as the total amount of tissue mounted, the amount of tissue discarded, and ancillary notes can be found in the appendix. The sectioned ribbons were cut to size using a razor blade, floated in a heated bath of RO water, then mounted on slides and placed on slide warmers to dry overnight. The tissue beneath the craniectomy was considered the region of interest. In order to reduce the amount of tissue sectioned on the microtome, the brain was first cut to smaller dimensions using a metal brain matrix as a guide. The matrix was used to remove the olfactory bulbs rostrally, and the cerebellum caudally. An image of a brain being prepared in the matrix can be found in **Figure 6-1**. The extraneous tissue was removed after the first step of dehydration, because it was found that the dehydration process stiffened the tissue, making it easier to cut the tissue without deforming it. After the sample was embedded in paraffin and mounted in the microtome, coronal sectioning began from the rostral end of the sample, providing enough tissue before the region of interest to ensure the researcher could obtain a regular ribbon.

The mounted samples were stained with Luxol Fast Blue and a Cresyl Violet counterstain. Protocols for mixing the dyes and the staining procedure can be found in

the appendix. The slides were initially examined using a dissecting scope (BME 214) in order to obtain a planar image of the full section, then later examined under a 40x objective using the Olympus IX51 microscope located in the core imaging lab (BME 225). An image of a calibration slide was also captured under the same magnification used to record images of the stained sections to create accurate scale bars.

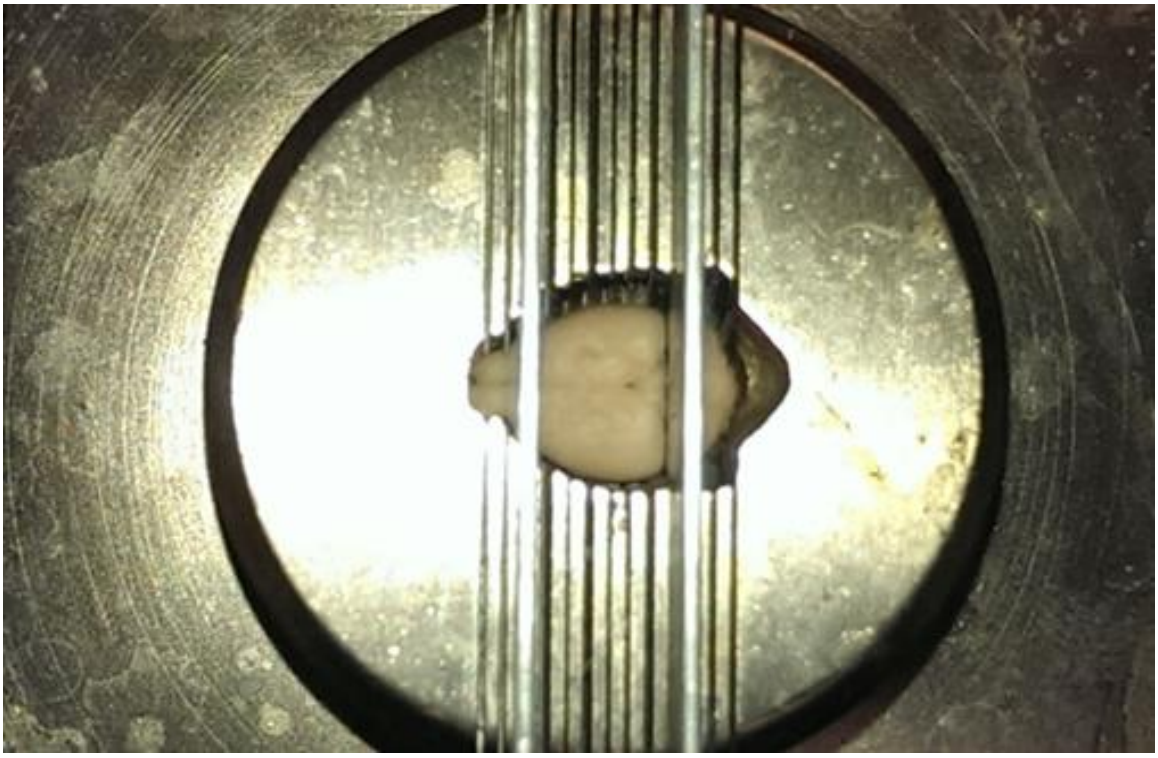

Figure 6-1: Each mouse brain in was placed in the metal matrix and cut in preparation for sectioning. The matrix was used to remove the olfactory bulbs (left, rostral) and the cerebellum (right, caudal). Coronal sections were taken, beginning at the rostral end of the sample. This provided the researcher with ample tissue to obtain a regular ribbon before reaching the region of interest.

6.8 Histology Results

An example of the successfully stained slide is shown in **Figure 6-2**. The image is also overlaid with black bars marking the points where the thickness of various structures was measured for comparison. The slides used for comparison were judged to

be as near as possible to the representation of the coronal section located at Bregma -1.82 mm in Paxinos and Franklin's Mouse Brain Atlas. This location was near the center of the craniectomy, and contained the smallest area of ventricles in the region, which proved important for the section's integrity.

One section from each animal was chosen to be analyzed. The choice was made by qualitative observation of the proximity of the section to region of interest and the integrity of the tissue in the section. The sections were measured at the center of the corpus callosum, the medial portions of the external capsule on the left and right sides of the brain, and near the CA1 regions of the hippocampus on the left and right sides of the brain. The thickness of a region was defined as the length of a line drawn across the region as shown in **Figure 6-2**. These lines were drawn quantitatively in ImageJ using the line selection tool. Once a region had been selected, the selection was added to the ImageJ ROI Manager. When selections for each region had been added to the ROI Manager, the contents of the ROI Manager were saved as a separate file labeled with the associated section, allowing those exact regions to be reused in future analysis.

Using the Set Scale feature in ImageJ, the pixel/micron ratio was set for each section as determined by the image of the calibration slide. Once this information was entered, the Measure function in ImageJ could be used to determine the thickness of each region of interest in the appropriate units. These thicknesses were recorded and organized by injury group for comparison. A table containing the measured thickness of each section grouped by injury severity can be found in the appendix. The groups contained the same numbers of mice as reported previously regarding the EPM.

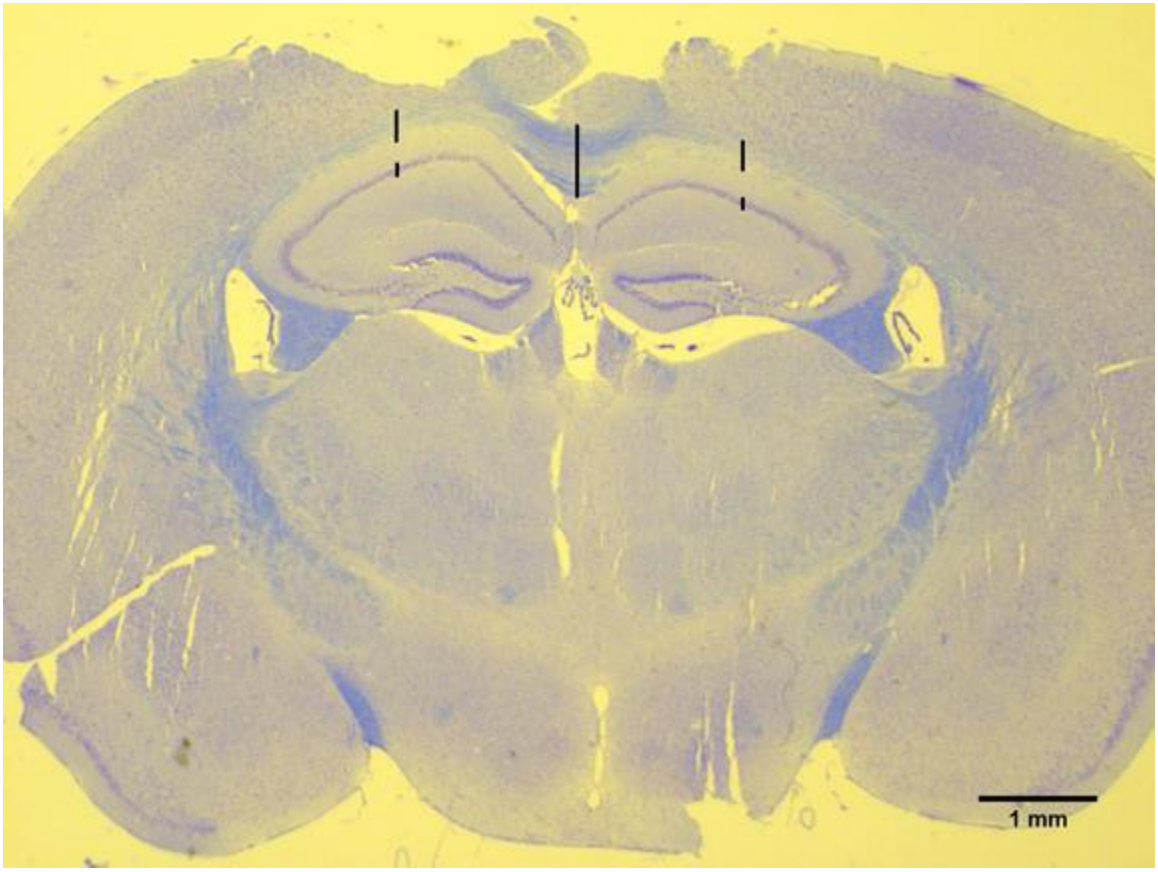

Figure 6-2: A coronal section taken from a severely injured mouse (M4) stained with Luxol Fast Blue and Cresyl Violet. The black bars show the locations of measurements taken to judge the thickness of the corpus callosum, external capsule, and neurons in the hippocampus.

Single factor ANOVA analysis was used to compare the measurements from control, sham, moderately injured, and severely injured mice. A significant difference was indicated in the output for the corpus callosum measurements. Further analysis using a student's one-tailed t-test showed that a significant difference existed between the control and sham groups ($p=0.024$), calling into question the cause of the difference. A significant difference also existed between the severe and control groups, as well as the severe and moderate groups. Interestingly, the severe and sham injured mice exhibited a higher mean thickness in the corpus callosum than control and moderate mice. This ran counter to expectations, as it was hypothesized that axonal damage and subsequent

recovery would result in a reduction of the stained area. One possibility is that the area appeared expanded as a result of surgery and reacted differently to a moderate or severe TBI. However, further experiments are required to support that conclusion. Because a significant difference existed between the control and sham groups, and in consideration of the small sample size of severely injured animals, the results of this analysis were deemed inconclusive.

Single factor ANOVA was also used to compare the measurements of the external capsule and CA1 regions of the hippocampus. No significant difference was found among the groups in any of these regions.

Before moving to higher magnification images, a second test was devised to further analyze the regions containing luxol fast blue stain. For this analysis, it was hypothesized that areas with increased myelin would retain more of the stain, and that the amount of stain stored in the tissue could be quantified using the histogram function in ImageJ. In an RGB image, each pixel is assigned a red, green, and blue value ranging from 0 to 255. The histogram function can be used to quickly count the number of pixels of each value by sorting them into separate bins. The mean, minimum, maximum, and mode color values were also output, as well as the standard deviation. In an RGB image, the histogram function was capable of sorting by desired color value, and could also limit the analysis to a specific region of interest.

The most difficult part of this analysis was accounting for the different architecture between brains. Although each section was as near to the previously described coronal section in the brain as possible, slight variations in architecture are common between animals. Although precautions were taken to prevent it, differences

were sometimes exacerbated by the process of extracting the brain from the skull or through the stresses imparted by sectioning and mounting. These architectural differences made it extremely difficult to pick a single region of interest large enough to adequately capture damage while also maintaining the exact region size across all tissue sections. Instead, a region of sufficient size was defined for each section that fit both in the internal capsule as well as the corpus callosum. A representation of the regions used can be found in **Figure 6-3**. It was hypothesized that the corpus callosum, being directly beneath the surgical site and the point of impact, would suffer from greater myelin loss than the more lateral and ventral internal capsule. Comparing the ratio of the mean corpus callosum blue value to the mean internal capsule blue value of each section rather than directly comparing the mean blue value of a single area would help mitigate differences caused by dimensional changes in architecture.

Single factor ANOVA was used to compare the groups as previously discussed. The sections used were the same as those used for previous measurements, and regions of interest were defined and saved in the same manner. ANOVA indicated a significant difference existed between groups ($p=0.004$). After a series of paired comparisons using one-tailed student's t-tests, it was found that the sham injured mice may have exhibited a significant difference from the control group ($p=0.0494$), but that the probability of a significant difference between the moderately injured and control groups was much higher ($p=0.013$). The moderate group also significantly differed from the sham and severely injured groups ($p=0.030$ and $p=0.025$, respectively), but the severely injured group did not significantly differ from the control or sham groups. Interestingly, the results follow a similar pattern to the previous histology results, in that the mean sham

and severely injured values increased in comparison to the mean control group value, but the mean moderately injured value was lower than either the sham or severely injured group. In this case, however, the mean moderately injured group value was also lower than the mean control group value. Once again, it was difficult to draw a meaningful conclusion with such a large difference between the control and sham groups.

Figure 6-3: A coronal section from a control mouse (M31) stained with Luxol Fast Blue and Cresyl Violet. Callouts indicate the regions used for comparison. The region size was constant between the corpus callosum (upper left) and external capsule (lower right). Scale bar is 1 mm.

The final histological analysis focused on the CA1 region of the hippocampus. This analysis attempted to take a closer look at the region using the images taken through the 40x objective to determine if there was cellular loss that was not detectable with

lower magnification. ImageJ was again used to complete this analysis, this time using the Area Fraction measurement. Unlike cells grown *in vitro*, cells in the brain are often irregularly shaped or simply not regular across the plane of the section. The shapes and close proximity of the cells made traditional cell counting methods painstaking and inaccurate. However, the lack of myelin near the hippocampus meant the CA1 cells were the only cells stained in the region. Instead of attempting to count individual cells, the image was adjusted to determine the percent area the CA1 band occupied in the image.

Images of the CA1 band were taken at the previously measured locations. Images were taken of the CA1 band on the left and right side of the brain in two different tissue sections per animal. Area fractions of the CA1 region were only compared to others taken on the ipsilateral side. To acquire the area fraction, the brightfield images were first changed into 8-bit tiff images. This step removed all color data from the image, leaving stained areas black and unstained areas white. A threshold was then applied to the image to reduce the black areas to only whole cells. At this point, the researcher would define the CA1 region with a freehand selection and clear anything outside of the selection from the image. This removed any nearby neuronal cells and other artifacts from the image, leaving only the CA1 region. The selection was saved in the ROI manager, then the measure function was used to determine and record the area of the freely drawn selection. The area was de-selected, and the measure function was used to determine the area fraction of the CA1 in the image. A side by side comparison of the original brightfield image and the thresholded image used to calculate the area fraction is shown in **Figure 6-4**.

The area fractions were converted from decimals to percentages, and the percentages were sorted into the appropriate injury groups. Single factor ANOVA analysis was used to compare the groups, but returned no significant difference in the CA1 region on either side of the brain.

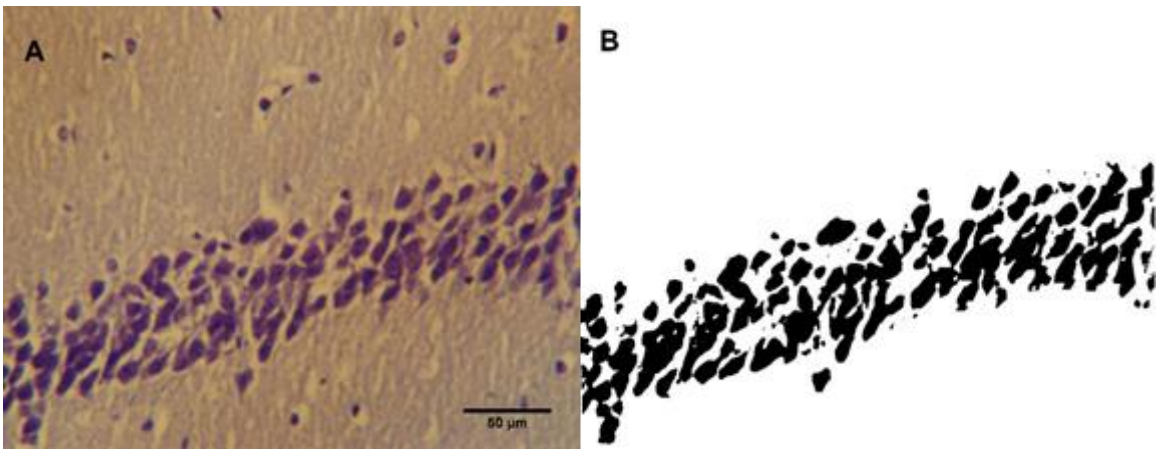

Figure 6-4: A 40x magnification image of the CA1 region stained with Cresyl Violet before and after thresholding. A shows the brightfield image of a section acquired from subject M4 with scale bar before any post processing effects had been applied. B shows the same section as it appeared when the area fraction measurement was acquired. As described in the text, the original image was converted to an 8 bit format, a threshold was applied, and anything outside the area the researcher defined as the CA1 band was cleared. Scale bar is 50 µm.

6.9 Discussion

The lack of significant results was a disappointing outcome. With greater statistical power, it is expected that some of the observed trends may have become more pronounced to the point that a significant difference was measurable, but the estimated number of mice needed for this study could not account for the unexpected variations in injury level. Unfortunately, due to a lack of resources and available personnel, the experiments could not be expanded or repeated. However, the attempt provided much needed experience to the researchers in experimental design, coordinating efforts

between researchers with different areas of expertise, and techniques ranging from basic animal handling (an important skill for undergraduates intending to continue on to graduate level research) to advanced surgery, injury models, behavioral analysis, and histology.

The unexpected variation in injury level was a major setback for this study, and as such deserves further discussion. While the surgeons did not have experience with the exact surgery used to attach the injury hub, the surgical techniques were very similar to those used to implant a gradient index lens, a surgery the researchers were intimately familiar with. Though the integrity of the dura is tantamount to experiments using fluid percussion to create a diffuse traumatic injury, a stark deviation from the implantation of a lens that plunges through the dura and into the cortex, unfamiliarity with the specific surgical techniques are unlikely to have caused the variability. Failure to preserve the dura would have resulted in herniation of the brain after the injury had been induced, a condition which prevented subjects from progressing in the study. Occlusion of the injury hub by either the adhesive used to secure it to the skull or coagulated blood exuded by the damaged trabecular bone of the skull, or, in turn, a failure to adequately seal the injury hub to the skull would have been a more likely culprit, however these conditions were thoroughly investigated before and after the induction of injury. Instead, the variability was likely caused by the device used to induce the traumatic brain injury.

The fluid percussion device used in this research has a long history in the literature, and it is not the intent of this discussion to call the effectiveness of the method into question. The cause of the unexpected variability was likely due to a fault in the specific device used in this research which was repaired after the research concluded, but

which initially went undetected due to the researchers' lack of experience with the device. The two major causes of variance in the fluid percussion device were air bubbles in the fluid chamber and leaks. A pressure transducer attached near the end of the fluid percussion device and connected to an oscilloscope is meant to detect the variance these conditions can cause, typically observed as an irregular peak in the oscilloscope display. However, during prior use of the fluid percussion device, a leak had occurred beyond the pressure transducer, and it was improperly sealed with Parafilm (MIDSCI). While Parafilm is often used to seal containers in the lab, its elastic nature is a detriment in this application. As the pressure wave passes, energy is lost in the mechanical deformation of the film, resulting in the varied levels of injury observed in this research. The researchers, inexperienced in the use of the device and observing the expected waveform on the oscilloscope, did not realize a problem existed until it was far too late. It was not until Dr. Rachel Rowe, who has worked in the Lifshitz lab and is much more experienced in fluid percussion injury, visited the Murray lab to advise on a later experiment that the fault in the fluid percussion device was detected and properly repaired.

The technique used to seal the craniectomy after removal of the injury hub differs from previously published descriptions in the literature. Typically, the skin around the injury hub is left intact and sealed over the craniectomy with either a veterinary adhesive or sutures after the injury occurs. However, this research also intended to serve as a precursor to the development of an injury model that could be used in conjunction with an implanted lens. Dr. Chelsea Pernici was able to complete development of such a model for the research published in her dissertation.

This experiment initially set out to determine if some of the behavior described in the literature as reflective of a change in anxious behavior could instead be rooted in memory deficits. Even though the researchers met with setbacks that proved to be insurmountable, the process of designing and running the experiment provided a powerful learning opportunity and aided in the development of a successfully applied novel imaging technique.

CHAPTER 7

CONCLUSION AND FUTURE WORK

A novel imaging device, its implantation technique, and the procedure for acquiring images have been presented. This device was modeled after endoscopic devices previously presented in the literature, with the intention of adapting them for wider use. These adaptations included lowering the profile of the GRIN lens implant, both on the surface of the skull and within the implanted tissue, and maintaining the implant for an extended period of time better suited for longitudinal experiments. This body of work shows another step in the continued improvement of *in vivo* imaging techniques, which will hopefully provide a better understanding of the brain in both its natural functions and response to traumatic injury.

In vivo imaging is a valuable resource in both basic research and pre-clinical trials. The techniques demonstrated should be readily adaptable to experiments including fluorescent cell lines, as shown in this work, as well as those using fluorescent dye or particle injections. This would not only allow future researchers to obtain high resolution images of natural architecture without sacrificing the animal, but to also observe dynamic functions over periods of time alternative methods are incapable of providing. In pre-clinical trials, the demonstrated techniques can be applied to observe the effects of treatment at multiple time points in a single animal, potentially vastly reducing the amount of subjects required to successfully observe impacts.

As with any design, there is room for improvement in both the device's capabilities as well as its manufacture. An interesting possibility that was not discussed in this work is the potential of a compound lens. A compound lens can be created by simply continuing to alternate glass windows and GRIN lenses during construction, resulting in a much longer lens capable of penetrating deeper into tissue. However, such lenses are incredibly fragile, and it is unclear if they could survive for an extended implantation period without mechanical support. An attempt to develop a compound lens design was made during the course of this research in order to capture dynamic events along the rostral migratory stream, but limitations in lens components and restrictions in the animal model quickly curtailed this direction of research. Future projects with access to a wider variety of GRIN lenses or performed in a larger animal model could see further improvements in imaging based on a compound lens design.

The most obvious approach to improving the manufacturing process for this implant would be to eliminate the individually machined parts. Alternative designs created by fellow lab members took advantage of 3D printing, however these designs were much closer to a traditional headplate in size[45, 60]. Also, as previously mentioned in Chapter 5, certain plastics produce autofluorescence, requiring a much wider imaging port in order to avoid obscuring the desired image. However, 3D printing with metal instead of plastic may allow future researchers to hasten the manufacturing process without introducing detrimental effects. This option was not pursued during the course of this research, as the capability was not available to the researchers. If such a method could produce an even surface that allowed the GRIN lens to be appropriately aligned with the objective, it would serve as an effective substitute that would reduce the

need for specialized skills in production as well as the amount of time invested to create each implant.

This work also describes the foundation of a protocol for the study of TBI and considered the possible role of memory deficits during the examination of behavioral changes. This protocol and the low profile GRIN lens implant were later adapted and combined by Dr. Chelsea Pernici to produce high resolution, *in vivo* images of axonal reactions to TBI. Future studies of this nature may allow researchers to gather longitudinal data on both the behavioral and physical reactions to TBI treatment.

The device, techniques, and procedures presented in this research continue to expand a unique spatio-temporal niche between histology and non-invasive imaging. They have shown that GRIN lenses are capable of acquiring high resolution, *in vivo* images over the course of months, expanding their use to longitudinal experiments. When designed appropriately, these implants are at low risk of accidental removal and do not put an undue burden on the animal. GRIN lenses are shown here to be a viable alternative to sacrificial histological techniques and an effective means of streamlining longitudinal studies.

APPENDIX A

LETTER OF APPROVAL FROM LOUISIANA TECH UNIVERSITY INSTITUTIONAL ANIMAL CARE AND USE COMMITTEE

INSTITUTIONAL ANIMAL CARE AND USE COMMITTEE
Louisiana Tech University

January 29, 2016

Teresa Murray, Ph.D.
Biomedical Engineering
Louisiana Tech University
Campus Box #58

Dear Dr. Murray:

The Louisiana Tech University's Institutional Animal Care and Use Committee (IACUC) examined your protocol and via the committee review process approved your protocol entitled:

In Vivo Imaging and Neural Electrophysiological Recording in Rodent Brain for Biomedical Research

Your protocol has been assigned the following number: **2016-01**. All changes and procedures have been noted. If changes to your research are necessary, please know you will need prior approval from the IACUC. This protocol will expire **January 29, 2019.**

Please remember that you are required to keep adequate and accurate records of all procedures, results, and the number of animals used in this protocol for three years after termination of the project. These records must be available for review by the IACUC or state and federal animal use agencies. Each year in October you will be required to complete a summary of animals used for the United States Agricultural Agency (USDA). Note, that failure to follow this protocol as approved may result in the termination of research.

If you have any questions concerning the animal part of your research please contact me via e-mail at eborn@latech.edu.

Sincerely,

Emily Born, IACUC Chair
Louisiana Tech University

APPENDIX B

HISTOLOGY EXAMPLE PROTOCOL

B.1 Stain Preparation and Protocol for Luxol Fast Blue with Cresyl Violet[3]

Fixation

Formalin.

Sections

Paraffin, 10-15 µm.

Preparation of solutions

Luxol Fast Blue

Luxol Fast Blue	1 g
Methanol (absolute)	1000 mL
10% acetic acid	5 mL

Mix reagents and filter

Cresyl violet stock solution

Cresyl violet	0.5 g
Distilled water	100 mL

Acidified cresyl violet solution

Add 0.8 mL of 10% acetic acid to 100 mL of stock cresyl violet solution and filter before use.

Method

1. Take sections on slides to 95% alcohol
2. Stain in luxol fast blue solution, 2 hours at 60ºC, or 37ºC overnight
3. Wash in 70% alcohol
4. Wash in tap water (note: modified to RO water)
5. Differentiate in 0.1% lithium carbonate solution until the gray and white matter are distinguished. This may be more easily controlled by using 0.05% lithium carbonate followed by 70-95% alcohol instead.
6. Wash in tap water (note: modified to RO water)
7. Check differentiation under the microscope. Repeat step 5 if necessary.
8. Stain in cresyl violet solution, 10-20 minutes.
9. Drain sections and transfer to 70% alcohol. Avoid placing the section in water at this stage as the cresyl violet staining loses some of its intensity. Gently agitate the sections; the cresyl violet dye will flood out. The 70% alcohol differentiates the cresyl violet stain. Optimally, the cresyl violet should be removed, leaving the cell bodies and Nissl clearly visible. Do not over-differentiate; the 70% alcohol will take out the cresyl violet and to a certain extent the luxol fast blue. The cresyl violet counterstain will deepen the color of the luxol fast blue stained myelin from turquoise to a deep blue.
10. Dehydrate, clear in xylene, and mount in DPX

APPENDIX C

TRIO SYSTEM HEATED BASE DATA

Table C-1: Test 1 (Flow 1 to 5)

Test 1						
Time (minutes)	**Temp in water bath (Celsius)**	**Lane 1 (Input) (Celsius)**	**Lane 2 (Celsius)**	**Lane 3 (Celsius)**	**Lane 4 (Celsius)**	**Lane 5 (Output) (Celsius)**
0	40	32	34	35	31	22
5	39	35	36	36	34	24
10	39	36	36	36	34	23
15	39	36	36	36	35	24
20	39	36	36	36	33	24
25	39	36	36	36	35	24
30	39	36	36	36	32	24
40	40	36	36	36	33	24
50	40	36	36	36	33	25
60	40	36	37	37	34	24

Table C-2: Test 2 (Flow 5 to 1)

Test 2						
Time (minutes)	**Temp in water bath (Celsius)**	**Lane 5 (Input) (Celsius)**	**Lane 4 (Celsius)**	**Lane 3 (Celsius)**	**Lane 2 (Celsius)**	**Lane 1 (output) (Celsius)**
0	40	21	27	30	30	30
5	37	24	32	33	33	33
10	39	23	32	33	33	33
15	39	24	32	34	33	33
20	40	24	32	34	34	34
25	41	25	31	34	34	34
30	41	24	33	35	35	35
40	41	24	33	35	35	35
50	41	24	35	36	35	35
60	42	25	34	36	36	36

Table C-3: Test 3 (Flow 1 to 5)

Test 3						
Time (minutes)	**Temp in water bath (Celsius)**	**Lane 1 (Input) (Celsius)**	**Lane 2 (Celsius)**	**Lane 3 (Celsius)**	**Lane 4 (Celsius)**	**Lane 5 (Output) (Celsius)**
0	41	33	33	33	27	23
5	40	35	35	35	31	24
10	40	35	35	35	30	24
15	40	35	35	35	31	24
20	40	35	35	35	31	24
25	39	35	35	35	31	24
30	39	34	34	34	30	23
40	39	35	35	35	32	24
50	39	34	34	34	32	24
60	39	34	34	34	32	24

Table C-4: Average Temperature at Each Position

Averages						
Time (minutes)	**Temp in water bath (Celsius)**	**Lane 1 (Celsius)**	**Lane 2 (Celsius)**	**Lane 3 (Celsius)**	**Lane 4 (Celsius)**	**Lane 5 (Celsius)**
0	40.3	31.7	32.3	32.7	28.3	22.0
5	38.7	34.3	34.7	34.7	32.3	24.0
10	39.3	34.7	34.7	34.7	32.0	23.3
15	39.3	34.7	34.7	35.0	32.7	24.0
20	39.7	35.0	35.0	35.0	32.0	24.0
25	39.7	35.0	35.0	35.0	32.3	24.3
30	39.7	35.0	35.0	35.0	31.7	23.7
40	40.0	35.3	35.3	35.3	32.7	24.0
50	40.0	35.0	35.0	35.3	33.3	24.3
60	40.3	35.3	35.7	35.7	33.3	24.3

Table C-5: Square Error of the Mean for Each Position

SEM						
Time (minutes)	**Temp in water bath (Celsius)**	**Lane 1 (Celsius)**	**Lane 2 (Celsius)**	**Lane 3 (Celsius)**	**Lane 4 (Celsius)**	**Lane 5 (Celsius)**
0	0.33	0.88	1.20	1.45	1.33	0.58
5	0.88	0.67	0.88	0.88	0.88	0.00
10	0.33	0.88	0.88	0.88	1.15	0.33
15	0.33	0.88	0.88	0.58	1.20	0.00
20	0.33	0.58	0.58	0.58	0.58	0.00
25	0.67	0.58	0.58	0.58	1.33	0.33
30	0.67	0.58	0.58	0.58	0.88	0.33
40	0.58	0.33	0.33	0.33	0.33	0.00
50	0.58	0.58	0.58	0.67	0.88	0.33
60	0.88	0.67	0.88	0.88	0.67	0.33

APPENDIX D

IMAGE ACQUISITION

This appendix provides additional specifications for acquiring images using the multiphoton microscope not described in the main text, with an emphasis on how these specifications affect the time it takes to acquire the image. The settings used to acquire the mosaic shown in Figure 5-3 are detailed in order to provide a concrete example.

Key Terms:

Resolution: Image resolution is determined by the number of pixels per area in a given image. Each pixel is a two dimensional area on the image the computer assigns with a discrete color value. In the case of multiphoton imaging, these values will be acquired in grayscale and later pseudocolored using a lookup table based on the light filter. Increasing the number of pixels available while the overall imaging area remains constant allows for better detection of gradual shifts in color values, resulting in a more detailed image.

Dwell Time: During imaging, the laser raster scans over the pre-defined capture area. Dwell time refers to the length of time the laser is allowed to rest on each pixel, and is typically measured in microseconds.

Frame Time: Frame time refers to the amount of time it takes the system to capture a single scan of an x-y plane in the pre-defined area. Dwell time and image resolution both directly impact the frame time, but are not the only factors that do so. Limitations

inherent to the system, such as the time it takes hardware to correctly position components or the computer's processing speed, will also affect the frame time. Slidebook does not provide the formula for calculating frame time, but does provide an estimate that accounts for factors beyond dwell time and resolution. This estimate is provided in seconds, and updates immediately after a resolution and dwell time are applied.

The raw data used to create the mosaic featured in Figure 5-3 was acquired in four stacks with the following imaging specifications that affected the capture time:

Resolution (pixels): 1024 x 1024 y

Dwell time (µs): 2

Frame time (s): 4.46

Range (µm): 50

Step size (µm): 2

Averages: 4

As is evident from the provided specifications, additional factors beyond dwell time and resolution affect the total frame time. The range indicates the total extent of the image in the z direction, and the total number of frames can be determined by using the range and the step size. In this case, the total will be 26, as there is one plane per each step as well as an initial frame at the starting point. Determining the total time to acquire an image stack now only requires multiplying the total number of frames by the frame time, which results in an acquisition time of about 1 minute and 56 seconds.

However, a stack of single frames is often susceptible to background noise. Background noise is random, so the simplest way to reduce it is to capture multiple

frames at each plane along the z-axis and average them together. In the example shown, each plane was an average of 4 frames, meaning the total capture time also increased fourfold. The final total capture time of each image stack was actually 7 minutes and 44 seconds.

Unfortunately, not everything shown in Figure 5-3 could be captured in a single image stack because the microscope's field of view is smaller than that of the GRIN lens. In order to capture the complete image, four stacks were taken with x and y dimensions of 200 µm each. The total time needed to acquire the mosaic (only considering capture time and not setup) was nearly 31 minutes.

In summary, the largest influencers on the total frame time are the image resolution and the dwell time. The total time to image an entire stack will depend upon the extent of the stack in the z direction, as each plane will require a new frame to be captured. Finally, any averaging will require additional frame captures, further increasing the total capture time of an experiment.

APPENDIX E

CHAPTER 6 SUPPLEMENTARY MATERIAL

E.1 Gantt Chart

Table E-1: Behavioral Testing and TBI Surgery Gantt Chart

	Mon	Tue	Wed	Thu	Fri	Sat	Sun
Mouse	3/28/16	3/29/16	3/30/16	3/31/16	4/1/16	4/2/16	4/3/16
Set 1	EPM - AP	OF&NO - TG					
Set 2		EPM - KH	OF&NO - KaP				
Set 3			EPM - SS	OF&NO - AS			
Set 4				EPM - TG	OF&NO - KaP		
Set 5					EPM - TG	OF&NO - KaP	
Set 6						EPM - AP	OF&NO - SS
Set 7							EPM - TG
Set 8							

	Mon	Tue	Wed	Thu	Fri	Sat	Sun
Mouse	4/4/16	4/5/16	4/6/16	4/7/16	4/8/16	4/9/16	4/10/16
Set 1	Surgery						
Set 2		Surgery					
Set 3			Surgery				
Set 4				Surgery			
Set 5					Surgery		
Set 6						Surgery	
Set 7	OF&NO - KaP						Surgery
Set 8							

Table E-2: Behavioral Testing and TBI Surgery Gantt Chart contd.

	Mon	Tue	Wed	Thu	Fri	Sat	Sun
Mouse	4/11/16	4/12/16	4/13/16	4/14/16	4/15/16	4/16/16	4/17/16
Set 1	EPM - SS	OF&NO - TG					
Set 2		EPM - KH	OF&NO - KaP				
Set 3			EPM -AP	OF&NO - AS			
Set 4				EPM - CB	OF&NO - TG		
Set 5					EPM - AP	OF&NO - KaP	
Set 6						EPM -AP	OF&NO - TG
Set 7							EPM - SS
Set 8							

	Mon	Tue	Wed	Thu	Fri	Sat	Sun
Mouse	4/18/16	4/19/16	4/20/16	4/21/16	4/22/16	4/23/16	4/24/16
Set 1				EPM - MA	OF&NO - KaP		
Set 2					EPM- TG	OF&NO - TG	
Set 3						EPM - KaP	OF&NO - MA
Set 4							EPM - TG
Set 5							
Set 6							
Set 7	OF&NO - KaP						
Set 8							

Table E-3: Behavioral Testing and TBI Surgery Gantt Chart contd.

	Mon	Tue	Wed	Thu	Fri	Sat	Sun
Mouse	4/25/16	4/26/16	4/27/16	4/28/16	4/29/16	4/30/16	5/1/16
Set 1							EPM - MA
Set 2							
Set 3							
Set 4	OF&NO - KaP						
Set 5	EPM -AP	OF&NO - CB					
Set 6		EPM - KaP	OF&NO - KaP				
Set 7			EPM -AP	OF&NO - AS			
Set 8							EPM - MA

	Mon	Tue	Wed	Thu	Fri	Sat	Sun
Mouse	5/2/16	5/3/16	5/4/16	5/5/16	5/6/16	5/7/16	5/8/16
Set 1	OF&NO - KaP						
Set 2	EPM - SS	OF&NO - KeP					
Set 3		EPM -MA	OF&NO - KaP				
Set 4			EPM -AP	OF&NO - AS			
Set 5				EPM -MA	OF&NO - KaP		
Set 6					EPM - SS	OF&NO - TG	
Set 7						EPM -AP	OF&NO - KeP
Set 8	OF&NO - KaP						Surgery

Table E-4: Behavioral Testing and TBI Surgery Gantt Chart contd.

	Mon	Tue	Wed	Thu	Fri	Sat	Sun
Mouse	5/9/16	5/10/16	5/11/16	5/12/16	5/13/16	5/14/16	5/15/16
Set 1							
Set 2							
Set 3							
Set 4							
Set 5							
Set 6							
Set 7							
Set 8							EPM-TG

	Mon	Tue	Wed	Thu	Fri	Sat	Sun
Mouse	5/16/16	5/17/16	5/18/16	5/19/16	5/20/16	5/21/16	5/22/16
Set 1							
Set 2							
Set 3							
Set 4							
Set 5							
Set 6							
Set 7							
Set 8	OF&NO - TG						

	Mon	Tue	Wed	Thu	Fri	Sat	Sun
Mouse	5/23/16	5/24/16	5/25/16	5/26/16	5/27/16	5/28/16	5/29/16
Set 1							
Set 2							
Set 3							
Set 4							
Set 5							
Set 6							
Set 7							
Set 8			EPM - KaP	OF&NO - KaP			

Table E-5: Behavioral Testing and TBI Surgery Gantt Chart contd.

	Mon	Tue	Wed	Thu	Fri	Sat	Sun
Mouse	5/30/16	5/31/16	6/1/16	6/2/16	6/3/16	6/4/16	6/5/16
Set 1							
Set 2							
Set 3							
Set 4							
Set 5							
Set 6							
Set 7							
Set 8						EPM - KaP	OF&NO - KaP

Table E-6: Additional Information for Gantt Chart.

Abbreviation key	
Elevated Plus Maze	EPM
Open Field	OF
Novel Object	NO
Deceased	
Worker abbreviation key	
Kayla Ponder	KaP
Kelsey Phelan	KeP
Tess Grodner	TG
Shyanthony Synigal	SS
Mariela Aponte	MA
Caroline Bell	CB
Anita Pecurcika	AP
Aminah Smith	AS
Karly Hooper	KH

Test time	
Elevated Plus Maze	1:00 PM
Open Field	7:00 PM
Novel Object	7:00 PM

Mice in Set						
Set 1	S1M1A	S1M2B	S1M3A	S1M4B	S1M5A	S1M6B
Set 2	S2M7A	S2M8B	S2M9A	S2M10 B	S2M11 A	S2M12 B
Set 3	S3M13 A	S3M14 B	S3M15 A	S3M16 B	S3M17 A	S3M18 B
Set 4	S4M19 A	S4M20 B	S4M21 A	S4M22 B	S4M23 A	S4M24 B
Set 5	S5M25 A	S5M26 B	S5M27 A	S5M28 B	S5M29 A	S5M30 B
Set 6	S6M31 A	S6M32 B	S6M33 A	S6M34 B	S6M35 A	S6M36 B
Set 7	S7M37 A	S7M38 B	S7M39 A	S7M40 B		
Set 8	S8M41 A	S8M42 B	S8M43 A	S8M44 B	S8M45 A	S8M46 B

E.2 Representative Behavioral Testing Data

Table E-7: EPM Raw Data Week 2

ID	Total Distance(cm)	ST on Center(sec)	ST on North (sec)	ST on South (sec)	ST on West (sec)	ST on East (sec)	ST_Nowhere (sec)	Open Arm Stay Time (%)
S1M4BW2	1926.4	47.5	241	311.4	0	0	0	0
S2M7AW2	2844.1	70.5	156.9	298.9	38.7	34.9	0	1.2
S2M8BW2	2285.7	40.8	210.4	338.4	9.4	0.9	0	0.2
S2M10BW2	1529.1	27.7	133.8	423	9.2	6.2	0	0.3
S2M12BW2	1306.9	14.1	111.3	445.5	25.2	3.8	0	0.5
S3M13AW2	Mouse fell							
S3M15AW2	2075	46.7	147	390.2	15.1	0.9	0	0.3
S3M16BW2	1618.4	23.1	177	346.4	39.9	13.5	0	8.9
S4M20BW2	2625.9	67.8	161.4	324.3	34.9	11.5	0	7.7
S4M21AW2	1961.8	44	170.9	380.1	0.8	4.1	0	0.8
S4M22BW2	1998.6	49.7	254.7	275.4	12.1	8	0	0.3
S4M24BW2	2125.3	48.2	265.8	262.4	13	10.5	0	0.4
S5M25AW2	2667.6	65.4	272.3	240	18	4.2	0	3.7
S5M26BW2	Mouse fell							
S5M28BW2	2133.3	40.7	331.1	171.6	5	11.7	0	0.3
S5M29AW2	2055.3	35.8	217.4	337.4	7.5	1.8	0	1.5
S6M31AW2	1403.3	10	124.5	465.4	0	0	0	0
S6M32BW2	2456.7	60.7	327.5	98.9	86.5	26.3	0	1.9
S6M34BW2	2119.4	31.6	220.2	312.9	26.1	9.1	0	0.6
S6M35AW2	1373	58.5	306.8	156.9	60	17.7	0	1.3
S6M36BW2	1311.9	27	177	390	3.1	2.8	0	0.1
S7M38BW2	2094.2	36.1	216.3	312	26.3	9.2	0	5.9
S7M39AW2	1380.2	60.1	368.6	167.6	2.6	1	0	0.9
S7M40BW2	3105.2	99.7	233.4	212.4	18.2	36.2	0	14.1
S8M41AW2	1611.5	25.4	278.3	256.3	20.1	19.8	0	6.7
S8M45AW2	2659.5	40.9	342.9	183.7	27.3	5.1	0	5.4
S8M46BW2	2407.1	22.7	228.9	348.3	0	0	0	0

Table E-8: EPM Raw Data Week 2 contd.

ID	NE into North	NE into South	NE into West	NE into East	Total Entries	Open Arm Entries (%)	Open Arm Locations	Duration
S1M4BW2	14	16	0	0	30	0	East/West	599.9
S2M7AW2	21	22	16	6	65	33.8	East/West	599.9
S2M8BW2	17	18	5	2	42	16.7	East/West	599.9
S2M10BW2	8	12	3	6	29	31	East/West	599.9
S2M12BW2	4	9	6	1	20	35	East/West	599.9
S3M13AW2	Mouse fell							0
S3M15AW2	15	21	9	2	47	23.4	East/West	599.9
S3M16BW2	9	9	2	3	23	21.7	East/West	599.9
S4M20BW2	19	21	9	2	51	21.6	East/West	599.9
S4M21AW2	17	15	1	5	38	15.8	East/West	599.9
S4M22BW2	20	20	8	9	57	29.8	East/West	599.9
S4M24BW2	16	16	5	9	46	30.4	East/West	599.9
S5M25AW2	31	21	19	3	74	29.7	East/West	599.9
S5M26BW2	Mouse fell							0
S5M28BW2	22	17	5	7	51	23.5	East/West	560.1
S5M29AW2	15	15	8	2	40	25	East/West	599.9
S6M31AW2	6	14	0	0	20	0	East/West	599.9
S6M32BW2	21	15	13	5	54	33.3	East/West	599.9
S6M34BW2	20	13	8	1	42	21.4	East/West	599.9
S6M35AW2	11	12	21	5	49	53.1	East/West	599.9
S6M36BW2	8	10	2	7	27	33.3	East/West	599.9
S7M38BW2	19	14	9	1	43	23.3	East/West	599.9
S7M39AW2	20	4	2	2	28	14.3	East/West	599.9
S7M40BW2	29	27	6	14	76	26.3	East/West	599.9
S8M41AW2	8	13	3	7	31	32.3	East/West	599.9
S8M45AW2	22	19	5	4	50	18	East/West	599.9
S8M46BW2	18	24	0	0	42	0	East/West	599.9

Table E-9: OF Raw Data Week 2

ID	Total Distance (cm)	Total Center Time (sec)	Average Speed (cm/s)	Moving Speed (cm/s)	Move Speed (cm/s)
S1M1AW2P1		Deceased			
S1M2BW2P1		Deceased			
S1M3AW2P1		Deceased			
S1M4BW2P1	1353.1	5.1	2.3	30.3	128
S1M5AW2P1		Deceased			
S1M6BW2P1		Deceased			
S2M7AW2P1	1625.3	14	2.7	26.5	137
S2M8BW2P1	1729.1	1.9	2.9	27.6	92
S2M9AW2P1		Deceased			
S2M10BW2P1	1160.5	1.7	1.9	30.1	119
S2M11AW2P1		Deceased			
S2M12BW2P1	1156.4	3.4	1.9	29.6	82
S3M13AW2P1	1861.8	3.4	3.1	26.7	121
S3M14BW2P1		Deceased			
S3M15AW2P1	1937.1	18.7	3.2	24.2	160
S3M16BW2P1	1369.2	0.6	2.3	29.7	99
S3M17AW2P1		Deceased			
S3M18BW2P1		Deceased			
S4M19AW2P1		Deceased			
S4M20BW2P1	1398.6	0.8	2.3	30.9	86
S4M21AW2P1	1974.9	0.3	3.3	25.7	136
S4M22BW2P1	1046.9	0	1.7	37	47
S4M23AW2P1		Deceased			
S4M24BW2P1	1574.7	2.5	2.6	25.6	115
S5M25AW2P1	1424.5	0.7	2.4	30.3	80
S5M26BW2P1	2022.1	1.7	3.4	30.1	132
S5M27AW2P1		Deceased			
S5M28BW2P1	1955.2	6.2	3.3	26	118
S5M29AW2P1	1279.7	0	2.1	28.9	81
S5M30BW2P1		Deceased			
S6M31AW2P1	1305.2	1.1	2.2	34.4	93
S6M32BW2P1	891.4	1.3	1.5	35.9	74
S6M33AW2P1	893.8	1.6	1.5	35.2	91
S6M34BW2P1	675.8	4.3	1.1	46	54
S6M35AW2P1	1339.8	3.4	2.2	32.1	118
S6M36BW2P1	986.7	0.9	1.6	33.1	118

Table E-10: OF Raw Data Week 2 contd.

S7M37AW2P1	1602.8	6.9	2.7	30.4	160
S7M38BW2P1	975.4	4.5	1.6	35.2	65
S7M39AW2P1	913.9	0.3	1.5	39.7	76
S7M40BW2P1	654.6	0	1.1	51.5	50
S8M41AW2P1	1550.1	6.4	2.6	28.7	147
S8M42BW2P1	Deceased				
S8M43AW2P1	Deceased				
S8M44BW2P1	Deceased				
S8M45AW2P1	2292.6	26.7	3.8	23.9	183
S8M46BW2P1	1768	5.2	2.9	24.8	140
ID	Move Episode N	Total Movement Duration (sec)	Distance Per Movement (cm)	Duration Per Movement (sec)	
S1M1AW2P1	Deceased				
S1M2BW2P1	Deceased				
S1M3AW2P1	Deceased				
S1M4BW2P1	44.7	10.6	0.3	600	
S1M5AW2P1	Deceased				
S1M6BW2P1	Deceased				
S2M7AW2P1	61.4	11.9	0.4	600	
S2M8BW2P1	62.7	18.8	0.7	600	
S2M9AW2P1	Deceased				
S2M10BW2P1	38.6	9.8	0.3	600	
S2M11AW2P1	Deceased				
S2M12BW2P1	39.1	14.1	0.5	600	
S3M13AW2P1	69.8	15.4	0.6	600	
S3M14BW2P1	Deceased				
S3M15AW2P1	80.2	12.1	0.5	600	
S3M16BW2P1	46.1	13.8	0.5	600	
S3M17AW2P1	Deceased				
S3M18BW2P1	Deceased				
S4M19AW2P1	Deceased				
S4M20BW2P1	45.2	16.3	0.5	600	
S4M21AW2P1	76.9	14.5	0.6	600	
S4M22BW2P1	28.3	22.3	0.6	600	
S4M23AW2P1	Deceased				
S4M24BW2P1	61.4	13.7	0.5	600	
S5M25AW2P1	47	17.8	0.6	600	
S5M26BW2P1	67.2	15.3	0.5	600	

Table E-11: OF Raw Data Week 2 contd.

S5M27AW2P1	Deceased			
S5M28BW2P1	75.1	16.6	0.6	600
S5M29AW2P1	44.3	15.8	0.5	600
S5M30BW2P1	Deceased			
S6M31AW2P1	37.9	14	0.4	600
S6M32BW2P1	24.8	12	0.3	600
S6M33AW2P1	25.4	9.8	0.3	600
S6M34BW2P1	14.7	12.5	0.3	600
S6M35AW2P1	41.8	11.4	0.4	600
S6M36BW2P1	29.8	8.4	0.3	600
S7M37AW2P1	52.8	10	0.3	600
S7M38BW2P1	27.7	15	0.4	600
S7M39AW2P1	23	12	0.3	600
S7M40BW2P1	12.7	13.1	0.3	600
S8M41AW2P1	54	10.5	0.4	600
S8M42BW2P1	Deceased			
S8M43AW2P1	Deceased			
S8M44BW2P1	Deceased			
S8M45AW2P1	95.9	12.5	0.5	600
S8M46BW2P1	71.3	12.6	0.5	600

Table E-12: Assorted Data on Sectioned Tissue

ID	µm/Section	Discarded (mm)	Mounted (mm)	Total (mm)	Additional Notes
4	7	na	2.065	na	some cortex lost over injury site due to adhesion
7	10	na	1.36	na	minor damage to sample over injury site due to adhesion
8	6/10	na	1.168	na	some cortex lost over injury site due to adhesion
10	6	na	0.72	na	small amount of cortex lost
12	10	na	2.08	na	large portion of right hemisphere lost due to adhesion
13	10	0.89	1.74	2.63	small amount of tissue remained attached to skull
15	10	1.74	1.6	3.34	clean
16	10	1.08	2.07	3.15	large amount of tissue adhered to skull
20	10	1.66	1.44	3.1	clean
21	10	na	2	na	possible puncture in front of brain, difficulty removing
22	10	0.84	1.76	2.6	adherence over injury site, small chunk remained on skull
24	10	0.97	2.61	3.58	indent at injury site, possible infection
25	10	1.62	1.44	3.08	front of brain detached during excision
26	10	1.06	1.92	2.98	lost OB, otherwise clean
28	10	1.43	2.04	3.47	top of brain stuck to skull
29	10	1.51	1.46	2.97	top of brain stuck bad
30	10	1.49	1.73	3.22	clean
31	10	2.13	1.76	3.89	lost Obs, cuts from scissors
32	10	0.77	1.43	2.2	clean
34	10	1.1	2.16	3.26	clean
35	10	1.59	1.28	2.87	clean
36	10	1.38	0.72	2.1	clean
37	10	1.24	2.06	3.3	clean
38	10	1.22	1.68	2.3	clean
39	10	1.52	1.6	3.12	left hemisphere adhered, no obvious damage
40	10	na	1.28	na	od'd prematurely, not as well perfused
41	8	1.008	1.664	2.672	no major adhesion, appears intact near injury
45	10	1.3	1.52	2.82	adhered, small amount of tissue lost, minor dmg with scissors
46	10	1.78	1.12	2.9	adhesion at injury, moderate amount of tissue lost, dmg from scissors
	Chelsea cut sample to sectioning size				
	Missed 95% Etoh step during dehydration				

Table E-13: Measured Thickness of Brain Regions

ID	Corpus Callosum (µm)	External Capsule Right (µm)	External Capsule Left (µm)	Hippocampus Right (µm)	Hippocampus Left (µm)
30	311.349	120.482	88.376	99.443	62.249
31	180.723	NA	226.943	67.771	52.209
32	355.434	200.813	160.643	62.257	68.303
34	410.694	268.089	228.916	57.732	66.265
35	421.687	301.22	259.044	94.411	68.777
36	307.244	182.235	171.693	64.01	77.568
37	431.738	208.832	130.52	66.264	72.288
38	343.38	197.291	214.865	58.734	76.409
39	361.439	155.62	152.661	68.272	58.241
40	349.398	160.643	165.633	72.289	66.265
12	490.964	243.99	228.912	90.36	81.324
16	453.807	216.864	216.866	28.112	32.144
20	433.732	146.082	108.432	82.352	106.936
24	393.595	216.867	196.828	90.412	86.439
25	389.641	210.865	146.806	81.339	77.413
21	365.55	147.621	144.578	81.325	75.301
26	377.51	280.137	293.18	66.265	72.289
45	265.091	160.643	196.787	96.469	76.305
13	317.269	204.819	216.867	76.305	66.265
22	560.249	298.208	277.108	84.391	93.422
28	353.414	240.983	253.012	60.241	166.535
29	381.547	219.88	159.639	117.508	81.325
4	477.92	108.432	204.855	114.456	102.452
46	427.703	120.48	108.474	42.168	58.734
	Controls		Sham		Mild
	Moderate		Severe		

REFERENCES

[1] E. D. Olsen, *Modern Optical Methods of Analysis*. (McGraw-Hill, Inc., 1975).

[2] F. L. Pedrotti, L. S. Pedrotti, L. M. Pedrotti, *Introduction to Optics*. (Upper Saddle River, NJ, USA, ed. 3rd, 2007).

[3] S. K. Suvarna, C. Layton, J. D. Bancroft, *Bancroft's Theory and Practice of Histological Techniques*. (Elsevier, ed. 7th, 2013).

[4] J. A. Kiernan, *Histological and Histochemical Methods Theory and Practice*. (Scion Publishing Ltd, Banbury, UK, ed. 5th, 2015).

[5] T. A. Murray *et al.*, α7β2 nicotinic acetylcholine receptors assemble, function, and are activated primarily via their α7-α7 interfaces. *Molecular pharmacology* **81**, 175-188 (2012).

[6] D. W. Piston, T. J. Fellers, M. W. Davidson. (Nikon, 2019), vol. 2019.

[7] J. E. Hall, *Guyton and Hall Textbook of Medical Physiology*. (Saunders Elsevier, Philadelphi, PA, USA, ed. 12th, 2011).

[8] G. P. K. B. J. Franklin, *The Mouse Brain in Stereotaxic Coordinates*. (Academic Press, San Diego, California, ed. 2nd, 2001).

[9] F. H. Kobeissy, in *Brain Neurotrauma Molecular Neuropsychological, and Rehabilitation Aspects*, F. H. Kobeissy, Ed. (CRC Press Taylor & Francis Group, 2015), pp. xvii-xviii.

[10] W. L. Maxwell, in *Brain Neurotrauma Molecular, Neuropsychological, and Rehabilitation Aspects*, F. H. Kobeissy, Ed. (CRC Press Taylor & Francis Group, 2015), chap. 3, pp. 15-34.

[11] R. A. Laskowski, J. A. Creed, R. Raghupathi, in *Brain Neurotrauma Molecular, Neuropsychological, and Rehabilitation Aspects*, F. H. Kobeissy, Ed. (CRC Press Taylor & Francis Group, 2015), chap. 4, pp. 35-41.

[12] K. F. George Paxinos, *The Mouse Brain in Stereotaxic Coordinates*. (Academic Press (c) 2001 by Academic Press, ed. 2nd, 2001).

[13] A. Albanese, K. Chung, "Whole-brain imaging reaches new heights (and lengths)," *eLife* **5**, (2016).

[14] A. Au - Ertürk, D. Au - Lafkas, C. Au - Chalouni, "Imaging Cleared Intact Biological Systems at a Cellular Level by 3DISCO," *JoVE*, e51382 (2014).

[15] E. A. Susaki *et al.*, "Advanced CUBIC protocols for whole-brain and whole-body clearing and imaging," *Nature Protocols* **10**, 1709 (2015).

[16] K. Chung *et al.*, "Structural and molecular interrogation of intact biological systems," *Nature* **497**, 332 (2013).

[17] N. Renier *et al.*, "iDISCO: A Simple, Rapid Method to Immunolabel Large Tissue Samples for Volume Imaging," *Cell* **159**, 896-910 (2014).

[18] S. G. Parra, S. S. Vesuna, T. A. Murray, M. J. Levene, "Multiphoton microscopy of cleared mouse brain expressing YFP," *Journal of visualized experiments : JoVE*, e3848-e3848 (2012).

[19] R. James, Y. Kim, P. E. Hockberger, F. G. Szele, "Subventricular zone cell migration: lessons from quantitative two-photon microscopy," *Frontiers in neuroscience* **5**, 30 (2011).

[20] F. Doetsch, A. Alvarez-Buylla, "Network of tangential pathways for neuronal migration in adult mammalian brain," *Proceedings of the National Academy of Sciences of the United States of America* **93**, 14895-14900 (1996).

[21] F. Doetsch, J. M. García-Verdugo, A. Alvarez-Buylla, "Cellular Composition and Three-Dimensional Organization of the Subventricular Germinal Zone in the Adult Mammalian Brain," *The Journal of Neuroscience* **17**, 5046 (1997).

[22] Z. Mirzadeh, F. T. Merkle, M. Soriano-Navarro, J. M. Garcia-Verdugo, A. Alvarez-Buylla, "Neural stem cells confer unique pinwheel architecture to the ventricular surface in neurogenic regions of the adult brain," *Cell stem cell* **3**, 265-278 (2008).

[23] Z. Mirzadeh, F. Doetsch, K. Sawamoto, H. Wichterle, A. Alvarez-Buylla, "The subventricular zone en-face: wholemount staining and ependymal flow," *Journal of visualized experiments : JoVE*, 1938 (2010).

[24] C. C. Young *et al.*, "Ependymal ciliary dysfunction and reactive astrocytosis in a reorganized subventricular zone after stroke," *Cerebral cortex (New York, N.Y. : 1991)* **23**, 647-659 (2013).

[25] E. M. Shapiro, K. Sharer, S. Skrtic, A. P. Koretsky, "In vivo detection of single cells by MRI," *Magnetic Resonance in Medicine* **55**, 242-249 (2006).

[26] E. M. Shapiro, O. Gonzalez-Perez, J. Manuel García-Verdugo, A. Alvarez-Buylla, A. P. Koretsky, "Magnetic resonance imaging of the migration of neuronal precursors generated in the adult rodent brain," *NeuroImage* **32**, 1150-1157 (2006).

[27] C. L. Mallett, D. D. Shuboni-Mulligan, E. M. Shapiro, "Tracking Neural Progenitor Cell Migration in the Rodent Brain Using Magnetic Resonance Imaging," *Frontiers in neuroscience* **12**, 995-995 (2019).

[28] J. P. Sumner, E. M. Shapiro, D. Maric, R. Conroy, A. P. Koretsky, "In vivo labeling of adult neural progenitors for MRI with micron sized particles of iron oxide: quantification of labeled cell phenotype," *NeuroImage* **44**, 671-678 (2009).

[29] B. J. Nieman *et al.*, "In vivo MRI of neural cell migration dynamics in the mouse brain," *NeuroImage* **50**, 456-464 (2010).

[30] A. Holtmaat *et al.*, "Long-term, high-resolution imaging in the mouse neocortex through a chronic cranial window," *Nature protocols* **4**, 1128-1144 (2009).

[31] G. Yang, F. Pan, C. N. Parkhurst, J. Grutzendler, W.-B. Gan, "Thinned-skull cranial window technique for long-term imaging of the cortex in live mice," *Nature protocols* **5**, 201-208 (2010).

[32] A. Y. Shih, C. Mateo, P. J. Drew, P. S. Tsai, D. Kleinfeld, "A polished and reinforced thinned-skull window for long-term imaging of the mouse brain," *Journal of visualized experiments : JoVE*, 3742 (2012).

[33] G. J. Goldey *et al.*, "Removable cranial windows for long-term imaging in awake mice," *Nature Protocols* **9**, 2515-2538 (2014).

[34] C. E. J. Cheetham, "Multiphoton Intravital Calcium Imaging," *Current Protocols in Cytometry* **85**, e40 (2018).

[35] K. P. Ghiggino, M. R. Harris, P. G. Spizzirri, "Fluorescence lifetime measurements using a novel fiber-optic laser scanning confocal microscope," *Review of Scientific Instruments* **63**, 2999-3002 (1992).

[36] D. L. Dickensheets, G. S. Kino, "Micromachined scanning confocal optical microscope," *Optics Letters* **21**, 764-766 (1996).

[37] P. M. Lane, A. L. P. Dlugan, R. Richards-Kortum, C. E. MacAulay, "Fiber-optic confocal microscopy using a spatial light modulator," *Optics Letters* **25**, 1780-1782 (2000).

[38] C. P. Lin, R. H. Webb, "Fiber-coupled multiplexed confocal microscope," *Optics Letters* **25**, 954-956 (2000).

[39] J. C. Jung, M. J. Schnitzer, "Multiphoton endoscopy," *Optics Letters* **28**, 902 (2003).

[40] M. J. Levene, D. A. Dombeck, K. A. Kasischke, R. P. Molloy, W. W. Webb, "In Vivo Multiphoton Microscopy of Deep Brain Tissue," *Journal of Neurophysiology* **91**, 1908-1912 (2004).

[41] Murray, Levene, "Singlet GRIN lens for deep in vivo multiphoton microscopy," *J Biomed Opt* **17**, (2012).

[42] A. Nimmerjahn, "Two-Photon Imaging of Microglia in the Mouse Cortex In Vivo," *Cold Spring Harbor Protocols* **2012**, pdb.prot069294 (2012).

[43] D. F. Marker, M.-E. Tremblay, S.-M. Lu, A. K. Majewska, H. A. Gelbard, "A thin-skull window technique for chronic two-photon in vivo imaging of murine microglia in models of neuroinflammation," *Journal of visualized experiments : JoVE*, 2059 (2010).

[44] L. Zhang *et al.*, "Imaging glioma initiation in vivo through a polished and reinforced thin-skull cranial window," *Journal of visualized experiments : JoVE*, 4201 (2012).

[45] V. Voziyanov, B. S. Kemp, C. A. Dressel, K. Ponder, T. A. Murray, "TRIO Platform: A Novel Low Profile In vivo Imaging Support and Restraint System for Mice," *Frontiers in Neuroscience* **10**, 169 (2016).

[46] J. Alder, W. Fujioka, J. Lifshitz, D. P. Crockett, S. Thakker-Varia, "Lateral fluid percussion: model of traumatic brain injury in mice," *Journal of visualized experiments : JoVE*, (2011).

[47] C. A. Schneider, W. S. Rasband, K. W. Eliceiri, "NIH Image to ImageJ: 25 years of image analysis," *Nature methods* **9**, 671-675 (2012).

[48] P. Thévenaz, M. Unser, "User-friendly semiautomated assembly of accurate image mosaics in microscopy," *Microscopy Research and Technique* **70**, 135-146 (2007).

[49] M. C. Morganti-Kossmann, L. Satgunaseelan, N. Bye, T. Kossmann, "Modulation of immune response by head injury," *Injury* **38**, 1392-1400 (2007).

[50] B. A. Stoica, A. I. Faden, "Cell death mechanisms and modulation in traumatic brain injury," *Neurotherapeutics : the journal of the American Society for Experimental NeuroTherapeutics* **7**, 3-12 (2010).

[51] E. Siopi *et al.*, "Evaluation of late cognitive impairment and anxiety states following traumatic brain injury in mice: the effect of minocycline" *Neurosci Lett* **511**, 110-115 (2012).

[52] M. L. Schwarzbold *et al.*, "Effects of traumatic brain injury of different severities on emotional, cognitive, and oxidative stress-related parameters in mice," *Journal of neurotrauma* **27**, 1883-1893 (2010).

[53] L. B. Tucker, A. H. Fu, J. T. McCabe, "Performance of Male and Female C57BL/6J Mice on Motor and Cognitive Tasks Commonly Used in Pre-Clinical Traumatic Brain Injury Research," *Journal of neurotrauma*, (2015).

[54] R. Rodgers, A. Dalvi, "Anxiety, defence and the elevated plus-maze," *Neuroscience & Biobehavioral Reviews* **21**, 801-810 (1997).

[55] M. Komada, K. Takao, T. Miyakawa, "Elevated plus maze for mice," *Journal of visualized experiments : JoVE*, 1088 (2008).

[56] R. E. Brown, S. C. Corey, A. K. Moore, "Differences in measures of exploration and fear in MHC-congenic C57BL/6J and B6-H-2K mice," *Behavior genetics* **29**, 263-271 (1999).

[57] K. S. Holly, C. O. Orndorff, T. A. Murray, "MATSAP: An automated analysis of stretch-attend posture in rodent behavioral experiments," *Scientific Reports* **6**, 31286 (2016).

[58] A. P. O. Ferreira *et al.*, "The effect of NADPH-oxidase inhibitor apocynin on cognitive impairment induced by moderate lateral fluid percussion injury: Role of inflammatory and oxidative brain damage," *Neurochemistry International* **63**, 583-593 (2013).

[59] S. Li *et al.*, "Transient versus prolonged hyperlocomotion following lateral fluid percussion injury in mongolian gerbils" *Journal of Neuroscience Research* **83**, 292-300 (2006).

[60] S. A. Lee *et al.*, "Gradient Index Microlens Implanted in Prefrontal Cortex of Mouse Does Not Affect Behavioral Test Performance over Time," *PLOS ONE* **11**, (2016).